Università degli Studi di Milano-Bicocca

Dipartimento di Scienza dei Materiali

Corso di Dottorato di Ricerca in
Nanostrutture e Nanotecnologie
XXVI ciclo

Enhancing oxide surface reactivity by doping or nano-structuring

A.A. 2013/2014

Ph.D. dissertation

Stefano Prada

Supervisor
Dr. Livia Giordano

Contents

Chapter 1

Introduction

Simple, non defective, high gap oxides, as for example MgO, are often rather inert materials used in heterogeneous catalysis only as substrates for the active phase, usually metallic particles, thanks to their chemical stability. However, it is possible to enhance their activity in different ways: 1) by defect engineering, since low coordinated defective sites or point defects at the oxide surface are more reactive than the perfect crystal [1], 2) by doping, that has proven to be an efficient way to modify the properties of oxides [2], 3) or by nanostructuring, since oxide nanoparticles and nanofilms have peculiar properties that come from their reduced dimensions [3]. The aim of this thesis is, by using first principles calculations within the density functional theory (DFT), to study the last two aspects, doping and nanostructuring of oxides, with particular attention to engineer the charge transfer with adsorbates for catalytic purposes.

With respect to nanostructuring, this thesis addresses in particular the properties of oxide films of nanometric thickness. Indeed, ultra-thin insulating films grown on metal substrates are a new class of materials of recent use in many technological applications, such as, for example: magnetic junctions, plasma displays, dielectrics in miniaturized electronic devices and substrates for catalysis. [4–6] These thin films, of thickness usually lower than 10 Å, have a series of characteristics that do not have a counterpart in the corresponding crystal surfaces. Increasing the thickness, however, these features tend to quickly converge to those of the crystal surface; this is true even in thin films traditionally used (50-100 Å) where these peculiar characteristics are largely lost.

In particular, two unique properties make thin-film systems so fascinating for surface and material science research. On the one hand, thin films might be considered as the "electrically conductive" counterpart of wide-gap and hence insulating bulk oxides. They can thus be investigated with classical surface science techniques, as charge transport through the film remains possible via electron tunneling. On the other hand, ultrathin oxide films on metal supports turned out to be an interesting material combination in their own right, as they possess properties that are intrinsically connected with interfacial interactions between the two systems. Because of these properties, an intensive study has been performed in recent years to determine the physical and chemical characteristics and the role they play in the occurrence of the special features that distinguish them from traditional materials.

The metal substrate induces structural modifications of the supported thin film, such as, for example, the distortions of the crystal cell of the insulator caused by the difference of the lattice parameter between the two systems and atomic relaxations which are dominant at the interface. The substrate also induces changes to the electronic structure of the insulating film caused by the formation of interfacial bonds, by charge transfer phenomena and, more generally, by chemical and electrostatic interactions that are established between the respective electronic distributions. This combination of structural and electronic features, dependent on the nature of the interface, is a key factor because it allows, in principle, to modulate the properties of the system to be adapted to specific technological demands. Below, some peculiar properties of supported thin films are reviewed, focusing in particular on the role played in catalysis.

A second aspect addressed in this thesis is the possibility to tailor the properties of the oxide through doping, a versatile method that increases the opportunities to engineer new materials with enhanced performances.

1.1 Ultrathin oxide films and catalysis

The idea that metal supported thin films can play an active role in heterogeneous catalysis was introduced for the first time by Vol'kenshtein in 1966 [7] who suggested that controlling the thickness of a semiconducting oxide film (now we know this is also true for insulating film) supported on a metal it is possible to control to some extent its catalytic activity and selectivity. However, thanks to the progress of experimental tools that allow a characterization of ultrathin films at the atomic level, only in the last 20-30 years very thin supported oxide films are attracting more and more attention, also because of the potentialities and unprecedented properties this important class of materials have shown so far [8, 9]. One example of characteristic catalytic activity of ultrathin films, which is not observed in the respective monocrystalline surfaces, is the peculiar activity of thin films of MgO in water dissociation [10].

As it will be better explained later, the ability of nanosized films to respond with structural relaxations to changes in the electronic structure or composition is of great catalytic interest; a clear example is FeO / Pt(111) that, under appropriate conditions of partial pressures of oxygen, is able to modify its stoichiometry (forming a FeO_2 phase with a structural modification to the interface) becoming particularly reactive in the oxidation of carbon monoxide to CO_2 according to a classical Mars-Van Krevelen mechanism [11]. Notable is the fact that the supported oxide is more reactive than the bare metal. In this respect it is interesting to note that often in oxidation reactions the most active phase is a native nano-thick oxide that forms spontaneously at the catalyst surface under reactive condition, this is the case of ruthenium that forms a very thin ruthenium oxide film of not yet well determined structure [12]. This is in contrast with the general thought that the encapsulating oxide deactivates the catalyst (this of course depends on the system, since in many cases the formation of an oxide actually deactivates the catalyst [13]), but the reason lies in the fact that the chemical and structural properties of ultra-thin films differ significantly from their bulk counterparts. In fact, as it will be seen in many examples, oxide systems that are inert as a bulk become chemically active at the nanoscale.

The interest in the catalytic field for supported oxide thin films is not limited to the direct role of catalysts, it is very interesting to consider also their role in supporting chemically active metal particles. It is well known that the catalytic properties of metal particles deposited on oxide surfaces depend dramatically on the charging mechanisms at the interface [1]. In particular it has been shown that the charge of the adsorbed metal for such systems is closely related to the presence of surface defects. For example, cluster of Au_8 stabilized in F centers (oxygen vacancies with two trapped electrons) on the surface of MgO are particularly active in the conversion of CO to CO_2 [16], while atoms of Pd, which are inert in the gas phase, catalyse the reaction of conversion from acetylene to benzene when they are trapped in F centers on the MgO surface [17]. In this respect supporting thin oxide films on metals can act in two ways: on the one hand they can influence the properties of the defects in a sort of "defect engineering", for example stabilizing the F center in a particular charge state (F^0, F^+ and F^{2+}, where two, one and no electrons are trapped) simply changing the nature of the metal-oxide interface by the mechanism explained in the next section; this is the case of MgO/Ag(100) where F^+ are stable and MgO/Mo(100) where only F^0 are present [18]. On the other hand, supported thin oxide films can influence directly the adsorbed metal catalyst in two ways, by direct charge flow from or toward the metal substrate or acting as a template for the cluster growth. The two aspects are the subject of the next section.

1.2 Changes in electronic and structural properties of adsorbates

One of the main goal in heterogeneous catalysis is the ability to control the shape and the electronic structure of metal catalysts deposited on oxide substrates. In this respect the use of oxide thin films deposited on metals opens interesting routes to finely tailor the properties of catalysts. This is mainly due to the fact that at the nanoscale new phenomena appear when the quantum-mechanics comes into play. One example that shows very well this fact is the MgO/Mo(100) system. It was first proven theoretically that when gold atoms are deposited over very thin films (1-3L) of MgO supported by Mo, they get electrons from the metal substrate becoming negatively charged [19]. The electrons flow from the metal to the adsorbate toward the oxide film by tunneling, effect that disappears when the thickness of the film is above the mean-free paths of electrons and thus possible only at the nanoscale. The mechanism involved in the spontaneous charge transfer is very similar to the one described by Cabrera and Mott for the oxidation of metals [20]. In this case, more general because it is extended to all the semiconducting or insulating thin films and not only limited to oxide, the presence of an adsorbate whose levels fall below the Fermi energy of the metal is the driving force that stimulates the spontaneous charge transfer toward the dielectric layer. The charging mechanism is strongly dependent on the adsorbate nature, in fact, it has been shown that considering the Pd adsorption, an element less electronegative than Au, for MgO(100) and MgO/Mo(100) systems no major differences are detected and no charge transfer takes place even when the thin film is supported [19]. After the theoretical prediction the effect was confirmed experimentally for the system MgO/Ag(100) [21]; the choice of Ag was due to the fact that, thanks to the lower lattice mismatch between magnesium oxide and silver, it is easier to obtain very thin insulating films over the metal of very good quality and controlled properties. When Au atoms are deposited over 3ML of silver supported MgO, they appear spatially ordered how shown in Figure 1.1. The reason is due to the charge transfer that negatively charges the adsorbed atoms by the mechanism explained above; this fact generates electronic repulsions that drive the ordering at the surface. This is a clear example of how it is possible to obtain in principle the control of both geometrical and electronic properties of adsorbed metal catalysts. In accordance to the theoretically predicted results no charge transfer takes places when the less electronegative Pd atoms are adsorbed over the supported oxide, in this case, in fact, no spatial ordering is visible at the surface. Another very interesting aspect is shown in Figure 1.1, where the deposition of Au atoms directly over the metal substrate is also analysed; in the latter system no particles ordering is visible in contrast to the thin film case, this clearly shows that the role of the insulating thin film is crucial and not only restricted to mediate the interaction between the adsorbed catalyst and the

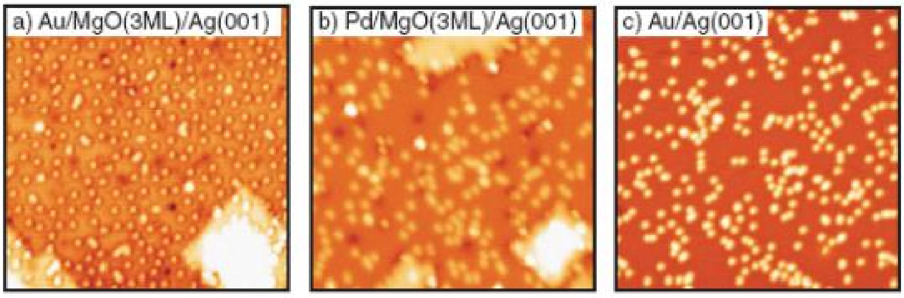

Figure 1.1: STM images (30x30nm) of a) spatially ordered and negatively charged gold atoms deposited on MgO(3L)/Ag(100); b) neutral Pd randomly distributed on the same surface; c) Au atoms directly deposited on the metal, the spatial ordering is missing. Image taken from ref. [21].

substrate.

Not only the ordering of the particles is affected by charging, but also the shape and the interaction with the substrate. It has been shown by means of DFT calculations that Au_{20} clusters have different shapes when deposited over a very-thin MgO film supported by Mo(100) or a bulk truncated MgO surface [22]; over the thick MgO surface Au_{20} assumes a tetrahedral shape as in the gas phase, on the contrary Au_{20} over the supported thin film adopts a flat configuration that wets the substrate. The change in shape is driven by the charge transfer from the metal to the cluster where the extra electron localizes at the interface between the gold and the oxide reinforcing the binding energy. This has been confirmed experimentally for the MgO/Ag(100) system [23] whose STM images are shown in Figure 1.2.

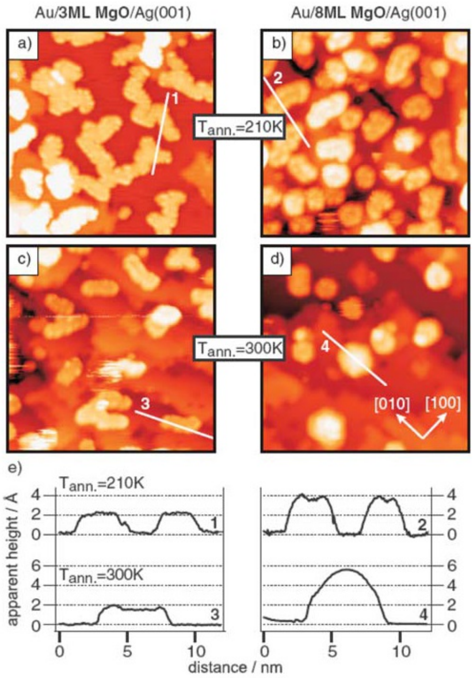

Figure 1.2: STM images of Au clusters formed after annealing Au atoms deposited on 3 ML and 8 ML thin MgO films, respectively to T = 210 K (a, b) and T=300 K (c, d). (e) Height profiles of the Au clusters marked with a solid line. Images taken from ref. [23].

The study of the Au cluster height reveals that when the thickness of the MgO film is 3ML the gold particles adopt a 2D configuration over the oxide surface; the situation completely changes when the thickness of the dielectric increases to 8ML (Figure 1.2 b-d), where the adsorption properties of gold clusters resemble essentially the ones found for adsorption on truncated bulk MgO(001), i.e. three dimensional. The difference in the shape is essentially attributed to the charge transfer at the interface as mentioned before. It is also interesting to note that not only the shape of the gold is influenced by the film thickness but also the adsorption site of the gold adatoms: strongly preferred O-top for thicker films, slightly preferred Mg-top or hollow sites for thinner film. The different behavior of the 3L and 8L MgO is not entirely due to the fact that for the thicker film the tunneling of the electrons is less efficient but it displays another interesting properties of materials at low dimensions: flexibility. Massive oxide materials are usually stiffer compared to metals and a larger energy is requested to deform the crystal lattice; the situation completely changes for very thin films that are able to easily perform a structural deformation; this has a double implication: firstly thin oxide films can easily accommodate the strain at the interface with the metal due to the different lattice parameter (this point will be expressed later in more detail) and secondly, very thin oxide films can stabilize the accumulated charge transferred to the adsorbate at the surface by means of polaronic distortion [19], an effect that is not present for thicker films. Since the structural feasibility is strongly linked to the phonon spectrum of the oxide, that is rapidly converging to the bulk one when increasing the thickness [24], this also contributes to explain why the behavior of the 3L and 8L MgO systems is different. Another contribution that stabilizes the charged adsorbate in thinner films comes from the interaction between the charged species and the image charge of the metal, an effect that decreases with the film thickness [25].

The cluster shape and its charge have important influences in the reactivity of the system, as proven for mass selected Au_{20} cluster over MgO/Mo(100) in the oxidative reaction of carbon monoxide [26]. It has been proposed that the oxide thin film has an important role, strictly related to its thickness, in the reaction, while other studies point out to a decisive charge transfer contribution from electrons trapped in defective sites [27].

In addition to MgO, many other examples are found in literature that confirm this charging phenomenon for very thin films; one is the case of charged gold particles over Al_2O_3/NiAl [28]. Naturally this effect is not restricted to gold atoms only, but in principle any species sufficiently electronegative is able to take electrons from the metal substrate by tunneling, for example the same behavior is expected for molecules like NO_2 with strong electron-acceptor character [29]; the formation of superoxo O_2^- anions upon O_2 dosing over MgO/Mo(100) are another example that has been proven both theoretically and by EPR experiments [30, 31]. In all cases described before, the direction of the charge transfer is from the metal substrate, but, thanks to the versatility of thin supported oxide films, also charge transfers in the opposite direction are possible. This is the case of the FeO monolayer supported on Pt(111), where density of state calculations and STS images show that Au atoms deposited at low temperature bind over surface oxygen and loose one electron to the substrate becoming Au^+ [32], exactly the opposite behavior of MgO over Ag or Mo. In other cases there is no charge transfer and the adsorbed species remain neutral and poorly bound to the surface as it occurs for Au on $SiO_{2.5}$/Mo(112) [33].

The reason of why different systems behave in different ways is essentially due to the energy position of electronic levels of the materials involved. In particular the driving force that causes the charge transfer is the relative position of the HOMO and LUMO levels of the adsorbate and the Fermi level of the substrate. When the LUMO level of the adsorbate lies below the Fermi level of the metal the charge is transferred from the latter to the surface, on the contrary when the HOMO level is above the Fermi level the electrons are transferred from the adsorbed species to the substrate. There is also the possibility that HOMO and LUMO are sufficiently close to the Fermi level in a way that the driving force is not sufficient to lead the spontaneous tunneling through the oxide, as in the case of Au over $SiO_{2.5}$/Mo(112). This consideration makes clear that in order to design a system of desired properties the choice of the adsorbate (electronegative atoms get charge easily) and of the oxide-metal system are crucial. The work function of the metal substrate, and thus the position of the Fermi level, is strongly related to the nature of the metal-oxide interface; this fact is of capital importance because it allows to greatly enhance the tunability of these systems simply choosing the appropriate materials; the next section is dedicated to this aspect.

The examples shown until now are focused on the fact that it is possible to tune the charge and the shape of the adsorbate by means of charge tunneling, made possible by the presence of the very thin oxide film; in addition to this, supported thin films also have the potentiality to control the spatial ordering of the adsorbed metal catalysts acting as a template for clusters growth. The interaction of the oxide with the metal can generate anchoring sites at the surface that can act as nucleation centers for the self-organized cluster growth. For example alumina thin films grown over $Ni_3Al(111)$ show a structure with small holes at the surface where atoms having a weak affinity to the oxide can nucleate [34]. Another example is FeO over Pt(111); due to the different lattice parameter of the two materials, iron oxide forms a Moirè pattern when grows over the platinum [35]. The Moirè pattern joint with the special double-layer structure of the FeO, which originates a surface dipole [36], gives rise to a system where the work function varies locally at the surface by several tenth of eV; easily polarisable Au atoms subjected to the surface potential direct towards regions with higher work function leading to a self-organized ordered arrangement, with the adatoms found at well defined distances [37, 38].

1.3 Work function change

In the previous section it was stated that the relative position between HOMO and LUMO levels of an adsorbed species and the Fermi levels of the metal substrate is the key parameter that determines the direction of the charge transfer. While the electron affinity of the adsorbate is only dependent on the species itself, the position of the Fermi level in the metal is strongly related to the nature of the interface between the oxide material and the metal substrate. In this section firstly the fundamentals of the theory of the metal work function are presented, and later it is explained how very thin dielectric films can influence this important parameter.

1.3.1 Metal work function

The work function Φ is one of the most important electronic properties of the metal surfaces. It represents the minimum energy required to extract one electron from the metal, or more specifically, it is the energy difference between a state in which the metal is at the equilibrium and a state in which one electron has been removed to a point, sufficiently far from the surface, such that the electron is no more affected by the potential exerted on it by the metal. In general, the work functions of the surfaces of a monocrystalline sample differ by about a few tenths of eV. For example, by means of photoelectron spectroscopy it has been measured that the faces (100), (110) and (111) of a single crystal of aluminum provide Φ values respectively of 4.20 eV, 4.06 eV, 4.26 eV [39]. The work function can be simply described by the following equation:

$$\Phi = -\mu + D \tag{1.1}$$

where μ is the bulk chemical potential and D represents the energy required to overcome the dipole barrier at the surface. The surface dipole barrier, which is responsible for the anisotropy of the metal work function, is generated by the redistribution of the charge density at the surface. Mainly two phenomena [40] are responsible for the redistribution of the surface charge: the first, whose effect is to increase the height of the barrier, consists in a spill-out of charge outside the surface edge. The second, whose effect, opposite to the first, is to decrease the height of the barrier, consists in a smoothing of the charge due to the broken crystal symmetry. Because these two effects have comparable intensity, it is difficult to predict the surface dipole barrier a priori without the aid of computational calculations. In the following these two phenomena will be analysed in more detail.

Charge spill-out

The explanation of this phenomenon in metals takes advantage of the simple but useful approximation of the Jellium model applied to the density functional theory [41,42], which considers a uniform distribution of positive charge instead of the discrete values of the ion cores. The electronic distribution in proximity of the surface area according to Lang and Kohn is shown in Figure 1.3 for two different values of charge density in the bulk. The figure clearly shows the spill-out of the electrons outside the edge of the positive charge distribution (assumed uniform) of the ions.

Since the tail of the charge density decays exponentially outside the surface, the self-consistent potential felt by an electron moving away from the metal decays exponentially converging to the vacuum level within approximately half the Fermi wavelength λ_F, according to the Jellium model. In

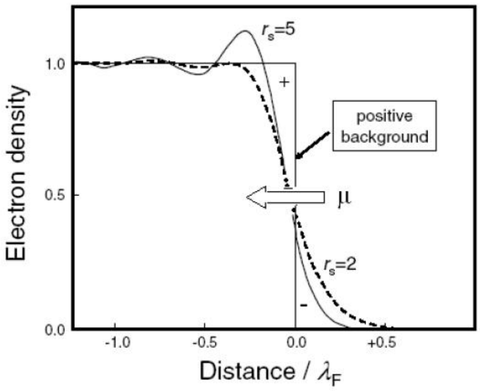

Figure 1.3: Charge spill-out for a metal surface in the Jellium model for different electron densities. The tail of electrons out of the metal surface generates a dipole μ directed inward which raises the work function. The densities r_s are expressed as the radii of the spheres of the volume of one electron. λ_F is defined as $\lambda_F = 2\pi/K_F$. Image adapted from [43].

fact, the potential decays much more slowly for the presence of the classical image charge, that generates an image potential not taken into account in this model [43]. The effect of this spill-out charge is to bring an excess of electrons out of the surface leaving the positive charge within the metal not fully screened. This leads to the formation of a surface dipole pointing inwards, whose effect is to generate a barrier that raises the energy required to extract an electron.

Smoothing of surface charge

In metals the positive ion cores are shielded by symmetric charge distributions formed by the conduction electrons within the Wigner-Seitz cell. The residual electrostatic force is weakly attractive stabilizing the high-packed structure of the solid bulk when hard core Pauli repulsion is included [44]. At the surface, the electrons are free to change their distribution in space in order to minimize the total energy. This results in a levelling of the surface charge distribution as can be seen in Figure 1.4.

The charge levelling has the effect, exactly opposite to that described in

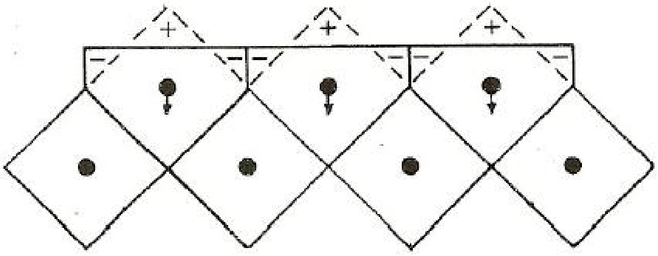

Figure 1.4: Surface relaxation generated by the levelling of the surface charge. Image taken from [44].

the previous paragraph, to generate a dipole pointing towards the exterior of the bulk, lowering in this way the energy required to overcome the surface barrier and therefore the work function [40]. The charge redistribution has another important consequence that affects the superficial structure of the metal. In this relaxed asymmetric charge distribution, in fact, the surface ions are outside the electrostatic equilibrium, a force therefore appears, directed usually towards the interior of the solid, which tends to contract the external atomic layers; this mechanism is called relaxation. The latter is not the only phenomenon that affects the surface structure of metals, in fact many of them perform more complex reconstructions to compensate the loss of coordination associated with the surface; this is the case for example of the (100) surface of gold that performs an hexagonal distortion [45]. Any change in the structure of the surface also affects the work function that then is not easily predictable from simple considerations.

1.3.2 Work function change by ultrathin films

As already mentioned several times above, the value of the metal work function is a very important parameter to determine the charging mechanism of adsorbed species on a metal/oxide system. Growing thin films of oxide materials over a metal substrate changes the work function value; this variation, which is due to the modification of the surface dipole, may occur in both directions, increasing or decreasing Φ. This versatility is of great interest in the design of metal oxide systems of suitable properties. FER (Field

Emission Resonance) experiments performed on ultra-thin films of NaCl (1-3 layers) deposited on the (100) face of Ag show a lowering of Φ of about 1.3 eV compared to the value of the free metal surface [46]. Other examples of experimental lowering of the work function by insulating films are found, for example, for a single layer of Al_2O_3 supported by Mo (100) for which $\Delta\Phi$ = -0.7 eV [47], and for alkali metal chlorides deposited on Au (111) that give rise to a reduction of the work function of 0.5-0.8 eV [48]. Exactly the opposite effect is observed in systems such as, for example, $SiO_{2.5}$/Mo (112) in which the deposition of the thin film causes a rise of the metal work function of about 0.8 eV [49].

According to the ideal Schottky model [50], when a dielectric and a metal form an interface, there is no charge transfer across the interface and the Schottky barrier height is given by the difference between the work function of the metal and the top of valence band of the dielectric. This model is generally not obeyed, the main reason lies in the fact that the interaction of the two materials generates electronic states at the interface, that are essentially of two types. The first is due to the tail of the metal wave function that decays into the dielectric in the energy range where the metal conduction band overlaps with the band gap of the insulator [51]. This gives rise to the so called metal induced gap states (MIGS) [52, 53]. The second possibility is that states at well defined energies appear when actual bonds form at the interface [54, 55]. These states can have donorlike or acceptorlike characteristics, inducing a charge transfer across the interface and thus creating a surface dipole that modifies the work function. If the charge transfer occurs from the metal to the insulator a dipole oriented in the same direction of the one generated by the spill-out of the metal charge appears. The overall effect is that these two dipoles are mutually reinforcing, resulting in an increase of Φ (Figure 1.5). If the charge transfer takes place from the dielectric to the metal the two dipoles, oriented in the opposite direction, partially cancel themselves lowering the work function.

It has been shown theoretically that the origin of the Φ increasing in the $SiO_{2.5}$/Mo (112) system is due to the charge transfer from the metal to the silica film induced by the O-Mo bonds [55]. However, although models that correlate the electronegativity difference between the atoms of the substrate and the atoms of the film to the change of the work function have been proposed [56], this can not be explained simply by phenomena of charge transfer. It has been shown that in series of interfaces between an ionic insu-

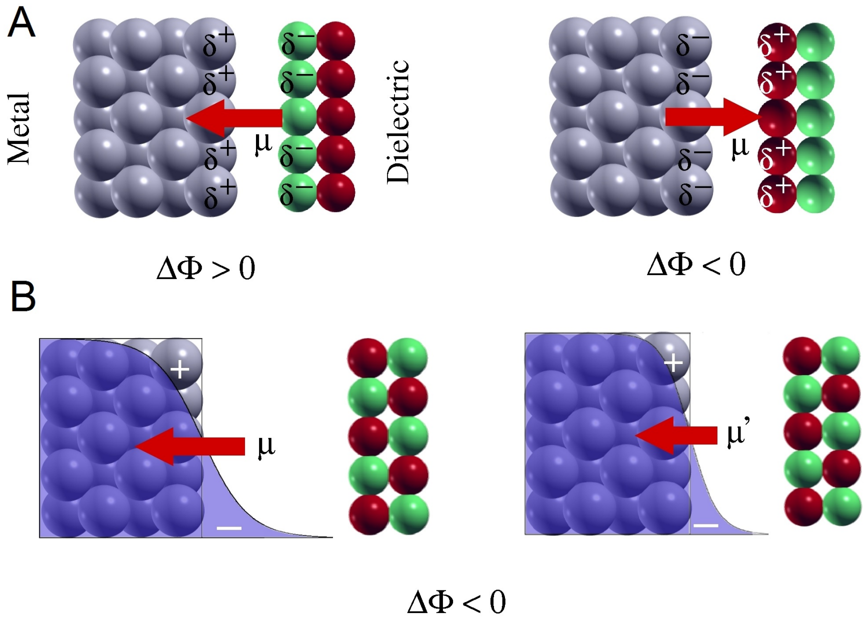

Figure 1.5: Schematic representation of the two major contributions to the change in work function Φ induced by the deposition of an ultrathin dielectric layer on a metal support. A) Charge transfer at the interface and B) compressive electrostatic effect. Both terms lead to a change in surface dipole μ, and hence in metal work function.

lator, such as MgO, and different simple and transition metals, a substantial lowering of Φ occurs in spite of the low value of charge transferred (CT). Although such transfer varies monotonically with the electronegativity of the metal, the change of the surface dipole is not proportional to CT [57]. A second effect that contributes to the Φ change comes into play. As shown in Figure 1.5, when the dielectric approaches the metal substrate there is an electrostatic compression that pushes the tail of the spilled-out charge back into the metal. This compression results in a reduction of the surface dipole and thus in a reduction of the metal work function. It is interesting to point out that while the charge transfer contribute allows Φ changes in both directions depending on the donor-like or acceptor-like character of the materials involved, the electrostatic compressive effect always results in a Φ

reduction.

The resulting work function modification is therefore a result of these two combined effects that, depending on the interface, can be respectively more or less important [55, 58]. The latter described electrostatic effect is well visible for N atoms adsorbed over W(100). In this system indeed, despite the electrons transferred to the adsorbates, the work function is reduced with respect to the free metal surface [59]. The metal tail charge compression is strongly dependent on the interfacial distance; this is clearly visible for an ionic dielectric like MgO over Ag(100) and Mo(100) systems where the electrostatic effect is dominant over the charge transfer (Figure 1.6) [55]. It is also possible that the two above mentioned effects have the same weight while they point in opposite direction, in this case they almost cancel themselves and the resulting work function is not very different from the one of the clean metal surface; this is the case of NiO growth over Ag(100) [60]. In conclusion the work function of the metal/oxide system is strongly dependent on the choice of the materials because modifications of Φ are directly related to the nature of the interface, allowing interesting possibility of fine tailoring. Once again it is evident that the role of the thin oxide film is not limited to guarantee the electronic communication between the adsorbate and the metal support.

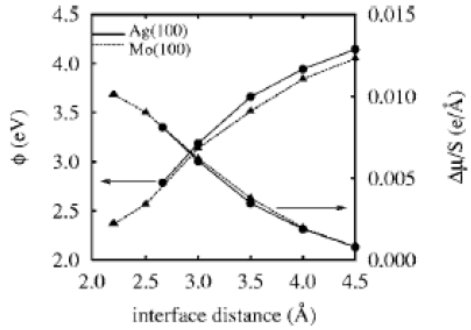

Figure 1.6: Dependence of the work function and the surface dipole from the interfacial distance in MgO(1L) / Ag (100) and MgO(1L) / Mo (100) systems. Image taken from [55].

1.4 Other properties and applications of supported thin films

In the following are briefly presented some other properties, potentialities and applications of supported thin oxide films; although the next topics are not directly related to the work done in this thesis, they clearly show how the peculiar characteristics of these systems can be used in many fields and how they potentially can play a role in new generation technologies.

1.4.1 Molecular sieves

Zeolites, microporous aluminosilicate minerals, are of great importance in heterogeneous catalysis with many industrial applications, ranging from water purification systems to petrochemical cracking and even nuclear industry, thanks to the ability to capture some ions while allowing others to pass freely. One intriguing possibility of thin films is the ability to mimic the behavior of zeolites acting as a molecular sieves. The most natural candidates in terms of chemical composition are of course supported thin silica films. $SiO_{2.5}$/Mo(112) and SiO_2/Ru(0001) are two promising materials since silica films are chemically inert and have a nanoporous surface structure [61, 62] with eventually the possibility to exchange part of silicon atoms with alluminium atoms [63]. The nanoporous structure acts as a filter that allows only atoms or molecules of well determined dimension to pass through the oxide structure reaching the interface with the metal, opening new interesting routes for the functionalization of metal supported oxide films. For example it has been shown for $SiO_{2.5}$ grown on Mo (112) that Au and Pd show a completely different mechanism of adsorption [33, 64]; Pd is small enough to penetrate through the pores of the film, binding firmly at the interface, while Au, which is too large, can not penetrate and therefore it weakly interacts only with the surface of the film (Figure 1.7).

The same effect is visible for the same system in the metal work function change induced by alkali atoms. The latter can easily donate an electron to the substrate reducing the work function value, but atoms like K, that are too big to penetrate into the pores of the film, are exposed on the surface with the possibility to loose these properties by diffusion and aggregation with other adsorbed species. Smaller atoms like Li can penetrate into the

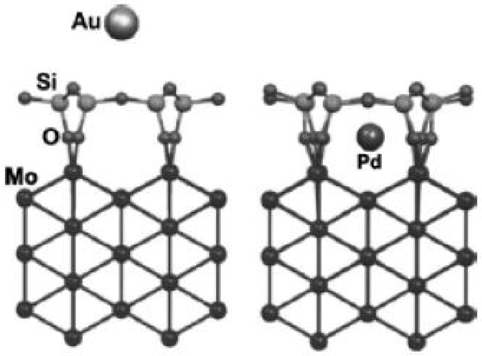

Figure 1.7: Different adsorption mechanism for Au and Pd on $SiO_{2.5}$/Mo(112). While Pd is small enough to penetrate the pores of the structure, Au remains weakly bound to the surface. Image taken from [33].

pores reaching the metal surface, and despite the Φ change is not big, it is still able to change completely the properties of the supported silica film that turns from inert to chemically active [65,66].

1.4.2 Oxide thin films as advanced materials

Oxide materials play an important role in several modern technologies. The most obvious example is the importance of the SiO_2 film grown over silicon in the development of metal oxide transistors. Since the demand for miniaturization and fine control of properties increases continuously in the nanotechnology era, research related to very-thin oxide films is becoming more and more important. Interesting applications can be found in spintronics for the magnetic tunnel junctions (MJT) [67,68] based on the giant magnetoresistive effect (GMR) [69]. The basic element of the MJT is a sandwich composed by a very thin non magnetic oxide film, like MgO, between two ferromagnetic metallic electrodes like Fe (Figure 1.8). Depending on the magnetic alignment of the two electrodes, parallel or antiparallel, the charge that flows trough the oxide by tunneling can vary up to 300% [68]. This has important applications, as in the field of magnetic sensors, or for potential new generation magnetic memories. The field of data storage is particularly important for the possible use of thin films, especially for new generation non

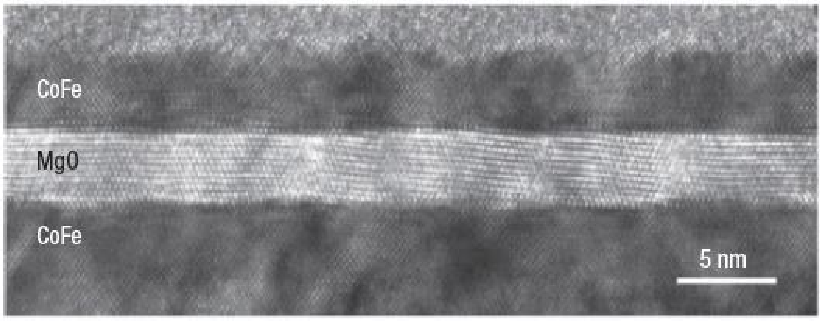

Figure 1.8: Transmission electron micrograph of CoFe/MgO/CoFe magnetic tunnel junction. Image taken from [68].

volatile memories (NVM) [70]. Nowadays the most performing NVM, memories that retain stored information even when not powered, are the Si-based flash memories. But they suffer from various problems (low durability, high writing potentials requested and so on) that make them non compatible for low energy consumption applications or even RAM-like memories. For these reasons a big effort is done in this field. Among the various research lines, the most promising involving thin oxide films [71] are: ferromagnetic RAM (FeRAM), where electric charge is stored on a ferromagnetic ultrathin oxide film capacitor [72], and resistive memories (RRAM) composed by a sandwich of an oxide between two metal electrodes [73]. The working principle of RRAM is based on the reversible formation of a conductive filament inside the oxide under an applied potential that connects the two electrodes, changing the resistivity of the system. Depending on the nature of the system, different mechanisms are involved in the filament formation, for example an Ag metal wire for Ag/TiO_2/Pt [74] or a conductive non stoichiometric oxide phase for Pt/TiO_2/Pt [75] (Figure 1.9).

Another completely different form of storage can exploit the porous structure described in the previous section. For example in the $SiO_{2.5}$/Mo(112) system it is possible to stabilize into the open rings Fe monomers that partially retain their magnetic behavior [76]. The silica cage protects them from desorption, diffusion or interaction with molecules in the external environment, making in this way a dense, thermally stable ensemble of magnetic entities.

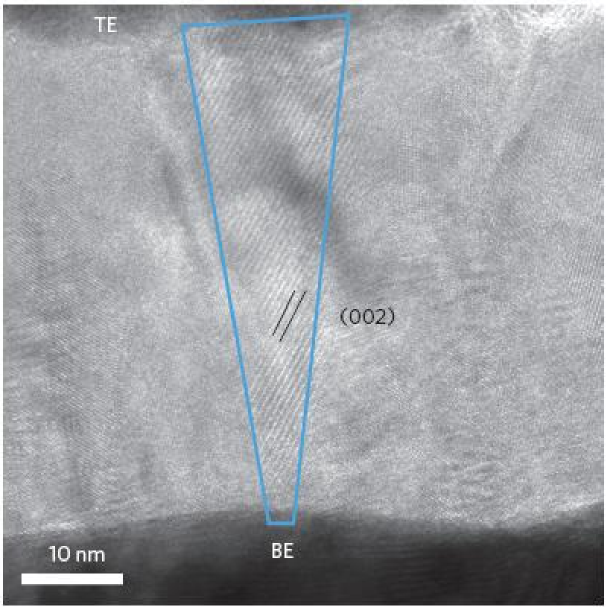

Figure 1.9: HRTEM image of a conductive Ti_nO_{2n-1} filament in the $Pt/TiO_2/Pt$ system. Image taken from [75].

Another important use of thin oxide films is the passivation of metals against corrosion [77, 78]. Since usually it is the dissolution rate that determines the lifetime of structural materials, this application has both enormous commercial and technological importance. Unstable metals become "passive" if they substantially resist corrosion under conditions where the bare metal would react significantly. This behavior is due to the inhibition of active dissolution by a more or less spontaneous formation of a dense passive film of limited ionic conductivity. Essentially there are two ways to obtain a passive film: electrochemically by anodization of the metal, or by direct deposition of a dielectric film with techniques like Physical Vapor Deposition (PVD) or sol-gel methods.

Thin oxide films play also an important role as solar energy materials, especially transparent electrically conductive oxides (TCO) due to the combination of their electronic and optical properties [79]. The most glaring example is the extensively use of indium tin oxide (ITO) as transparent anode for solar cells. TCOs are not only important for energy production, but also to address the challenge of improving energy efficiency in buildings, a very serious problem since around 40% of energy in industrialized countries is used for heating, cooling, lighting, and ventilating of buildings. For example, transparent heat mirrors, like the layered structure WO_3/Au/WO_3, are able to enhance the transmission of the visible part of spectrum suppressing simultaneously the transmission of the near-infrared part with interesting properties of energy saving in hot climate [80]. Other notable examples of applications are TiO_2-based self cleaning glasses [81] and the so called "smart windows" [82], glass that can change light transmission properties when a voltage is applied. Finally, in the energy production field, the application of solid oxide fuel cells (SOFCS) [83], that have attracted great attention because of their potential of achieving efficient energy conversion, must be mentioned.

1.5 Doping of oxide materials

A large part of this thesis is focused on the study of doped oxide materials. Oxides doping plays a crucial role in many fields of advanced technologies: microelectronics, catalysis and photocatalysis, magnetism, superconductivity, lasers and optoelectronics, ferroelectrics, sensors, etc [84–87]. Doping inorganic oxides is a central activity in materials science as it provides a versatile way to modify and tune physical, chemical, electronic, and even mechanical properties. By selective doping of oxides, one can improve the performances of devices or generate new applications. Even simple binary metal oxides like MgO may radically change their properties when doped by other elements. For instance, Cr-doped MgO has been studied as a potential laser source in the near-infrared spectral range [88]; recently, doping of MgO by many elements has been investigated as a potential source of ferromagnetism by diluted magnetic impurities [89].

One of the most important applications of doped oxides is in the electronic field; we have already cited above the importance of the transparent conducting oxides (TCO), whose most notable example is the widely used Sn-doped In_2O_3, thanks to its low resistivity and high transmittance [90]. Many other promising oxides have been studied in recent years, like ZnO and SnO_2; among them Nb-doped TiO_2 has recently attracted great interest because of excellent electrical conductivity and transparency, comparable to

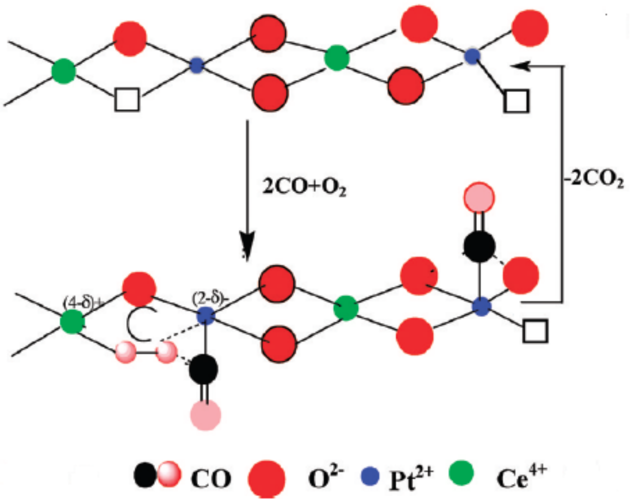

Figure 1.10: Mechanism of CO oxidation by O_2 on $Ce_{1-x}Pt_xO_{2-\delta}$: CO adsorption on Pt ion and O_2 on oxide ion vacancy; electron transfer from CO to Pt ion and to O_2(ad) via Ce ion; CO extracting dissociated oxygen from the vacant site or from the activated lattice oxygen forming CO_2. Lattice oxygen is replenished by feed oxygen. Image taken from [103].

those of ITO [91]. To design a transparent conductor the impurities must be soluble in the host and able to transfer their outer electrons to the host conduction band minimum (CBM); furthermore the host material must not introduce compensating defects (such as cation vacancies [92]) that can trap the electrons. TiO_2 is a very interesting material since it is a good solvent for numerous impurities [93] and it has a rather high formation energy for cation vacancies (under metal-rich growth conditions) [94].

Impurities can introduce extra electrons in the host structure; when the dopant locates states close to the oxide conduction band the system can behave as a TCO. However the dopants can also introduce deep gap states carrying a magnetic moment, with potential application as ferromagnetic semiconductor [94]. The principal goal in the field of ferromagnetic semiconductors for devices is the synthesis, characterization and utilization of semiconductors that exhibit substantial carrier spin polarization at and above room temperature. Such materials are of great interest in the emerging field of semiconductor spintronics [95]. One of the most promising materials is the Co-doped TiO_2, that shows an electrically induced switching from paramagnetic to ferromagnetic even at room temperature [96].

To focus on chemical properties, Li-doped [97,98] and Ni-doped [99–101] MgO, for example, have been widely studied in methane coupling catalysis and in the catalytic dissociation of N_2O, respectively. Notice that in the undoped form, MgO is a chemically rather inert material, in particular for defect-free samples. Doping oxides is of major importance in catalysis, in fact the potential ability to finely tune the properties of active species is of crucial importance to achieve the maximal reaction efficiency. For example, noble metals are widely used as catalysts to reduce pollutants from car exhaust (about the 40% of the Pt-group metals in the market is used for this purpose [102]); it has been shown recently that the catalytic activity of noble metal ions substituted in reducible oxides, like CeO_2 and TiO_2, is much higher than the corresponding metal particles supported on oxides [103].

Bibliography

[1] B. Yoon, H. Hakkinen, U. Landman, A.S. Worz, J.M. Antonietti, S. Abbet, K. Judai, U. Heiz,, *Science* **307**, 403 (2005).

[2] E.W. McFarland and H. Metiu, *Chem. Rev.* **113**, 4391 (2013).

[3] F.P. Netzer, F. Allegretti and S. Surnev, *J. Vac. Sci. Technol. B* **28**, 1 (2010).

[4] Y. Motoyama, H. Matsuzaki and H. Murakami, *IEEE Trans. Electron Devices* **48**, 1568 (2001)

[5] L.F. Weber, in: *Flat-panel Displays and CRTs*, edited by L.E Tannas (Van Nostrand Reinhold, New York, 1985), Chap. 10.

[6] Y.T. Matulevich, T.J. Vink and P.A. Zeijlmans van Emmichoven, *Phys. Rev. Lett.* **89**, 167601 (2002).

[7] F. F. Vol'kenshtein, *Russ. Chem. Rev.* **35**, 537 (1966).

[8] L. Giordano and G. Pacchioni, *Account of Chemical Research* **44**, 1244 (2011).

[9] H.-J. Freund and G. Pacchioni, *Chem. Soc. Rev.* **37**, 2224 (2008).

[10] S. Altieri, L.H. Tjeng and G.A. Sawatzky, *Phys. Rev. B* **61**, 16948 (2000).

[11] Y.N. Sun, Z.H. Qin, M. Lewandowski, E. Carrasco, M. Sterrer, S. Shaikhutdinov and H.J. Freund, *J. Catal.* **266**, 359 (2009).

[12] H. Over, Y.D. Kim, A.P. Seitsonen, S. Wendt, E. Lundgren, M. Schmid, P. Varga, A. Morgante and G. Ertl, *Surf. Sci.* **287**, 1474 (2000).

[13] P.J.M. Dukgraaf, M.J.M. Rijk, J. Meuldijk and K. van der Wiele, J. Catal. 112, 329 (1988).

[14] S. Sun, H. Li and L. Chen, *Energy Environ. Sci.* **5**, 8475 (2012).

[15] C.T. Campbell and C.H.F. Peden, *Science* **309**, 713 (2005).

[16] A. Sanchez, S. Abbet, U. Heiz, W.D. Schneider, H. Hakkinen, R.N. Barnett and U. Landman, *J. Phys. Chem. A* **103**, 9573 (1999).

[17] S. Abbet, A. Sanchez, U. Heiz, W. Schneider, A.M. Ferrari, G. Pacchioni and N.J. Rösch, *J. Am. Chem. Soc.* **122**, 3453 (2000).

[18] L. Giordano, U. Martinez, G. Pacchioni, M. Watkins and A.F. Shluger, *J. Phys. Chem. C* **112**, 3857 (2008).

[19] G. Pacchioni, L. Giordano and M. Baistrocchi, *Phys. Rev. Lett.* **94**, 226104 (2005).

[20] N. Cabrera and N.F. Mott, *Rep. Prog. Phys.* **12**, 163 (1948).

[21] M. Sterrer, T. Risse, U. Martinez, L. Giordano, M. Heyde, H.P. Rust, G. Pacchioni and H.J. Freund, *Phys. Rev. Lett.* **98**, 096107 (2007).

[22] D. Ricci, A. Bongiorno, G. Pacchioni and U. Landman, *Phys. Rev. Lett.* **97**, 036106 (2006).

[23] M. Sterrer, T. Risse, M. Heyde, H.P. Rust and H.J. Freund, *Phys. Rev. Lett.* **98**, 206103 (2007).

[24] C.J. Nelin, P.S. Bagus, M.A. Brown, M. Sterrer and H.J. Freund, *Angew. Chem. Int. Ed.* **50**, 10174 (2011).

[25] P. Frondelius, A. Hellman, K. Honkala, H. Häkkinen and H. Grönbeck, *Phys. Rev. B* **78**, 085426 (2008).

[26] C. Harding, V. Habibpour, S. Kunz, A.N.S. Farnbacher, U. Heiz, B. Yoon and U.J. Landman, *Am. Chem. Soc.* **131**, 538 (2009).

[27] Lin et al., *J. Am. Chem. Soc.* **132**, 7745 (2010).

[28] N. Nilius, M.V. Ganduglia-Pirovano, V. Brazdova, M. Kulawik, J. Sauer and H.J. Freund, *Phys. Rev. Lett.* **100**, 096802 (2008).

[29] H. Grönbeck, *J. Phys. Chem. B* **110**, 11977 (2006).

[30] A. Hellman, S. Klacar and H. Grönbeck, *J. Am. Chem. Soc.* 2009, 131, 16636 (2009).

[31] A. Gonchar, T. Risse, H.J. Freund, L. Giordano, C. Di Valentin and G. Pacchioni, *Angew. Chem. Int. Ed.* **50**, 2635 (2011).

[32] L. Giordano, G. Pacchioni, J. Goniakowski, N. Nilius, E.D.L. Rienks and H.J. Freund, *Phys. Rev. Lett.* **101**, 026102 (2008).

[33] L. Giordano, A. Del Vitto and G. Pacchioni, *J. Chem. Phys.* **124**, 034701 (2006).

[34] M. Schmid, G. Kresse, A. Buchsbaum, E. Napetschnig, S. Gritschneder, M. Reichling and P. Varga, *Phys. Rev. Lett.* **99**, 196104 (2007).

[35] M. Ritter, W. Ranke and W. Weiss, *Phys. Rev. B* **57**, 7240 (1998).

[36] Y.J. Kim, C. Westphal, R.X. Ynzunza, H.C. Galloway, M. Salmeron, M.A. Van Hove and C.S. Fadley, *Phys. Rev. B* **55**, R13448 (1997).

[37] E. D. L. Rienks, N. Nilius, H. P. Rust and H. J. Freund, *Phys. Rev. B* **71**, 2414041 (2005).

[38] N. Nilius, E.D. L. Rienks, H.P. Rust and H.J. Freund, *Phys. Rev. Lett.* **95**, 066101 (2005).

[39] R.M. Eastment and C.H.B. Mee, *J. Phys F: Metal Phys.* **3**, 1738 (1973).

[40] R. Smoluchowski, *Phys Rev. Lett.* **60**, 661 (1941).

[41] N.D. Lang ,W. Kohn, *Phys. Rev. B* **3**, 1215 (1971).

[42] N.D. Lang ,W. Kohn, *Phys. Rev. B* **1**, 4555 (1970).

[43] H. Ibach, Physics of Surfaces and Interfaces (Springer, New York, 2006).

[44] A. Zangwill, Physics at Surfaces (Cambridge University Press, Cambridge, 1988).

[45] S.G. Mochrie, D.M. Zehner and B.M. Ocko, *Phys. Rev. Lett.* **64**, 2952 (1990).

[46] H.C. Ploigt, C. Brun, M. Pivetta, F. Patthey and W.D. Schneider, *Phys. Rev. B* **76**, 195404 (2007).

[47] T.T. Magkoev and G.G. Vladimirov, *J. Phys. Condens. Matter* **13**, L655 (2001).

[48] C. Loppacher, U. Zerweck and L.M. Eng, *Nanotechnology* **15**, S9 (2004).

[49] S. Wendt, E. Ozensoy, T. Wei, M. Frerichs, Y. Cai, M.S. Chen and D.W. Goodman, *Phys. Rev. B* **72**, 115409 (2005).

[50] W. Schottky, *Phys. Z.* **41**, 570 (1940).

[51] V. Heine, *Phys. Rev.* **138**, A1689 (1965).

[52] S. G. Louie and M. L. Cohen, *Phys. Rev. B* **13**, 2461 (1976).

[53] G. Bordier and C. Noguera, *Phys. Rev. B* **44**, 6361 (1991).

[54] R.T. Tung, *Phys. Rev. B* **64**, 205310 (2001).

[55] L. Giordano, F. Cinquini, and G. Pacchioni, *Phys. Rev. B* **73**, 045414 (2006).

[56] Y.C. Yeo, T.J. King and C. Hu, *J. Appl. Phys.* **92**, 7266 (2002).

[57] J. Goniakowski and C. Noguera, *Interface Sci.* **12**, 93 (2004).

[58] S. Prada, U. Martinez and G. Pacchioni, *Physical Review B* **78**, 235423 (2008).

[59] A. Michaelides, P. Hu, M.-H. Lee, A. Alavi and D.A. King, *Phys. Rev. Lett.* **90**, 246103 (2003).

[60] F. Cinquini, L. Giordano, G. Pacchioni, A. M. Ferrari, C. Pisani, and C. Roetti, *Phys. Rev. B* **74**, 165403 (2006).

[61] J. Weissenrieder, S. Kaya, J.L. Lu, H. Gao, S. Shaikhutdinov, H.-J. Freund, M. Sierka, T.K. Todorova and J. Sauer, *Phys. Rev. Lett.* **95**, 076103 (2005).

[62] D. Loffler, J.J. Uhlrich, M. Baron, B. Yang, X. Yu, L. Lichtenstein, L. Heinke, C. Buechner, M. Heyde, S. Shaikhutdinov, H.-J. Freund, R. Wlodarczyk, M. Sierka and J. Sauer, *Phys. Rev. Lett.* **105**, 146104 (2010).

[63] D. Stacchiola, S. Kaya, J. Weissenrieder, H. Kuhlenbeck, S. Shaikhutdinov, H.-J. Freund, M. Sierka, T. K. Todorova and J. Sauer, *Angew. Chem., Int. Ed.*, **45**, 7636 (2006).

[64] M. Baron, D. Stacchiola, S. Ulrich, N. Nilius, S. Shaikhoutdinov, H.J. Freund, U. Martinez, L. Giordano and G. Pacchioni, *J. Phys. Chem. C* **112**, 3405 (2008).

[65] U. Martinez, J.-F. Jerratsch, N. Nilius, L. Giordano, G. Pacchioni and H-J. Freund, *Phys. Rev. Lett.* **103**, 056801 (2009).

[66] U. Martinez, L. Giordano and G. Pacchioni, *J. of Chem. Phys.* **128**, 164707 (2008).

[67] T. Miyazaki, T. Yaoi, and S. Ishio, *J. Magn. Magn. Mater* **98**, L7 (1991).

[68] S.S.P. Parkin, C. Kaiser, A. Panchula, P.M. Rice, B. Hughes, M. Samant and S.H. Yang, *Nat. Mater.* **3**, 862 (2004).

[69] M.N. Baibich, J.M. Broto, A. Fert, F. Nguyen Van Dau, F. Petroff, P. Etienne, G. Creuzet, A. Friederich, and J. Chazelas, *Phys. Rev. Lett.* **61**, 2472 (1988).

[70] N. Derhacobian, S. Hollmer, N. Gilbert and M. Kozicki, *Proc. of the IEEE* **98**, 283 (2010).

[71] G. Fox, et al., *Topics in Appl. Phys.* **93**, 139 (2004).

[72] C.H. Ahn, K.M. Rabe and J.M. Triscone, *Science* **303**, 488 (2004).

[73] R. Waser and M. Aono, *Nat. Materials* **6**, 833 (2007).

[74] T.Busani and R. Devine, *J. Vac. Sci. Technol.* **26**, 1817 (2008).

[75] D. Kwon, et al., *Nature Nanotech.* **5**, 148 (2010).

[76] J.-F. Jerratsch, N. Nilius, D. Topwal, U. Martinez, L. Giordano, G. Pacchioni and H.J. Freund, *ACS Nano* **4**, 863, (2010).

[77] J.W. Schultze and M.M. Lohrengel, *Electrochimica Acta* **45** 2499 (2000).

[78] C.O.A Olsson and D. Landolt, *Electrochimica Acta* **48**, 1093 (2003).

[79] C.G. Granqvist, *Sol. Energy Mater. Sol. Cells* **91**, 1529 (2007).

[80] M.F. Al-Kuhaili, A.H. Al-Aswad, S.M.A. Durrani and I.A. Bakhtiari, *Solar Energy* **86**, 3183 (2012).

[81] Y.J. Xu, J.X. Liao, Q.W. Cai and X.X. Yang, *Sol. Energy Mater. Sol. Cells* **113**, 7 (2013).

[82] G.A. Niklasson and C.G. Granqvist, *Journal of Materials Chemistry* **17**, 127, (2007).

[83] P.-C. Su, C.C. Chao, J.H. Shim, H. Joon, R. Fasching and F.B. Prinz, *Nano Lett.* **8**, 2289 (2008).

[84] A. Fujimor and H. Namatame, *Physica C* **185**, 51 (1991).

[85] C. Kilic and A. Zunger, *Appl. Phys. Lett.* **81**, 73 (2002).

[86] J. Robertson and S.J. Clark, *Phys. Rev. B* **83**, 075205 (2011).

[87] S.B. Ogale, *Adv. Mater.* **22**, 3125 (2010).

[88] S. Kuck, L. Fornasiero, E. Heumann, E. Mix, G. Huber, T. Kaȓner and A. Maaroos, *Laser Phys.* **10**, 411 (2000).

[89] P. Mavrapoulous, M. Lezaic and S. Blügel, *Phys. Rev. B* **80**, 184403 (2009).

[90] I. Hamberg and C.G. Granqvist, *J. Appl. Phys.* **60**, R123 (1986).

[91] Y. Furubayashi, T. Hitosugi, Y. Yamamoto, K. Inaba, G. Kinoda, Y. Hirose, T. Shimada and T. Hasegawa, *Appl. Phys. Lett.* **86**, 252101 (2005)

[92] J. Osorio-Guillén, S. Lany, S. Barabash, and A. Zunger, *Phys. Rev. Lett.* **96**, 107203 (2006).

[93] M. Sacerdoti et al., *J. Solid State Chem.* **177**, 1781 (2004).

[94] J. Osorio-Guillén, S. Lany and A. Zunger, *Phys. Rev. Lett.* **100**, 036601 (2008).

[95] S.A. Chambers, *Surface Science Reports* **61**, 345 (2006).

[96] Y. Yamada, K. Ueno, T. Fukumura, H. T. Yuan, H. Shimotani, Y. Iwasa, L. Gu, S. Tsukimoto, Y. Ikuhara and M. Kawasaki, *Science* **332**, 1065 (2011).

[97] T. Ito, J.X. Wang, C.H. Lin, J.H. Lunsford, *J. Am. Chem. Soc.* **107**, 5062 (1985).

[98] P. Myrach, N. Nilius, S.V. Levchenko, A. Gonchar, T. Risse, K.-P. Dinse, L.A. Boatner, W. Frandsen, R. Horn, H.-J. Freund et al., *ChemCatChem* **2**, 854 (2010).

[99] F. Kapteijn, J. Rodriguez-Mirasol, J.A Moulijn, *Appl. Catal. B* **9**, 25 (1996).

[100] R.S. Drago, K. Jurczyk, N. Kob, *Appl. Catal. B* **13**, 69 (1997).

[101] Y. Izumi, T. Shimizu, T. Kobayashi, K. Aika, *Chem. Commun.* **12**, 1053 (2000).

[102] J.M. Thomas, *J. Chem. Phys.* **128**, 182502 (2008).

[103] M. S. Hedge, G. Madras and K.C. Patil, *Acc. Chem. Res.* **42**, 704, (2009).

Chapter 2

Methods

2.1 Electronic structure calculations

To get information over all the physical variables of a system it is necessary to solve the Schrödinger equation. However, this equation is exactly solvable only for a small number of systems; for this reason it is essential, when dealing with a many-body system, to introduce some approximations. An important simplification is introduced by the adiabatic, or Born-Oppenheimer, approximation [1]. This approximation allows, due to the big mass difference existing between nuclei and electrons, to consider the motion of electrons as if the nuclei were fixed, or, in other words, we consider the motions of the two subsets decoupled. The wave function can be factorized as follows:

$$\Psi = \psi(\{\vec{r}\};\{\vec{R}\})\chi(\{\vec{R}\}) \tag{2.1}$$

where χ is the nuclear wave function that depends on the positions of the nuclei $\vec{R}$ only and ψ is the electronic wave function that depends on the coordinates of the electrons $\vec{r}$ and, in a parametric way, also on the nuclear ones. Then the Hamiltonian of the system can be rewritten as a sum of an electronic and nuclear contribution:

$$H = H_e + H_n \tag{2.2}$$

The first part of this chapter follows the DFT description reported in: "G. Grosso and G. Pastori-Parravicini, Solid State Physics, 2° ed. (Accademic Press,2003)".

For a known atomic arrangement it is therefore possible to calculate energy and electronic eigenfunctions solving the time independent Schrödinger equation:

$$H_e\psi(\{\vec{r}\};\{\vec{R}\}) = E_e\psi(\{\vec{r}\};\{\vec{R}\}) \tag{2.3}$$

$$H_e = -\frac{\hbar^2}{2m_e}\sum_i \nabla_i^2 - \sum_i\sum_n \frac{Z_n e^2}{4\pi\epsilon_0|\vec{r}_i - \vec{R}_n|} + \frac{1}{2}\sum_{i\neq j}\frac{e^2}{4\pi\epsilon_0|\vec{r}_i - \vec{r}_j|} \tag{2.4}$$

where in the last equation the first term is the kinetic energy of the electrons, the second the energy of the interaction with the nuclei and the third the electron-electron interaction energy. The presence of the third term makes an analytical resolution of the problem impossible, so that it is necessary to adopt approximations. In the ab-initio calculations a model for the wave function is chosen and the equation 2.4 is solved without the need of a priori empirical parameters. This requires, as it will be shown in the following, the use of computers and iterative methods.

2.2 Density functional theory

The fundamental idea on which the density functional theory (DFT) is based is that the energy of an electronic system, including the exchange and correlation terms, can be formulated as a function of the electron density $\rho(r)$. The energy E is defined functional of the electron density, denoted E$[\rho(r)]$, in the sense that to a given function $\rho(r)$ corresponds only a single energy. This represents a major simplification compared to the multibody equation, since here the function to be determined is the electron density that depends only on the three spatial coordinates instead of the 3×10^{23} of the multibody wave function. In 1964 the formal proof that the energy and all the electronic properties of the ground state depend solely on the electron density was given by the theorems of Hohenberg and Kohn [2].

- **Theorem 1** : "Any observable of a stationary non-degenerate ground state can be calculated exactly from its electron density"

- **Theorem 2** : "The electronic density of a stationary non-degenerate ground state can be calculated exactly determining the density that minimizes the energy of the ground state"

The electronic Hamiltonian 2.4 can be rewritten as a sum of an internal part (kinetic energy and electron-electron interaction) and an external part (electron-nucleus interaction):

$$H_e = H_{int} + V_{ext} \tag{2.5}$$

$$H_{int} = T + V_{ee} = \sum_i \frac{\hbar^2}{2m}\nabla_i^2 + \frac{1}{2}\sum_{i\neq j}\frac{e^2}{4\pi\epsilon_0|\vec{r}_i - \vec{r}_j|} \tag{2.6}$$

$$V_{ext} = \sum_i v_{ext}(\vec{r}_i) \quad \text{with} \quad v_{ext}(\vec{r}_i) \equiv V_{nucl}(\vec{r}_i) = -\sum_n \frac{Z_n e^2}{4\pi\epsilon_0|\vec{r}_i - \vec{R}_n|} \tag{2.7}$$

The theorems of Hohenberg and Kohn state, therefore, that only the knowledge of this external potential is required (determined by the arrangement of ions in a crystal lattice) to define the Hamiltonian and, in principle, to exactly calculate its eigenvalues and eigenfunctions. From the wave function of the ground state the electron density is thus obtained:

$$\rho(\vec{r}) = \langle\psi_G(\{\vec{r}\})|\sum_i \delta(\vec{r} - \vec{r}_i)|\psi_G(\{\vec{r}\})\rangle \tag{2.8}$$

Hence a functional that binds the electron density to the external potential exists:

$$\rho(\vec{r}) = F[v_{ext}] \tag{2.9}$$

the biunivocal relation also ensures that, given an electronic density, only one external potential associated to it exists. As a consequence the equation 2.9 can be inverted [3].

$$v_{ext}(\vec{r}) = G[\rho(\vec{r})] \tag{2.10}$$

An important consequence of the theorems of Hohenberg and Kohn is that they allow the formulation of a variational method for the determination of the system ground state. Given a set of N interacting electrons in a given external potential v_{ext} it is possible to formulate the functional in the following way:

$$E[\rho(\vec{r}); v_{ext}(\vec{r})] = \langle\psi_G[\rho]|T + V_{ee} + V_{ext}|\psi_G[\rho]\rangle \tag{2.11}$$

keeping fixed v_{ext} and allowing ρ to vary, the variational principle ensures that the minimum energy obtained corresponds, in principle, to the exact electronic charge distribution of the ground state. Rewriting 2.7 as:

$$V_{ext}(\vec{r}) = \sum_i \int v_{ext}(\vec{r})\delta(\vec{r} - \vec{r}_i)d\vec{r} \tag{2.12}$$

and from the 2.8 it is obtained:

$$\langle \psi_G | V_{ext} | \psi_G \rangle = \int v_{ext}(\vec{r})\rho(\vec{r})d\vec{r} \tag{2.13}$$

This allows to rewrite the functional 2.11 as:

$$E[\rho(\vec{r}); v_{ext}(\vec{r})] = T[\rho(\vec{r})] + V_{ee}[\rho(\vec{r})] + \int v_{ext}(\vec{r})\rho(\vec{r})d\vec{r} \tag{2.14}$$

The functional $F[\rho] = T[\rho] + V_{ee}[\rho]$ is universal because it does not depend on v_{ext}, but unfortunately it is not explicitly known, thus the success of the theory depends on the ability to approximate it in an appropriate way.

2.2.1 Kohn-Sham Equations

The strategy to determine the ground state of the system is therefore to minimize the functional 2.14 in respect to $\rho(\vec{r})$. Since the theorems of Hohenberg and Kohn apply to any system in spite of the fact that it is interacting or not, it is possible to greatly simplify the problem by introducing a fictitious system of single-electron wave functions to use in place of the real multi-body wave functions. By means of this fictitious non-interacting ensemble it is possible to decompose the electron density as follows:

$$\rho(\vec{r}) = \sum_i \phi_i^*(\vec{r})\phi_i(\vec{r}) \tag{2.15}$$

where ϕ are orthonormal orbitals. The key point is that by ensuring the density of the non-interacting system $\rho_0(\vec{r})$ to be identical to that of the real system (interacting) $\rho(\vec{r})$ such decomposition is widely justified, since only the overall electronic distribution enters in the functional 2.14. We do therefore not know the explicit form of the functional $F[\rho]$, but we are able to calculate kinetic energy and potential V_{ee} of a non-interacting electronic system. It is convenient to extract the treatable terms from 2.14:

$$E[\rho(\vec{r}); v_{ext}(\vec{r})] = T_0[\rho] + V_H[\rho] + \int v_{ext}(\vec{r})\rho(\vec{r})d\vec{r} + \overbrace{T[\rho] - T_0[\rho] + V_{ee}[\rho] - V_H[\rho]}^{E_{xc}[\rho]} \tag{2.16}$$

where $V_H[\rho]$ is the interelecronic Hartree interaction

$$V_H[\rho] = \frac{1}{2}\int\int \rho(\vec{r})\frac{e^2}{4\pi\epsilon_0|\vec{r}-\vec{r'}|}\rho(\vec{r'})d\vec{r}d\vec{r'} = \frac{1}{2}\sum_{i\neq j}\langle\phi_i\phi_j|\frac{e^2}{4\pi\epsilon_0\vec{r}_{ij}}|\phi_i\phi_j\rangle \tag{2.17}$$

$T_0[\rho]$ is the kinetic energy of a non-interacting system:

$$T_0[\rho] = \sum_i \langle\phi_i| - \frac{\hbar^2\nabla^2}{2m_e}|\phi_i\rangle \tag{2.18}$$

and $E_{xc}[\rho]$ is the exchange-correlation functional, where all the approximations are included. It is then possible to rewrite the functional 2.14 in the following way:

$$E[\rho(\vec{r}); v_{ext}] = \sum_i \langle\phi_i| - \frac{\hbar^2\nabla^2}{2m_e} + v_{ext}|\phi_i\rangle + \frac{1}{2}\sum_{i\neq j}\langle\phi_i\phi_j|\frac{e^2}{4\pi\epsilon_0\vec{r}_{ij}}|\phi_i\phi_j\rangle + E_{xc}[\rho] \tag{2.19}$$

introducing the exchange and correlation potential that is defined as the functional derivative of the exchange and correlation energy :

$$V_{ex}(\vec{r}) = \frac{\delta E_{xc}[\rho]}{\delta\rho(\vec{r})} \tag{2.20}$$

and developing the variational calculus of functional 2.19 we obtain the Kohn-Sham equations [4]:

$$\left[-\frac{\hbar^2\nabla^2}{2m_e} + \overbrace{v_{ext}(\vec{r}) + V_{Coul}(\vec{r}) + V_{xc}(\vec{r})}^{v_{eff}(\vec{r})}\right]\phi_i(\vec{r}) = \epsilon_i\phi_i(\vec{r}) \tag{2.21}$$

where V_{Coul} is the Hartree's mean-field Coulomb potential.

The KS equations are solved in a self-consistent way (Figure 2.1). At the beginning a guess for the charge density is needed and, using an approximated equation for the functional dependence of E_{xc} (from $\rho(\vec{r})$), V_{xc} is obtained. Then the system of KS equations is solved to obtain an initial set of KS orbitals. From this set a new charge density is calculated using the equation 2.15; the process is then reiterated untill the newer charge density

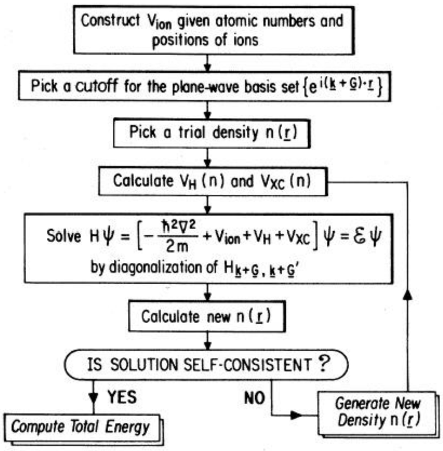

Figure 2.1: Iterative scheme for a self-consistent calculation in a plane wave code. Image taken from [5].

obtained differs below a certain tolerance with respect to the one calculated in the previous step (Figure 2.1). At each iteration the KS orbitals can be expressed numerically or with respect to a basis set of functions. In the latter case the resolution of KS equations reduces to finding the coefficients of the basis set. Once KS orbitals and energies have been determined, the total energy of the ground state of the system is given by:

$$E_0 = \sum_i \epsilon_i - \frac{1}{2}\sum_{i\neq j}\langle\phi_i\phi_j|\frac{e^2}{4\pi\epsilon_0\vec{r}_{ij}}|\phi_i\phi_j\rangle + E_{xc}[\rho] - \int V_{xc}(\vec{r})\rho(\vec{r})d\vec{r} \quad (2.22)$$

2.2.2 Local density approximation

The KS equations can not be solved unless the functional dependence of E_{xc} is provided. Since this dependence is not known it is necessary to introduce some approximations that are the main source of error in DFT. The simplest approximation used is the local density approximation (LDA) [7]. In this approximation it is assumed that E_{xc} of an electronic system in a point $\vec{r}$ is equal to that of an homogeneous gas of electrons that has the same density of the system in $\vec{r}$. The homogeneous electron gas is the only system for which one can calculate exactly the exchange and correlation energy for each electron density.

$$E_{xc} = \int \rho(\vec{r})\epsilon_{xc}[\rho(\vec{r})]d\vec{r} \tag{2.23}$$

where ϵ_{xc} is the exchange-correlation energy (known) per electron of an homogeneous electrons gas at constant density. Although this approximation is exact in the case of an ideal metal only, it describes with some accuracy also systems where the charge density is slowly varying in space.

2.2.3 Generalized Gradient Approximation (GGA)

In correspondence of the nuclei, however, the charge density varies rapidly, it is therefore necessary to introduce more sophisticated approximations that are able to describe non-homogeneous systems. One of the most used is the GGA approximation which adds to the functional a term dependent on the gradient of the electron density; this correction therefore takes into account the spatial dependence of the density.

$$E_{xc} = \int \rho(\vec{r})\epsilon_{xc}[\rho(\vec{r}), \nabla\rho(\vec{r})]d\vec{r} \tag{2.24}$$

There are different exchange-correlation functionals of this kind, the one mainly used in this thesis is the PBE functional developed by Perdew, Burke and Ernzerhof [8].

2.3 Periodic approach and VASP code

The simulation code used in this thesis is VASP (Vienna Ab-initio Simulating Package) [9]. It is a program that allows to perform ab-initio quantum mechanical simulations using plane waves as basis set. This methodology is based on the density functional theory, but the code also allows the use of post-DFT corrections such as hybrid functionals or inclusion of many body corrections. This program, along with the structural optimization and the calculation of the ground state energy, allows to obtain several additional information such as, for example, the total (DOS) and local (LDOS) density of states, charge and magnetic distributions.

2.3.1 Periodic approach

A solid material contains approximately 10^{24} atoms per cm^3; obviously such a large number of elements can not be treated by any computer. Fortunately, the high symmetry of ideal crystalline solids allows to overcome this problem. Crystalline solids, in fact, can be seen as the infinite periodic repetition of an elementary unit cell in three dimensions. The idea behind the periodic approach is therefore, rather than manage a huge number of bodies, to consider only the solutions for the atoms within the minimal crystal cell subject to periodic boundary conditions (PBC). This approach can also be used to describe defects in the structure. A defect, such as an ion vacancy, breaks the translational symmetry of the lattice. In the periodic approach defects in the cells are repeated in three dimensions for symmetry, with the result that they form a highly defective crystal with all the defects interacting with each other. To overcome this problem it is introduced the concept of supercell, that consists in a periodic cell whose dimensions are larger than the minimal one; in this way, at the cost of an higher computational effort, a structure with defects at a distance large enough to be considered non-interacting can be used. The supercell is also useful to model the surfaces of crystals, together with the slab model. In this model the cell consists of a number of atomic layers separated by a layer of vacuum. If the vacuum layer is sufficiently large, when the cell is repeated, a succession of layers is obtained (Figure 2.2) in which the atomic layers do not interact, allowing to treat the surfaces within the Bloch theorem [10].

2.3.2 Choice of the basis set

In accordance with the Bloch theorem, a wave function in a periodic potential can be written as the product of a plane wave and a modulating function $u_{\vec{k}}$ having the periodicity of the direct crystal lattice.

$$\psi_{\vec{k}} = e^{i\vec{k}\cdot\vec{r}} u_{\vec{k}}(\vec{r}) \tag{2.25}$$

$$u_{\vec{k}}(\vec{r}) = u_{\vec{k}}(\vec{r} + \vec{R}) \tag{2.26}$$

where $\vec{R}$ is a direct lattice vector and $\vec{k}$ a vector of the reciprocal space. The $u_{\vec{k}}$ periodic function can be developed in Fourier series on the basis of the

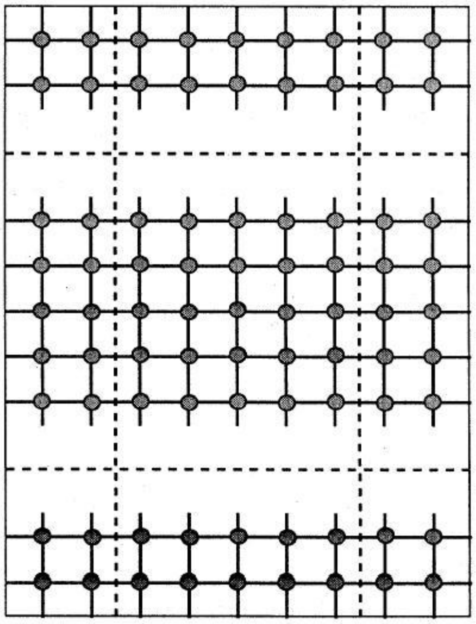

Figure 2.2: Schematic illustration of a slab model used to simulate a surface in the periodic supercell approach. Image taken from [5].

reciprocal lattice vectors $\vec{G}$:

$$u_{\vec{k}}(\vec{r}) = \sum_{G} C(\vec{k} - \vec{G}) e^{-i\vec{G}\cdot\vec{r}} \tag{2.27}$$

Since the potential is periodic in the cell, plane waves functions represent a natural basis for the Kohn-Sham orbitals in a periodic system. In principle, an infinite number of plane waves is needed to rewrite the KS orbitals, but in practice, because for the valence electrons the contribute of the high kinetic energy waves is negligible compared to those of lower energies, it is possible to truncate the series at a threshold value called cut-off. Obviously, this introduces an error in the calculation of the total energy, which can be made arbitrarily small by increasing the cut-off energy value.

2.3.3 Brillouine zone sampling

The Bloch theorem moves the problem of calculating an infinite number of wave functions (one for electron) to that of calculating a finite number of wave functions for an infinite number of $\vec{k}$ points. Because any occupied state contributes to the electronic potential, in theory an infinite number of calculations is required. Since the wave functions of contiguous $\vec{k}$ points are almost identical it is possible to approximate the functions corresponding to a region of reciprocal space with a single $\vec{k}$ point. The method used in this thesis is due to Monkhorst and Pack [11], and provides a sampling of the reciprocal space with a grid equally spaced in the Brillouin zone. Using these sampling methods it is possible to obtain a very good approximations of the properties of the system using a small number of $\vec{k}$ points, especially for insulators and semiconductors. For metals instead, a large number of $\vec{k}$ points is necessary to define with accuracy the Fermi sphere. In VASP different methods of smearing are implemented to reduce this number to an acceptable value.

2.3.4 Projector augmented-wave method

In VASP only the valence electrons are treated explicitly while the ions and the core electrons are treated in the approximation called frozen core. To define the valence states in the interatomic region only few plane waves are needed to describe the slowly oscillating character in space, but close to the nuclei the increased kinetic energy and the required orthonormality with the localized core states result in rapid oscillations (Figure 2.3). To describe these fluctuations an extremely high numbers of plane waves is necessary. The PAW method (Projector Augmented Wave), developed by Blöchl [12] and implemented in VASP by Kresse and Joubert [13], allows to reduce this number being able to effectively describe the nodal character of the function (unlike the pseudopotentials in which this character is suppressed in the core region) ensuring orthogonality between valence and core wave functions. In the PAW approach the all-electron valence functions are described as an overlap of different terms: the first part is a plane wave (pseudofunction) and the second part is an expansion on pseudoorbitals and atomic orbitals from each atom. A more complete description of the method can be found in J. Hafner (2008) [14].

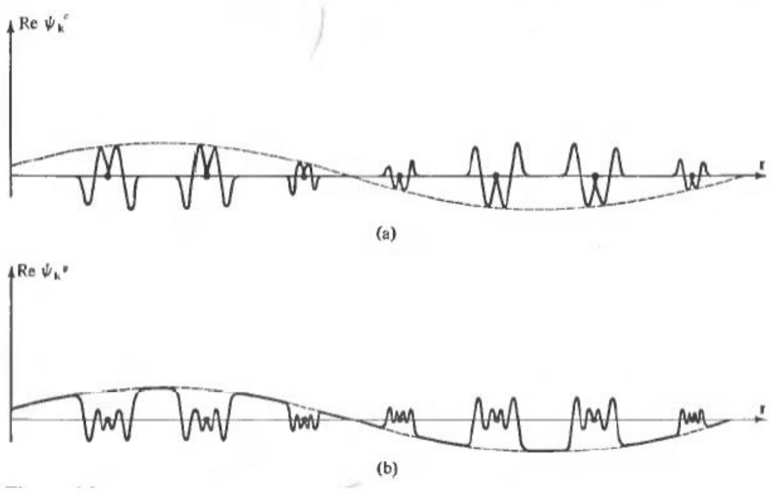

Figure 2.3: a) Core wavefunctions, b) valence wavefunction, notable are the rapid oscillations nearby the nuclei. Image taken from [6].

2.3.5 Structural optimization

As previously stated, the external potential is determined by the positions of the ions, so that the ground state energy and the wave functions depend parametrically on the ionic coordinates $\vec{R} = \{\vec{R}_I\}$. The force $\vec{F}_I$ acting on an ion positioned in $\vec{R}_I$, according to the Hellmann-Feynman theorem, is given by:

$$\begin{aligned} -\vec{F}_I &= \nabla_I E_0(\vec{R}) = \frac{\partial}{\partial \vec{R}_I} \langle \Psi_0(\vec{R}) | H(\vec{R}) | \Psi_0(\vec{R}) \rangle \\ &= \underbrace{\langle \nabla_I \Psi_0 | H | \Psi \rangle}_{=0} + \langle \Psi_O | \nabla_I H | \Psi_O \rangle + \underbrace{\langle \Psi_0 | H | \nabla_I \Psi_0 \rangle}_{=0} \\ &= \langle \Psi_0(\vec{R}) | \nabla_I H(\vec{R}) | \langle \Psi_0(\vec{R}) \rangle \qquad (2.28) \end{aligned}$$

where the first and third terms are zero for the variational properties of the ground state. Forces acting on the ions are then given by the expectation value of the gradient of the Hamiltonian in the electronic ground state. At the end of each self-consistent cycle, forces are calculated and the positions of the ions updated until the maximum force acting on a single ion is below the set threshold value. In VASP several algorithms that deal with the motion of the ions are implemented, in this thesis the CG (conjugated-gradient) algorithm has been used. For a detailed discussion of the algorithm see [15].

2.4 Beyond standard DFT

2.4.1 DFT limitations

Although DFT is able to predict with great accuracy many properties of a variety of systems, it suffers from some important limitations. The most relevant failures of DFT, in relation to the work done in this thesis, are schematically outlined below:

1. Band gap problem: the Hoenberg and Kohn theorems are not valid for the excited states. Furthermore, as previously mentioned, single particle energy values that are obtained from the Kohn-Sham equations are only Lagrange multipliers of the fictitious non-interacting system, not the eigenvalues of the real system. For these reasons band-gaps in semiconductors and insulators are always underestimated.

2. Binding: LDA gives too small lattice constants, while it overestimate cohesive energies and bulk moduli. However this problem is largely corrected by GGA functionals, that give lightly larger lattice constant for the heaviest elements.

3. Neglecting of strong correlations: exchange-splitting is underestimated for narrow d- and f-bands. As a results many transition-metal compounds that are Mott-Hubbard or charge-transfer insulators are predicted to be metallic by standard DFT.

4. Neglecting of van der Waals (vdW) interactions: vdW forces arise from mutual dynamical polarization of the interacting atoms, and it is not included in any DFT functional.

In order to overcome the above mentioned problems several methods exist that can be called post-DFT corrections. These methods are very numerous, and each one has advantages and drawbacks. The following paragraphs briefly describe post-DFT methods that have been used during the work done in this thesis.

2.4.2 DFT+U

As stated above, standard DFT underestimates the exchange-splitting for narrow d- and f-bands, this causes that strongly correlated transition metals oxides as FeO and NiO result metallic in spite of their insulating nature. To solve these problems it has been proposed by Anisimov [16] a new approach called DFT+U that adds a Hubbard type Coulombic repulsion to the Hamiltonian. The version implemented in VASP and used here is due to Dudarev [17], which uses on-site density matrices ρ^σ to define the energy functional:

$$E_{DFT+U} = E_{DFT} + \frac{U-J}{2}\sum_{\sigma} Tr[\rho^\sigma - \rho^\sigma \rho^\sigma] \tag{2.29}$$

where U is the Hubbard parameter $U = E(d^{n+1}) + E(d^{n-1}) - E(d^n)$, which measures the increase of energy caused by placing an additional electron at a given site, and J is the Stoner-like exchange term. Compared to classical DFT the occupied states are lowered by $(U-J)/2$ and those unoccupied raised by $(U-J)/2$. The DFT+U is a semiempirical approach with U-J specified by the user, in this respect the choice of U and J is to some extent arbitrary.

2.4.3 Hybrid Functionals

Hybrid functionals are characterized by mixing nonlocal Fock exchange and local or semilocal DFT exchange in a certain proportion. The choice is motivated by the attempt to solve the problems of both functionals that are to some extent complementary: band gap are too narrow for standard DFT and too wide for HF calculations. Moreover, this mixing gives the additional possibility to obtain more accurate total energies and geometries. One of the most popular hybrid functional is the semi-empirical B3LYP [18], where the mixing coefficients have been determined by fitting a test set of molecules. The PBE0 functional [19, 20] (used in this thesis) mixes 1/4 of exact (HF) exchange with 3/4 of PBE exchange, and describes the correlation at the GGA (PBE) level:

$$E_{xc}^{PBE0} = 0.25E_x^{HF} + 0.75E_x^{PBE} + E_c^{PBE} \tag{2.30}$$

Using plane waves, under periodic boundary conditions, the calculation of the HF exchange energy is very expensive because of the slow decay of the exchange interaction with distance. For this reason it has been proposed by Heyd et al. [21] to separate the Coulomb kernel into a short-range and long-range part:

$$\frac{1}{r} = S_\mu(r) + L_\mu(r) = erfc(\mu r)/r + erf(\mu r)r \tag{2.31}$$

where μ is the range-separation parameter determining the distance (equal to $\approx 2/\mu$) beyond which the short-range interaction becomes negligible. In the HSE functional, the mixing of HF and DFT exchange is applied only to the short-range interaction:

$$E_{xc}^{HSE} = 0.25E_x^{sr,HF} + 0.75E_x^{sr,PBE} + E_x^{lr,PBE} + E_c^{PBE} \tag{2.32}$$

It has been proven empirically that it is a good choice to take μ between 0.2 Å^{-1} (HSE06) and 0.3 Å^{-1} (HSE03). The use of the separated range helps to obtain a faster convergence with respect to the number of k-points. It is universally recognized that the improvements of the band gap are significant with the use of hybrid functionals: small gap semiconductors are better described by HSE functional (overestimated for PBE0), but high band gap insulators are still underestimated even using PBE0. Unfortunately hybrid functionals have some drawbacks, first of all the worse description of metals due to the broadening of the bands compared to standard DFT, the second is the description of magnetic metal systems arising from an overestimation of the exchange-splitting [22]. Moreover, the computational effort is dramatically increased when using hybrid functionals.

2.4.4 Van der Waals interactions

A general drawback of all common GGA, and also hybrids functionals, is that they can not describe the long range electron correlations responsible for the van der Waals forces. Since real materials have instantaneous electronic fluctuations that are at the basis of the vdW interactions, the latter may become important to describe some kind of systems. A pragmatic method to work around this problem has been given by the DFT-D approach [23], which consists in adding a semi-empirical dispersion potential to the conventional Kohn-Sham DFT energy:

$$E_{DFT-D} = E_{KS-DFT} + E_{disp} \tag{2.33}$$

The first approach used in this thesis is the DFT-D2 method due to Grimme [24] where the van der Waals interactions are described via a simple pair-wise force field. The dispersion energy for periodic systems is defined as:

$$E_{disp} = \frac{s_6}{2} \sum_{i=1}^{Nat} \sum_{j=1}^{Nat} \sum_{\vec{L}}{}' \frac{C_6^{ij}}{|\vec{r}^{i,0} - \vec{r}^{j,\vec{L}}|^6} f\left(|\vec{r}^{i,0} - \vec{r}^{j,\vec{L}}| \right) \tag{2.34}$$

where the summations are over all atoms N_{at} and all translations of the unit cell $\vec{L} = (l_1, l_2, l_3)$ excluding $i = j$ for $L = 0$ (interactions of pairs are limited by choosing a suitable cut-off radius). S_6 is a global scaling factor that only depends on the functional used. C_6^{ij} denotes the dispersion coefficient for the atom pair ij defined as $C_6^{ij} = \sqrt{C_6^i C_6^j}$ .The term $f(r^{ij})$ is a damping function used to avoid near singularities for small r_{ij}.

$$f(r^{ij}) = \frac{1}{e^{-d(r^{ij}/R_0^{ij} - 1)}} \tag{2.35}$$

where d is a dumping parameter and R_0^{ij} is the sum of atomic vdW radii $R_0^{ij} = R_0^i - R_0^j$. The parameters used in this equation are obtained by fitting and are tabulated for each atoms. Although this method is based on empirical parameters, it has the advantage to give quite good results with a negligible additional computational cost.

The second approach used in this thesis is the van der Waals density functional (vdW-DF) method developed by Langreth and Lundvquist groups [25]. In this functional the exchange-correlation energy takes the form of:

$$E_{xc} = E_x^{GGA} + E_c^{LDA} + E_c^{nl} \tag{2.36}$$

where the last term is the nonlocal energy that approximately accounts for the dispersion. It is notable that, with respect to the DFT-D2 method of Grimme, there is no need of empirical parameters for each species. There are several functional forms proposed implemented in VASP [26].

Bibliography

[1] M. Born and R. Oppenheimer, *Ann. Phys.* **84**, 457 (1928).

[2] P. Hohemberg and W. Kohn, *Phys. Rev. B* **136**, 864 (1964).

[3] G. Grosso and G. Pastori-Parravicini, Solid State Physics, 2° ed. (Accademic Press,2003).

[4] W. Kohn and L. Sham, *Phys. Rev. A* **140**, 1133 (1965).

[5] M. Payne, et al., *Rev. of Modern Phys.* **65**, 1045 (1992).

[6] N. Ashcroft, Solid State Physics (Thomson Learning Inc., 1976).

[7] J. Perdew and A. Zunger, *Phys. Rev. B* **23**, 5048 (1981).

[8] J. Perdew, K. Burke and M. Ernzerhof, *Phys. Rev. Lett.* **77**, 3865 (1996).

[9] http://cms.mpi.univie.ac.at/vasp/

[10] F. Bloch, *Z. Phys D* **52**, 555 (1929).

[11] H. Monkhorst and J. Pack, *Phys. Rev. B* **13**, 5188 (1976).

[12] P. Blochl, *Phys. Rev. B* **50**, 17953 (1994).

[13] G. Kresse and J. Joubert, *Phys. Rev. B* **59**, 1758 (1999).

[14] J. Hafner, *J. Comput. Chem.* **29**, 2044 (2008).

[15] W. Press, S. Teukolsky, W. Vetterling, B. Flannery, Numerical recipes in C: the art of scientific computing, 3° ed (Cambridge University Press, 2007).

[16] V. Anisimov, J. Zaanen and O. Andersen, *Phys. Rev. B* **44**, 943 (1991).

[17] S. Dudarev, G. Botton, S. Savrasov, C. Humphreys and A. Sutton, *Phys. Rev. B* **75**, 1505 (1998).

[18] A.D. Becke, *J. Chem. Phys.* **98**, 1372 (1993).

[19] C. Adamo and V. Barone, *J. Chem. Phys.* **110**, 6158 (1998).

[20] M. Ernzherhof and G.E. Scuseria, *J. Chem Phys* **110**, 5029 (1999)..

[21] J. Heyd and G.E. Scuseria, *J Chem Phys* **118**, 8207 (2004).

[22] J. Paier, M. Marsman, K. Hummer, G. Kresse, I.C. Gerber and J.G. Ángyán, *J. Chem. Phys.* **124**, 154709 (2006).

[23] X. Wu, M.C. Vargas, S. Nayak, V. Lotrich and G. Scoles, *J. Chem. Phys.* **115**, 8748 (2001).

[24] S. Grimme, *J. Comp. Chem.* **27**, 1787 (2006).

[25] M. Dion, H. Rydberg, E. Schröder, D.C. Langreth and B.I. Lundqvist, *Phys. Rev. Lett.* **92**, 246401 (2004).

[26] J. Klimes, D.R. Bowler and A. Michaelidis, *Phys. Rev. B* **83**, 195131 (2011).

Results

Chapter 3

MgO/Ag and FeO/Pt, case studies beyond standard DFT

As reported in section 2.4 standard DFT suffers from some limitations that can result in a poor description of some particular aspects of materials. Since the theory of computational science is rapidly growing, more details can be understood as newest and refined methods are developed [1]. Simulation of oxide materials can benefit from method improvements since they help to overcome the intrinsic limits of standard DFT theory, especially the poor description of insulator band gaps (see 2.4.1). Unfortunately, at present, there is a lack of knowledge about performances of improved methods in the description of combined metal/oxide systems. In this chapter we analyse two case studies at different DFT levels including van der Waals interaction and hybrid functionals, which are characterized by mixing exact Fock exchange with pure DFT (see 2.4.3).

The first part of this chapter is focused on the Ag-supported MgO thin films. We enquire essentially two aspects: the first is related to the electronic and structural properties of stoichiometric systems, with particular attention on the metal work function change induced by the thin oxide film. The

---

The results of this chapter have been reported in the following publications: S. Prada, L. Giordano, G. Pacchioni and J. Goniakowski, "Theoretical description of oxide metal interfaces: MgO ultra-thin films on Ag(100) as a case study beyond standard DFT", in preparation; S. Prada, L. Giordano, G. Pacchioni and J. Goniakowski, "Properties of Pt-supported iron oxide ultra-thin films: effect of hybrid functionals", in preparation second aspect is the F centers (oxygen vacancies) formation in the supported oxide film. STM measurements have clearly demonstrated, in agreement with theoretical prediction [2,3], that F centers introduce energy levels within the band gap of MgO [4]. When a sufficiently thin oxide film is supported on a metal, electron transfer can occur between the defect and the substrate in both directions by tunnelling. For this reason the correct alignment of the defect-induced gap states with respect to the metal Fermi level is crucial to properly describe the properties of F centers in the combined metal-oxide material.

The second part of the chapter is related to FeO, an antiferromagnetic oxide, grown over Pt. We are interested to study how hybrid functionals perform in describing supported magnetic transition metal oxides, which are not well characterized in standard DFT, where they appear as small gap semiconductors or even metals. In this context, the goal of the second part of this chapter is to determine to what extent the calculated properties of the Pt-supported iron oxides are affected by the use of the simple DFT+U approach for the description of their electronic characteristics and what type of improvements are brought by more robust, hybrid approximation to the exchange-correlation functional.

The choice of the two systems is due to the fact that their properties have been extensively characterized by both standard DFT theory and experiments. [4–8] We show that while the hybrid approximation improves substantially the electronic characteristics of the oxide films, and adatoms, its overall impact on the calculated stability and reactivity characteristics is essentially negligible.

3.1 MgO(100)/Ag(100)

3.1.1 Computational Details

Spin-polarized calculations have been performed in the framework of density functional theory (DFT), using a periodic approach and a plane-waves basis set, as implemented in the VASP code (see section 2.3). We used different functionals, from standard GGA(PBE), with and without van der Waals correction, to PBE0 and HSE hybrid functionals. The treatment of vand der Waals interactions was done at two levels of theory: with the simple semi-empirical DFT-D2 method of Grimme, and using non-local functionals [9] based on the vdW-DF proposed by Dion et al. [10](see section 2.4.4). Among the various non-local vdW correlation functionals implemented in VASP we chose the optB88-vdW, since it slightly outperforms both optPBE and original rev-PBE functionals in describing solids [9, 11].

The Ag(100) surface was represented by a slab made up of four atomic layers, with up to 4ML of MgO(100) adsorbed on one side only. A vacuum layer of at least 10 Å and dipole correction were used in order to eliminate the spurious interaction between periodic replica. Since, with all the functionals used, the Ag lattice parameter is smaller (<2%) than the MgO one, the oxide film is slightly constrained to match the metal. Ag lattice parameters were optimazed for both PBE and hybrid functionals, while VdW correction was added in the combined system using the silver lattice parameter optimized with PBE . We used a (1×1) surface cell to compute the perfect MgO/Ag surface while to study the oxygen vacancy formation we employed a (2×2) supercell to make a compromise between the computational effort and the spurious lateral interactions of defect replica. We considered only single oxygen vacancies in the outmost oxide layer. During geometry optimization all atoms in the MgO film and in the two outmost metal layers were relaxed, until forces became smaller than 0.01 eV/Å, while the remaining two metal layers were frozen at their optimized bulk position. We used a (11×11×1) Monkhorst-Pack sampling of the Brillouin zone for the (1×1) surface cell, while a (3×3×1) grid was employed to study the oxygen vacancy.

To simulate a paramagnetic F^+ center we have removed one electron from the periodic cell of the neutral F center. To keep the electrical neutrality a uniform neutralizing background was added. It is worth noting that the neutralizing background does not affect the results, as proven by replacing one divalent Mg atom with a monovalent Na atom [5].

3.1.2 MgO and Ag bulk

In Table 3.1 energy gaps and optimized lattice parameters of bulk MgO using different functionals are reported. The use of hybrids results in an improvement of the calculated lattice parameter that now matches the experimental value (4.21 Å [12]). The improvement in the description of the band gap is significant using hybrids, although it remains systematically underestimated even with the PBE0 functional (experimental value: 7.8 eV [13]).

	a (Å)	E_g (eV)
PBE	4.26	4.6
HSE06	4.21	6.4
PBE0	4.21	7.2

Table 3.1: Bulk MgO characteristics obtained using PBE, HSE06, and PBE0: lattice parameter a (Å), band gap E_g (eV) (calculated as a difference between the highest occupied and the lowest unoccupied state).

The optimized lattice parameter of silver is less affected by the functional, the results obtained are 4.16 Å for PBE and HSE06 and 4.15 Å using PBE0 (experimental value: 4.09 Å [14]). In the following, due to the reported slow convergence of PBE0 with respect to the number of k-points and the bandwidth overestimation in describing metals [15], we have considered only the hybrid HSE06 for the combined metal-oxide system.

3.1.3 Ag-supported MgO(100)

Table 3.2 summarizes the properties of the MgO(3L)/Ag(100) film computed at different levels of theory. We start the discussion comparing the hybrid HSE06 functional with standard GGA(PBE). First of all it is interesting to note that the work function (Φ) of the bare (100) Ag surface is better described by the GGA functional. In fact, the PBE value of 4.18 eV is closer to the experimental one (4.21 eV) with respect to the HSE06 one (3.98 eV), slightly underestimated. After MgO deposition Φ decreases as shown many times in literature [16–18]. Here we can see that the $\Delta\Phi$ is almost the same using the two functionals and only slightly larger for HSE06 which then gives a smaller overall $\Phi_{Ag/MgO}$ value (around 0.2 eV). The interfacial distance is 0.04 Å shorter using HSE06, but the charge transferred to the metal is higher using PBE (consistent with the higher Φ of Ag). Since both electrostatic compression and charge transfer to the metal contribute to reduce the metal work function (see 1.3), this explains why $\Delta\Phi$ is almost independent from the functional used. The shorter MgO interlayer distance for HSE06 can be explained by the smaller optimized MgO lattice parameter (Tab. 3.1). The surface rumpling and the adhesion energy are not affected by the hybrid

	d_{inter} (Å)	d_{MgO} (Å)	r_{MgO} (Å)	E_{adh}/S (meV/Å^2)	CT/S (e/Å^{2}x10^3)	Φ_{Ag} (eV)	$\Phi_{Ag/MgO}$ (eV)	$\Delta\Phi$ (eV)
PBE	2.67	2.16	0.046	23.0	5.86	4.18	2.92	-1.26
HSE06	2.63	2.12	0.047	23.0	5.03	3.98	2.69	-1.29
vdW Grimme	2.50	2.12	0.054	79.6	6.92	4.20	2.82	-1.38
vdW optB88	2.63	2.15	0.036	46.3	5.91	4.52	3.06	-1.46

Table 3.2: Properties of the MgO(3L)/Ag(100) film computed at different levels of theory: interfacial distance (d_{inter}), MgO interlayer distances (d_{MgO}, from the interface to the surface), MgO surface rumpling (r_{MgO}) defined as z_O-z_{Mg}, adhesion energy per surface area (E_{adh}/S), charge transfer per surface area (CT/S, estimated from the Ag Bader charges, positive when electrons are transferred from the oxide to the metal), Ag(100) work function (Φ_{Ag}), MgO(3L)/Ag(100) work function ($\Phi_{Ag/MgO}$), work function change ($\Delta\Phi$).

functional.

In Table 3.2 the results obtained adding the DFT-D2 van der Waals correction of Grimme at the PBE level are also reported. The most significant difference with respect to PBE is the increased adhesion energy that triples when including vdW interactions; this results in a shorter interfacial distance (by almost 0.2 Å). This value of d_{inter} (2.50 Å) is more consistent with the experimental values reported in literature (2.4/2.5 Å) [19–21]. The reduced distance at the interface reinforces the compressive effect at the interface giving rise to a higher $\Delta\Phi$. Also the increased charge transfer has a role in reinforcing $\Delta\Phi$, while the higher surface rumpling, although it drives in the opposite direction, is not sufficient to compensate the last two effects. The overall result is a stronger Φ lowering with respect to both PBE and HSE.

The last functional to compare in Table 3.2 is the non-local optB88 correlation functional. With respect to PBE the film adhesion energy doubles and the interfacial distance is shortened, but the effect is not as prominent as using the empirical correction of Grimme and it is of the same order as HSE. The work function of the bare substrate is poorly described and significantly overestimated compared to other functionals. The change in the work function due to the deposition of the film is the highest of the series, a result partially explained by the smallest rumpling of the supported oxide film.

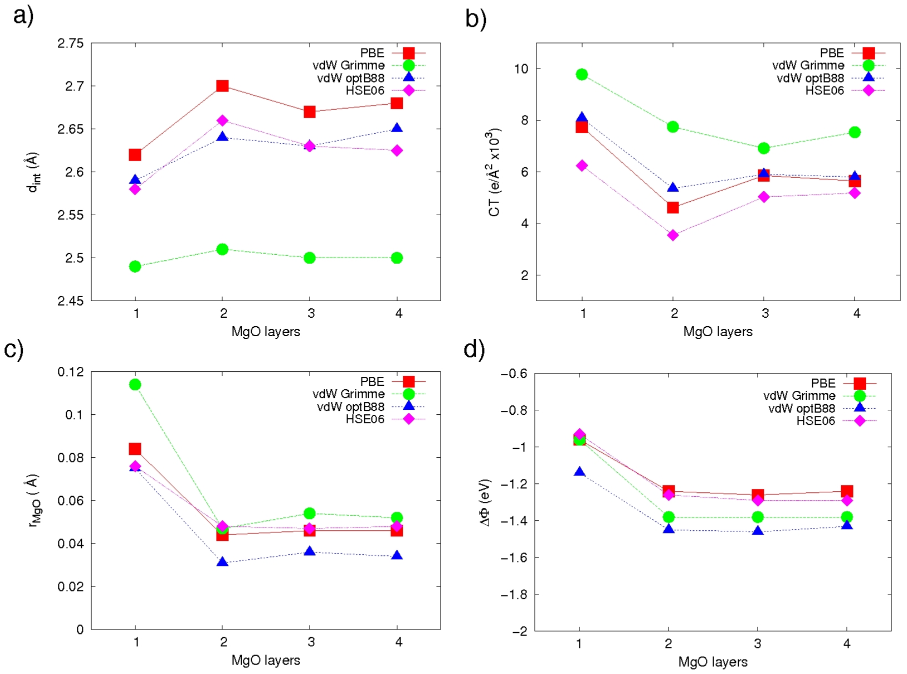

Figure 3.1: Properties of the MgO(nL)/Ag(100) interface as a function on the thickness (n=1-4), computed with the different methods: (a) interface distance; (b) charge transfer; (c) surface MgO rumpling; (d) work function change with respect to the Ag(100) surface.

To summarize the results reported in Table 3.2, we note that HSE06 hybrid has a marginal influence on the structural properties of the metal-oxide system with respect to PBE, but compared to the latter the description of the electronic properties of the metal is slightly worse (underestimated work function). The improved description of the oxide does not show significant advantages in the combined system, also taking into account that the computational time is approximately ten time higher using hybrids. Adding vdW corrections at the GGA level results in an increase of the adhesion energy and a shortening of the interfacial distance. This is particularly true for the Grimme correction that gives d_{inter} closer to the experimental values, while optB88 gives the same results as HSE06. Furthermore, optB88 seriously overestimates the work function of Ag.

To elucidate the role of the functionals with respect to the film thickness, we have varied the number of MgO layers from 1 to 4 on the same Ag substrate. The results are shown in Fig. 3.1. For all functionals considered, the analysed properties are almost converged starting from the supported bilayer. Only the supported monolayer is slightly different; we can note a shorter interfacial distance and a more pronounced rumpling, due to the enhanced flexibility peculiar of the single layer. Also the work function change is lower for all the functionals. It is interesting to note that all functionals tested behave essentially in the same way with respect to the film thickness. In Fig. 3.1 the same trend can be identified showing that the arguments based on Table 3.2 are still valid and independent from film thickness.

3.1.4 F center on MgO(100)/Ag(100)

In Table 3.3 the results relative to the neutral oxygen vacancy on the MgO surface for 1-3 oxyde layers supported on Ag are reported . We start the discussion considering the oxygen vacancy in the top layer of the MgO(3L)/Ag system. The formation energy computed using the PBE functional is 6.13 eV with respect to 1/2 E(O_2). The analysis of the electronic levels associated with the defect shows that the most stable state is the F^0 in singlet configuration with two electrons trapped in the vacancy (see the negligible charge transfer to Ag in Table 3.3). The occupied energy levels of the F^0 lie very close to the Fermi level of Ag, and only around 0.1 eV eV lower in energy. All these results are consistent with those previously reported for a

	MgO(1L)/Ag(100)			MgO(2L)/Ag(100)			MgO3L)/Ag(100)		
	PBE	HSE06	DFT-D2	PBE	HSE06	DFT-D2	PBE	HSE06	DFT-D2
E_{form} (eV)	4.64	4.82	4.67	5.91	6.26	6.16	6.13	6.45	6.36
relax (%)	3.8	3.5	3.7	2.6	2.4	2.0	1.9	1.5	1.4
CT (e)	1.20	1.24	1.16	0.36	0.37	0.29	0.14	0.01	0.11
μ (μ_B)	0.00	0.00	0.00	0.51	0.50	0.41	0.00	0.00	0.00

Table 3.3: Properties of oxygen vacancies formed in the surface layer of MgO(nL)/Ag(100) film (n = 1-3), computed at different levels of theory: formation energy (E_{form}) with respect to 1/2 E(O_2), relaxation computed as the displacement (%) of the surface cations around the vacancy, induced interfacial charge transfer (CT, estimated from the Ag Bader charges, positive when electrons are transferred from the oxide to the metal. This value is already corrected subtracting the one, related to the metal-oxide interface, reported in table 3.2.), film magnetization (μ).

(3×3) surface unit cell and the PW91 functional [5]. Comparing the results obtained with HSE06 to PBE ones we can see that the formation energy of the defect is slightly larger using the hybrid but in general, considering the other parameters taken into account in Table 3.3, there are no visible differences between the two functionals. In fact also in this case the most stable configuration is the doubly occupied F^0 singlet state as shown in Fig. 3.2a. The most interesting information contained in Fig. 3.2a is that also using HSE06 the electronic levels associated with the defect lie very close (0.5 lower in energy) with respect to the Ag Fermi level. This indicates that the defect may be metastable with respect to a singly occupied vacancy (F^+) and the transfer of one electron to the substrate, as already demonstrated using GGA [5]. To proof the stability of the defect using the hybrid functional, we have removed one electron from the system while a uniform neutralizing background was added to keep the electrical neutrality. In Fig. 3.2b it is visible that the F electronic levels are split in two components, one below and the other above the Fermi level, confirming that it is possible to stabilize F^+ center on MgO/Ag as predicted by GGA [5]. In fact no electrons come from the substrate to keep the neutral F^0 configuration. This means that, despite the better description of the oxide energy gap using HSE06, the mutual position of the levels involved remains virtually unaltered comparing the two functionals, giving a further confirmation of the validity of the results obtained so far using standard GGA for F centers on silver-supported MgO.

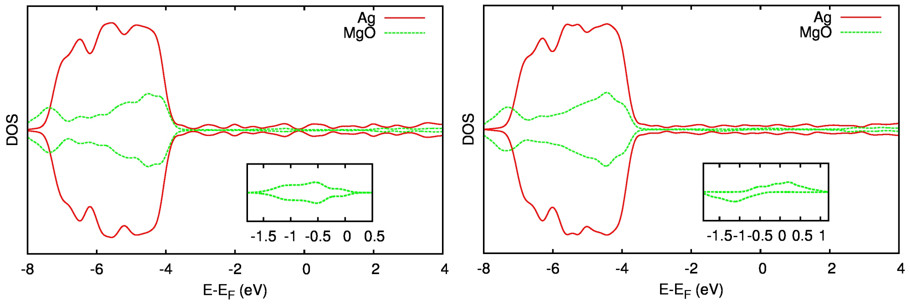

Figure 3.2: Density of states of F^0 center (left) and F^+ center (right) in MgO(3L)/Ag(100) top layer (HSE06 functional). In the inset contribution of the F center projected over nearest Mg.

We now consider the nature of the oxygen vacancy on the top layer of MgO(2L)/Ag. From table 3.3 it is visible that this configuration differs significantly from the MgO(3L) case for both HSE06 and PBE. In fact, although the formation energy is only slightly lower, the defect in the thinner film is paramagnetic, as visible from the net magnetization of the system. The increased charge transfer towards the metal, and the larger relaxation of the cations around the vacancy with respect to the thicker films are both clear evidences of the tendency to spontaneously transfer an electron to the metal substrate. The analysis of the electronic levels associated with the defect shows that the F^0 state is unstable toward the transfer of one electron to the metal substrate. The different behavior of MgO(2L)/Ag with respect to MgO(3L)/Ag is motivated by the fact that for thinner films the defect charge density can better overlap with that of the metal, and also because F^+ is stabilized by the interaction with the closer corresponding image charge in the substrate, as explained by Giordano et al. [5]. It is interesting to note that also in this case HSE06 and PBE show essentially the same behaviour.

The last case to consider is the oxygen vacancy in the MgO(1L)/Ag. As shown in Table 3.3 this case differs significantly from the thicker films, since in the monolayer the vacancy strongly interacts with the metal substrate.

The formation energy is reduced by roughly 1.5 eV for both PBE and HSE06 with respect to MgO(2-3L)/Ag; the charge transfer toward the metal and the increased cations relaxation around the vacancy (double with respect to MgO(3L)) reveal that the electrons associated with the defect are completely delocalized over the metal surface, quenching the total magnetization of the system. This is another clear example of the peculiarities of the monolayer, where the properties of the interface are dominant.

We conclude the discussion about F centers commenting the role of the vdW correction at the GGA level. In Table 3.3 we have also included the results obtained adding the Grimme correction at the PBE level. In all the cases considered the results are in line with those obtained using PBE and HSE, suggesting that vdW correction does not play a crucial role in describing F centers on Ag-supported MgO.

3.2 FeO(111)/Pt(111)

3.2.1 Computational Details

To describe Pt-supported FeO(111) we employed PBE exchange-correlation functional in DFT+U calculations (see 2.4.2) (U_{Fe}-J_{Fe} = 3 eV, systematically used in the previous studies on Pt-supported iron oxide films) in parallel with hybrid HSE06 functional .The structure of the iron oxide film has been extensively characterized by scanning tunneling microscopy (STM) and X-ray photoelectron diffraction [22–24]. The relatively large (11%) mismatch between the oxide layer and the Pt substrate results in a Moiré pattern with a periodicity of about 26 Å [23, 25]. Here, the results were obtained with pseudomorphic interface models already used in previous studies, [26, 27] which show a good agreement with few existing estimations obtained with the full Moiré cell. [28, 29]Each high-symmetry region of the full Moiré cell was represented separately by a specific small unit cell, where the two lattices were aligned and the Pt(111) substrate was laterally expanded as to match the in-plane lattice parameter of the oxide film (fixed to the experiential value of 3.10 Å). The Pt surface was represented by a slab composed of five atomic layers, with oxide films and ad-species adsorbed on one side only. A vacuum layer of at least 10 Å and the dipole correction were used. We have systematically used a (2×2) surface unit cell, as to accommodate

	a (Å)	E_g (eV)	μ_{Fe} (μ_B)	q (e)
PBE+U (U-J=3)	4.37	1.12	±3.64	±1.40
HSE03	4.34	1.84	±3.63	±1.50
HSE06	4.34	2.14	±3.63	±1.50
PBE0	4.34	2.90	±3.63	±1.50

Table 3.4: Bulk FeO characteristics obtained with different types of approximations to the exchange-correlation functional PBE+U, HSE03, HSE06, and PBE0: lattice parameter a, band gap E_g (calculated as a difference between the highest occupied and the lowest unoccupied state), magnetic moment of cations μ_{Fe}, and atomic charges q.

various possible (collinear) magnetic orderings in the iron oxide film, and to approach a low coverage limit (1/4 ML) of surface adspecies. In order to maintain the desired lattice registry at the interface and to avoid spurious relaxations induced by the imposed strain of the metal substrate, atomic coordinates were relaxed in z direction only, until forces became smaller than 0.01 eV/Å. We have verified that the above settings with a (3×3×1) Monkhorst-Pack sampling of the Brillouin zone of the (2×2) surface cell assure the convergence of calculated energy differences to 0.02 eV/FeO, of inter-atomic distances to less than 0.02 Å, and of work function to within 0.1 eV. Atomic charges were estimated within a Bader method. [30]

3.2.2 FeO and Pt bulk

Table 3.4 summarizes the essential characteristics of bulk FeO obtained within PBE+U approach and in hybrid calculations, for the undistorted cubic configuration, with antiferromagnetic coupling between {111} cationic planes. The use of hybrid functionals results in a small improvement of the calculated lattice parameter (experimental value: 4.33 Å [31]) and in a significant increase of the separation between the highest occupied and the lowest unoccupied states. As expected, the calculated E_g is very sensitive to the separation range of the Hartree-Fock exchange, the one obtained including the long-ranged part of the Fock exchange (PBE0) being by far the largest. In the following we will systematically use the HSE06 functional, which gives the band gap consistent with the experimental value of 2.4 eV [32]. Unsurprisingly, the Bader analysis reveals that hybrid approximation to the exchange-correlation functional results in a more ionic character of FeO, with only negligible differences between the considered hybrid functionals.

Bulk lattice parameter of Pt is also somewhat improved by the hybrid approximation, in non spin-polarized calculations we find 3.94 Å and 3.98 Å within HSE06 and PBE respectively, compared to the experimental value of 3.92 Å [33]. However, a net magnetization (about 0.6 μ_B/Pt) develops in hybrid calculations, showing a limited applicability of the Hartree-Fock exchange to calculation of metals. A magnetization of the same order is also present in surface layers of bare slabs used to represent the Pt(111) surface. However, the magnetic solutions are more stable by less than 0.05 eV/Pt and the spurious magnetization does not alter the calculated structural characteristics of Pt. Moreover, magnetization induced on surface Pt atoms upon deposition of FeO films fully overrides the small magnetic moments present on the bare Pt surface. Since in the following we will focus on the comparison between different FeO/Pt(111) systems only, we expect that the spurious magnetization at the clean Pt(111) surface existing in hybrid calculations hardly impact the discussed results.

3.2.3 Unsupported FeO(111) monolayer

Following the results of Ref. [8], in the comparison below we consider only the most representative magnetic orderings in the FeO(111) film: the simple ferromagnetic FM-(1×1), the row-wise antiferromagnetic RW-AFM-(2×1), and the collinear antiferrimagnetic CO-AFI-($\sqrt{3} \times \sqrt{3}$)$R30°$ structure (see Fig. 3.3). This latter can be seen as a collinear equivalent of the 120° - Néel structure, typical of triangular lattices.

The structural characteristics of the unsupported FeO(111) monolayer depend only little on the magnetic configuration. In all cases the unsupported films have a perfectly planar geometry, with the in-plane lattice parameters considerably larger than the bulk ones. While the FM structure is clearly unfavourable, the RW-AFM and the CO-AFI-($\sqrt{3} \times \sqrt{3}$) $R30°$ ones are practically isoenergetic, Tab. 3.5. The calculated Fe magnetic moments and ionic charges depend little on the particular magnetic structure and are close to the corresponding bulk values.

The modifications brought by the HSE06 approximation are relatively

	a (Å)	ΔE (eV/FeO)	μ_{Fe} (μ_{B})	q (e)
			HSE06	
FM-(1x1)	3.32	0	+3.7	±1.48
RW-AFM-(2x1)	3.29	-0.14	±3.6	±1.47
CO-AFI-($\sqrt{3} \times \sqrt{3}$)$R30^\circ$	3.29	-0.14	-3.5 +3.6 +3.6	±1.47
			PBE+U	
FM-(1x1)	3.34	0	+3.7	±1.40
RW-AFM-(2x1)	3.31	-0.15	±3.6	±1.39
CO-AFI-($\sqrt{3} \times \sqrt{3}$)$R30^\circ$	3.31	-0.15	-3.5 +3.6 +3.6	±1.38

Table 3.5: Characteristics of unsupported FeO(111) film obtained with PBE+U and HSE06 exchange-correlation functionals: in-plane lattice paramater a (Å), relative stability ΔE (eV/FeO) with respect to the FM solution (a negative value indicates a more stable structure), magnetic moment of Fe ions μ_{Fe} (μ_{B}), and atomic charges Q (e).

small. As in the case of bulk FeO, the hybrid functional makes the oxide more ionic (increase of atomic charges) and shortens somewhat the inter-atomic distances (smaller lattice parameters). We note that these modifications have practically no impact on either the formation energy of the free standing FeO film (0.18 and 0.19 eV/FeO in PBE+U and HSE06, respectively), or on the relative stability of different magnetic structures.

In the following we will systematically consider the RW-AFM-(2×1) structure only.

3.2.4 Pt-supported FeO(111) monolayer

Three high-symmetry regions along the diagonal of the full Moiré cell has been conventionally classified with respect to the position of the Fe atoms with respect to the Pt(111) substrate: in the Fe-top region the Fe atom is on-top of a surface Pt and the O atom is in the surface hollow site, in the Fe-hcp region the Fe atom is in the surface hcp site and the O atom on-top of a surface Pt, in the Fe-fcc region both Fe and O atoms are in threefold hollow sites.

	ΔE (eV/FeO)	z(FeO) (Å)	Δz (Å)	CT (e/FeO)	ΔΦ (eV)
		HSE06			
Fe-fcc	0.00	2.40	0.67	0.40	+0.46
Fe-hcp	+0.24	2.49	0.68	0.34	+0.02
Fe-top	+0.21	2.72	0.58	0.29	-0.52
		PBE+U			
Fe-fcc	0.00	2.44	0.71	0.35	+0.57
Fe-hcp	+0.20	2.48	0.72	0.31	+0.37
Fe-top	+0.24	2.78	0.60	0.22	-0.30

Table 3.6: Structural and electronic characteristics of FeO(111)/Pt(111) as function of interface lattice register obtained with PBE+U and HSE06 exchange-correlation functionals: relative stability ΔE with respect to the most stable Fe-fcc register, FeO adsorption height z(FeO), rumpling of the oxide film Δz, electron transfer towards the Pt substrate *CT* (positive values correspond to a negative charging of Pt), and FeO-induced change of the Pt(111) work function ΔΦ. As a reference, the calculated Φ for bare Pt(111) surface are 5.48/5.40 eV in HSE06/PBE+U.

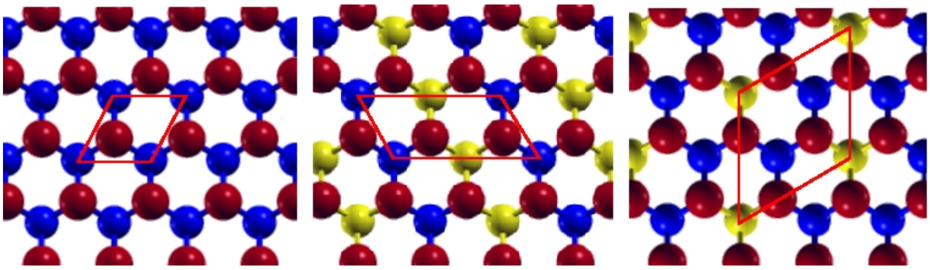

Figure 3.3: Magnetic structures of the FeO(111) monolayer: (left) ferromagnetic FM-(1×1), (center) row-wise RW-AFM-(2×1), (right) collinear antiferrimagnetic CO-AFI-($\sqrt{3}\times\sqrt{3}$)$R30°$. Red spheres, O atoms; yellow and blue spheres, Fe atoms with opposite magnetization.

Table 3.6 gives the main structural and electronic characteristics of the FeO(111) film supported on the Pt(111) substrate, with lattice registers representing the three different regions of the Moiré cell. Due to the large electronegativity of Pt, electrons are transferred from the FeO film towards the metal substrate (positive *CT*). [8] By an electrostatic coupling mechanism, this electron transfer induces a rumpling of the FeO film, with anions relaxing outwards (positive Δz). [34] Both effects are stronger in the Fe-fcc and Fe-hcp regions, where FeO film adsorbs closer to the Pt surface. They are considerably weaker in the Fe-top region where, due to Fe-Pt repulsion, the adsorption height z(FeO) is larger and, as a consequence, both interface electron transfer *CT* and FeO film rumpling Δz become smaller. [8] FeO film reduces the work function of the bare Pt(111) surface ($\Delta\Phi < 0$) in the Fe-top region, where the negative contributions due to compression of electron density and to interface charge transfer are not overridden by that due to the film rumpling (the smallest Δz). In Fe-fcc and Fe-hcp regions where Δz is larger, ΔΦ becomes positive. [8]

Compared to the PBE+U results, the HSE06 approximation brings relatively small modifications. In average, the FeO adsorption height z(FeO) is a slightly smaller (-1%), the electron transfer towards the metal *CT* is larger (+17%), and the rumpling of the FeO film Δz is smaller (-6%). Despite the shortening of interface distance z(FeO), the increase of the charge transfer *CT*, and the reduction of film rumpling Δz, HSE06 calculations bring an overall 0.2 eV shift of the oxide-induced modification of the work function

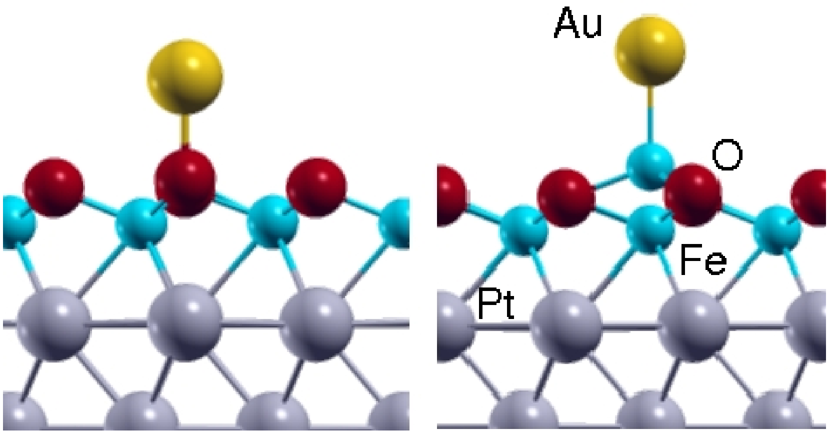

Figure 3.4: Direct O-top (left) and flipped Fe-top (right) Au adsorption configurations.

$\Delta\Phi$ towards more negative (Fe-top) and less positive (Fe-hcc, Fe-hcp) values.

We stress that, beyond these average trends, the fine film behaviour as function of the lattice registry at the interface follows closely the induced polarity pattern already derived from GGA+U calculations [8, 34] and described above. Also, the modifications of the atomic and electronic structures of the FeO/Pt interface do not alter the calculated separation energies (1.19 and 1.21 eV/FeO in the Fe-fcc region, respectively with PBE+U and HSE06 approach), nor the relative stability of the three high symmetry regions. Indeed, the Fe-fcc region remains by far the most favourable, while the less favourable Fe-hcp and Fe-top ones are nearly degenerate energetically. Also the FeO-induced modulation of the surface work function $\Delta\Phi$ gives a very similar pattern within the two studied approximations to the exchange-correlation functional, with $\Delta\Phi$ being the most positive and the most negative in respectively Fe-fcc and Fe-top regions.

3.2.5 Au adsorption on FeO(111)/Pt(111)

An ordered array of Au adatoms decorating the FeO(111)/Pt(111) Moiré pattern has been observed in low-temperature STM measurements and the ordering effect has been attributed to a spontaneous charging of the deposited Au atoms. [6, 35] In agreement with the existing DFT+U calcula-

	HSE06			PBE+U		
	E_b (eV)	q_{Au} (e)	Δz (Å)	E_b (eV)	q_{Au} (e)	Δz (Å)
top-Fe (d)	0.17	+0.39	+0.94	0.44	+0.30	+0.94
top-Fe (f)	0.92	-0.34	-0.64	1.14	-0.31	-0.66
top-O (d)	0.47	+0.38	+0.90	0.72	+0.26	+0.92
top-O (f)	0.19	-0.27	-0.51	0.54	-0.28	-0.57

Table 3.7: Structural and electronic characteristics of Au adsorption on FeO(111)/Pt(111) in the Fe-hcp region, obtained with the two functionals: binding energy (E_b), Bader charge of the Au adatom (q_{Au}), and local film rumpling (Δz). As reference, for bare substrate in FeO-hcp region, $\Delta z = 0.68/0.72$ Å (HSE06/PBE+U), Tab. 3.6. Adsorption geometry with Au on-top surface cation (Fe-top) and anion (O-top) have been considered, (d) and (f) refer to direct and flipped adsorption mode.

tions, [6,34,36] we find that Au adatoms spontaneously charge upon adsorption in one of two qualitatively different adsorption modes, Tab. 3.7.

In the direct (d) adsorption mode Au charges positively and induces an increase of local rumpling in the FeO film (positive Δz). Conversely, in the flipped (f) adsorption mode Au charges negatively and provokes a local reversal of the film rumpling (negative Δz) due to a substantial outward relaxation of the cations. In both cases, the distortion of the FeO film can be seen as a structural response to the adsorbate charging, such that the induced dipole moment opposes and partially compensates the one due to the electron exchange between the substrate and the adsorbate. [34] The calculations show that in Fe-hcp region, both direct and flipped adsorption modes correspond to local minima for Au adsorbed on-top both surface anions (O-top) and cations (Fe-top). Flipped Fe-top configuration, with negative charging of Au adatom is found to be the most favoured energetically (see Fig. 3.4).

The four considered adsorption configurations can also be stabilized in HSE06 calculations, where their characteristics differ only little from those obtained from PBE+U. The main difference concerns the direct adsorption mode where, regardless the adsorption site, the positive charging of

Au adatoms (direct adsorption mode) is considerably stronger and induces a larger increase of local film rumpling in HSE06 calculations. Conversely, in case of flipped adsorption mode, the Au charging is only little altered and the inversion of the local film rumpling is somewhat less pronounced. Finally, while Au binding energies E_b are systematically smaller in HSE06 calculations, the order of relative stability of the four considered adsorption configurations remains unaltered.

3.3 Conclusions

In this chapter we have considered two metal supported oxide systems, MgO/Ag and FeO/Pt, which have already been extensively studied by both theory and experiments, as case studies to understand to what extent refined methods beyond standard DFT can affect the description of thin oxide films on metals. We have shown that while the hybrid functionals improve the description of structural and electronic properties of the oxides (in particular band gaps and lattice parameters), their overall impact on the calculated stability and reactivity characteristics is practically negligible in the two considered combined systems. Moreover, hybrid functionals show limited applicability in describing metals, as it is well highlighted by Pt that is predicted to be ferromagnetic by HSE06. For the MgO/Ag case we have also considered the inclusion of vdW interactions at the PBE level. The main effect introduced by vdW forces is an increase of the film adsorption energy and, therefore, a reduction of the interfacial distance that gets closer to the experimental value. However, the latter effects do not alter significantly the analyzed properties, and then the results obtained with the standard DFT are still valid. In conclusion, in this chapter we have given a further confirmation of the validity of the results obtained so far using GGA in describing Ag-supported MgO and Pt-supported FeO.

Bibliography

[1] J. Hafner, *J. Comput. Chem.* **29**, 2044 (2008).

[2] A.M. Ferrari and G. Pacchioni, *J. Phys. Chem.* **99**, 17010 (1995).

[3] P.V. Sushko, A.L. Shluger and C.R.A Catlow, *Surf. Sci.* **450**, 153 (2000).

[4] M. Sterrer, M. Heyde, M. Novicki, N. Nilius, T. Risse, H.P. Rust, G. Pacchioni and H.-J. Freund, *J. Phys. Chem. B* **110**, 46 (2006).

[5] L. Giordano, U. Martinez, G. Pacchioni, M. Watkins and A.L. Shluger, *J. Phys. Chem. C* **112**, 3857 (2008).

[6] L. Giordano, G. Pacchioni, J. Goniakowski, N. Nilius, E. D. L. Rienks, and H.-J. Freund, *Phys. Rev. Lett.* **101** 026102 (2008).

[7] M. Sterrer, E. Fischbach, T. Risse, H.-J. Freund, *Phys. Rev. Lett.* **94**, 186101 (2005).

[8] L. Giordano, G. Pacchioni, J. Goniakowski, N. Nilius, E.D.L. Rienks and H.-J. Freund, *Phys. Rev. B* **76** 075416 (2007).i

[9] J. Klimes, D.R. Bowler, and A. Michaelides, *Phys. Rev. B* **83**, 195131 (2011).

[10] M. Dion, H. Rydberg, E. Schröder, D.C. Langreth and B.I. Lundqvist, *Phys. Rev. Lett.* **92**, 246401 (2004).

[11] J. Klimes, D.R. Bowler and A. Michaelides, *J. Phys.: Cond. Matt.* **22**, 022201 (2010).

[12] R.W.G Wyckoff, Crystal Structure, Wiley, New York (1963).

[13] D.M. Roessler and D.R. Huffman, Handbook of optical constants of solids II, ed. Palik, Academy Press, New York (1998).

[14] L. Liu and W.A. Bassett, *J. Appl. Phys.* **44**, 1475 (1973).

[15] J. Paier, M. Marsman, K. Hummer, G. Kresse, I. C. Gerber and J. G. Ángyán, *J. Chem. Phys.* **124**, 154709 (2006).

[16] L. Giordano, F. Cinquini and G. Pacchioni, *Phys. Rev. B* **73**, 045414 (2005).

[17] S. Prada, U. Martinez and G. Pacchioni, *Phys. Rev. B* **78**, 235423 (2008).

[18] T. König, G. H. Simon, H.-P. Rust and M. Heyde, *J. Phys. Chem. C* **113**, 11301 (2009).

[19] C. Giovanardi, A. di Bona, T.S. Moia, S. Valeri, C. Pisani, M. Sgroi and M. Busso, *Surface Science* **505**, L209 (2002).

[20] Yu, F. Zhukovskii, E.A. Kotomin, P.W.M. Jacobs and A.M. Stoneham, *Phys.Rev.Lett.* **84** 1256 (2000).

[21] A.M. Flank, R. Delaunay, P. Lagarde, M. Pompa and J.Jupille, *Phys.Rev.B* **53** (1996) R1737 (1996).

[22] H.C. Galloway, J.J. Benitez and M. Salmeron, *Surf. Sci.* **298**, 127 (1993).

[23] Y.J. Kim, C. Westphal, R.X. Ynzunza, H.C. Galloway, M.B. Salmeron, M.A. Van Hove and C.S. Fadley, *Phys. Rev. B* **55**, R13448 (1997).

[24] W. Ranke, M. Ritter and W. Weiss, Phys. Rev. B 60, 1527 (1999).

[25] G.H. Vurens, M. Salmeron and G.A. Somorjai, *Surf. Sci.* **201**, 129 (1988).

[26] F. Ringleb, Y. Fujimori, H.F. Wang, H. Ariga, E. Carrasco, M. Sterrer, H.J. Freund, L. Giordano, G. Pacchioni and J. Goniakowski, *J. Phys. Chem. C* **115** 19328 (2011).

[27] L. Giordano, M. Lewandowski, I.M.N. Groot, Y.N. Sun, J. Goniakowski, C. Noguera, S. Shaikhutdinov, G. Pacchioni and H.J. Freund, *J. Phys. Chem. C* **114** 21504 (2010).

[28] W. Zhang, Z. Li, Y. Luo, J. Yang, *J. Phys. Chem. C* **113** 8302 (2009).

[29] L.R. Merte, L.C. Grabow, G. Peng, J. Knudsen, H. Zeuthen, W. Kudernatsch, S. Porsgaard, E. Laegsgaard, M. Mavrikakis and F. Besenbacher, *J. Phys. Chem. C* **115** 2089 (2011).

[30] R.F.W. Bader, *Chem. Rev.* **91**, 983 (1991); G. Henkelman, A. Arnaldsson and H. Jonsson, *Comput. Mater. Sci.* **36**, 354 (2006); W. Tang, E. Sanville and G. Henkelman, *J. Phys.: Condens. Matter* **21**, 084204 (2009).

[31] T. Katsura, B. Iwasaki, S. kimura and S. Akimoto, *J. Chem. Phys.* **47**, 4559 (1967).

[32] H.K. Bowen, D. Adler and B.H. Auker, *J. Solid State Chem.* **12**, 355 (1975).

[33] Y. Waseda, K. Hirata and M. Ohtani, *High Temp. High Pressures* **7**, 221 (1975).

[34] J. Goniakowski, C. Noguera, L. Giordano and G. Pacchioni, *Phys. Rev. B* **80** 125403 (2009).

[35] N. Nilius, E.D.L. Rienks, H.P. Rust and H.-J. Freund, *Phys. Rev. Lett.* **95** 066101 (2005).

[36] R. Ouyang and W.X. Li, *Phys. Rev. B* **84** 165403 (2011).

Chapter 4

Strain-induced formation of ultrathin mixed-oxide films

The growth of crystalline, atomically flat and stoichiometric oxide layers depends on a number of structural and thermodynamic preconditions. The most important one is a good lattice match between the metal surface and the oxide film, which forms the basis for the development of an epitaxial network of interfacial metal-oxygen bonds. [1–3] Other factors are the electronegativity of the support that controls charge transfer processes, [4, 5] the metal affinity toward oxygen and its thermal stability, defining the maximum temperature to equilibrate the system. Structural flexibility of the thin film is another important parameter, as it determines the ability of the overlayer to compensate misfit-induced lattice strain. Several strain-relaxation mechanisms have been identified for metal-oxide interfaces. The most prominent ones are plastic lattice deformations, e.g., misfit dislocations, grain boundaries, and mosaics. [6, 7] The presence of line defects is, however, incompatible with many applications of thin-film systems, as they alter the electronic and chemical nature of the film and open communication channels with the metal below. Alternative relaxation mechanisms rely on modifications of the stoichiometry and crystal structure of the oxide film. NiO, for example, was found to develop an oxygen-poor interface structure,

---

The results of this chapter have been reported in the following publication: X. Shao, P. Myrach, N. Nilius, H.-J. Freund, U. Martinez, S. Prada, L. Giordano, G. Pacchioni., “Strain-induced formation of thin mixed-oxide films”, *Phys. Rev. B* **83**, 245407 (2011).

which better matches the lattice constant of the Pd(100) support. [8] Other films, such as $Al_{10}O_{13}$, [9] Pd_4O_5, [10] TiO_x , [11] and ZnO films, [12] adopt crystal phases that are unknown for the respective bulk materials and only stabilized by the metal surface underneath. Common to all those mechanisms is their self-terminating nature, which means that the oxide growth stops at a critical thickness because the thin-film phase cannot be transformed into a bulk structure.

In this chapter, we discuss a yet unknown principle for strain relaxation in a thin oxide film. A good lattice match with the metal below is hereby achieved by incorporating substrate ions into the oxide overlayer, as demonstrated for CaO deposited onto a Mo(001) surface. Upon annealing, a well-ordered ternary Ca-Mo-O phase forms that has a similar lattice parameter as the substrate and consequently grows in a pseudomorphic mode. In contrast, the comparable MgO/Mo(001) system remains phase separated even at high temperature, because the strain-induced stimulus for interfacial mixing is much smaller.

The results reported in this chapter are based on a collaboration with the group of Prof. Freund at the Fritz-Haber-Institut in Berlin, who provided all the experimental data here reported. The experimental evidences are presented and commented first, and secondly calculations are introduced to shed light over the nature of the observed mixed Ca-Mo phase.

4.1 Experimental evidences

4.1.1 Experimental details

The experiments have been performed in an ultrahigh vacuum chamber equipped with a liquid-nitrogen-cooled scanning tunneling microscope (STM) and a low-energy electron diffraction (LEED)/Auger unit for chemical analysis. The Mo(001) substrate is cleaned by Ar^+ sputtering, annealing in oxygen and flashing to 2000 K. Ca and Mg are vapor deposited onto the clean Mo surface in an O_2 ambience of 5×10^{-7} mbar at room temperature. The as-grown oxide films are stoichiometric, but amorphous as inferred from the absence of any LEED spots. Crystallization can be induced by vacuum annealing to temperatures as high as 1150 K.

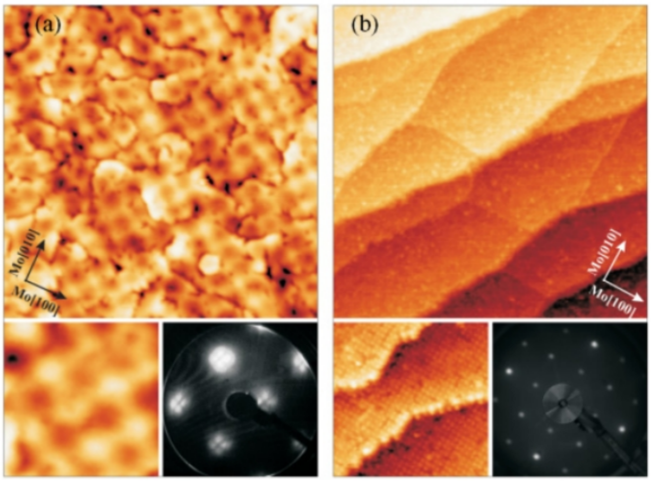

Figure 4.1: Overview (70×70 nm^2) and close-up (17×17 nm^2) STM images of (a) 3-ML Mg and (b) 3-ML Ca grown in an O_2 atmosphere on Mo(001) and annealed to 1000 K (U_s = 3.0 V, I_t = 50 pA). The right panels display the corresponding LEED patterns taken at 75-eV electron energy.

4.1.2 Results

Figure 4.1 provides information on the structure and morphology of 3-4 monolayer (ML)-thick MgO and CaO films annealed to 1000 K. Both films are atomically flat and completely cover the Mo surface. Close-up STM images of the MgO/Mo system reveal a regular square pattern with 55 Å periodicity, as described in [7] [Fig. 4.1(a)]. It is assigned to a coincidence lattice with 19 MgO unit cells overgrowing 18 Mo cells, whereby the MgO[110] direction aligns with the Mo[100]. The contrast modulation in the STM originates from a different stacking sequence at the interface. [13, 14] The energetically favored structure with O sitting above the Mo atoms appears dark, whereas the Mg-Mo stacking regions show up with bright contrast due to an enlarged interfacial distance. The coincidence lattice develops in order to compensate the -5.3% lattice mismatch between bulk MgO (d_{O-O} = 2.98 Å) and Mo(001) (d_{Mo-Mo} = 3.15 Å) and removes 90% of the initial misfit strain. The remaining strain is released in the form of grain boundaries and dislocation lines that appear as dark lines in the STM images [Fig. 4.1(a)]. The proposed relaxation mechanism is in line with the LEED pattern of the

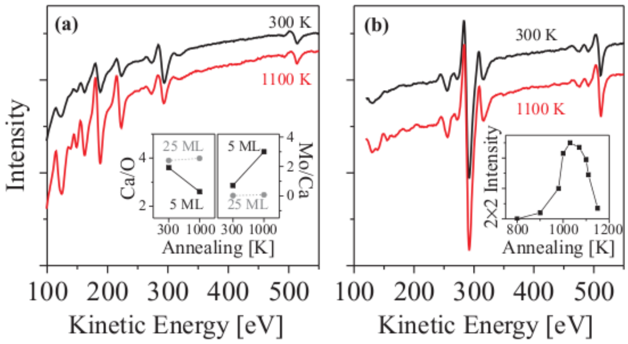

Figure 4.2: (a)Auger spectra of 5-ML-thick CaO films before (black) and after (red) annealing to 1100 K. (b) Same data for a 25-ML-thick film. Insets (a) and (b) display the development of the Ca/O and Mo/Ca peak ratios as well as the intensity variation of the (2×2) LEED spots upon annealing.

4-ML MgO/Mo(001) film, in which each fundamental spot is split into four satellites. Those satellites reflect some faceting of the surface, arising from the alternation of O-Mo and Mg-Mo stacking domains in the film. [7] The coincidence lattice, on the other hand, is not resolved in reciprocal space due to the limited coherence length of our LEED system.

For CaO films (d_{O-O} = 3.4 Å), even more pronounced relaxation effects are expected due to the +8.1% lattice mismatch with the Mo(001). However, the expected low structural quality of the film is not revealed in the experiments [Fig. 4.1(b)]. The STM images display wide terraces covered with a perfect 6.3×6.3 Å^2 square lattice that corresponds to a (2×2) superstructure with respect to Mo(001). The height of the lattice maxima amounts to 0.8 Å and depends only weakly on the applied sample bias. Apart from Mo-induced step edges, no line defects are detected, which is in sharp contrast to the MgO/Mo system. The high structural quality of the film becomes manifest also in a perfect (2×2) LEED pattern that shows no sign of disorder or faceting. Apparently, annealed CaO films are commensurate with the Mo support and therefore display an extremely low defect density. This unexpected finding raises the question on the strain-relaxation mechanism in this heavily mismatched metal-oxide system.

Elastic and plastic deformations of the CaO lattice are ruled out as possible means to compensate the lattice mismatch. Whereas unreasonably high energies are required to elastically compress the rocksalt lattice towards registry with the Mo, the "plastic route" is discarded because neither a defect network nor a coincidence structure is observed in the experiment. Furthermore, none of those mechanisms would explain the (2×2) superstructure, as the Mo(001) and the CaO(001) unit cells have comparable dimensions and should rather induce a (1×1) pattern. Therefore, alternative oxide cells that have square symmetry have been considered, but a two times larger in-plane lattice parameter. Those new building blocks may differ in their atomic structure and/or stoichiometry from classical rocksalt CaO.

To analyze the film stoichiometry first, Auger spectroscopy at 45° incidence angle have been performed (Fig. 4.2). A reference spectrum was obtained for a 25-ML-thick CaO/Mo film prepared at room temperature and post-annealed to 1100 K. As expected, only Ca and O peaks at 250, 290 and 510 eV, respectively, are observed for thick films and the Mo signature is completely suppressed. The intensity ratio of the two peaks amounts to (3.9±0.1) and is identical for as-grown and annealed samples. This Ca/O peak ratio is therefore taken as a fingerprint for stoichiometric CaO. On 3-4-ML films, the Mo Auger transitions at 160, 190, and 220 eV become visible as well, in agreement with the free mean path of electrons in bulk CaO. The as-grown films are still characterized by a Ca/O ratio of 3.7, indicative for a one-to-one stoichiometry, but absolute peak intensities are smaller. This ratio gradually declines to 3.6 when annealing the sample to 900 K and undergoes a sudden drop to 2.6 at 1000 K. Similarly, the Mo signal increases slowly until 900 K, but rises sharply for annealing temperatures above 1000 K. This temperature-dependent Auger series suggests a phase transition in the CaO layer, in which a part of Ca ions is replaced by Mo. A quantitative analysis of the peak intensities indicates the new film stoichiometry to be close to Ca_3MoO_4, corresponding to an exchange of 25% of the Ca ions. Partial desorption or dewetting of the film is discarded as possible explanation for the modified Auger response, because the O signal remains almost constant across the transition.

This stoichiometry change is closely connected with the appearance of the (2×2) LEED pattern, reflecting the structural side of the phase transition. The development of the new crystal structure can be monitored via the intensity of the (2x2) superstructure spots measured as a function of temperature [Fig. 4.2(b)]. The extra spots appear at 900 K, reach their intensity maximum at 1000 K when the new phase is fully developed, and attenuate above 1100 K due to film desorption. It should be noted that MgO films on Mo(001) do not exhibit a comparable behavior and maintain their structure and stoichiometry until desorption at 1150 K.

4.2 Computational details

To analyze the thermodynamic stability of the resulting oxide phases, spin-polarized density-functional theory (DFT) calculations have been performed with the VASP code, using the generalized gradient approximation, the PW91 exchange-correlation functional, [15] a plane-wave basis set with 400 eV energy cutoff, and the projector augmented wave method (see section 2.3). The films are modeled with (2×2) supercells containing three to four oxide and four Mo layers, separated by 10 Å of vacuum from the next slab.

4.3 Results

To elucidate the nature of the new phase, we have performed DFT calculations on potential Ca-Mo-O structures. We first considered known bulk-phases of the three elements, in particular the $CaMoO_3$ perovskite and $CaMoO_4$ powellite structure with Mo ions sitting in octahedral and tetrahedral positions, respectively. [16, 17] The properties of both phases could not be reconciled with the experimental data for several reasons. First, the size of their basal cells (5.5×5.5 $Å^2$ in perovskite and 5.2×5.2 $Å^2$ in powellite) is clearly smaller than the (2×2) cell (6.3×6.3 $Å^2$), which makes substantial lattice deformations necessary again. Second, the bulk structures comprise a number of distinguishable layers along their c axis, which should result in different surface terminations but has not been observed experimentally. And third, the high oxygen content of the bulk phases is not compatible with the Auger data obtained for our thin films.

In a next attempt, we have modified the CaO stoichiometry by removing 25% of the Ca or O ions from the interface plane. The formation of non-stoichiometric interfaces has been suggested as a possible strain-relaxation mechanism for other metal-oxide systems, e.g., NiO on Pd(001). [8] Our DFT calculations revealed, however, a higher free energy of the O-poor and Ca-poor vacancy structures compared to a strained but stoichiometric CaO film. While a Ca_4O_3 vacancy structure with a (2x2) cell can be stabilized on Mo(001) only at very reducing conditions, the oxygen-rich Ca_3O_4 phase is always unstable against Mo interdiffusion into the vacancy sites. We note that the instability of vacancy structures is in line with the irreducible nature of CaO.

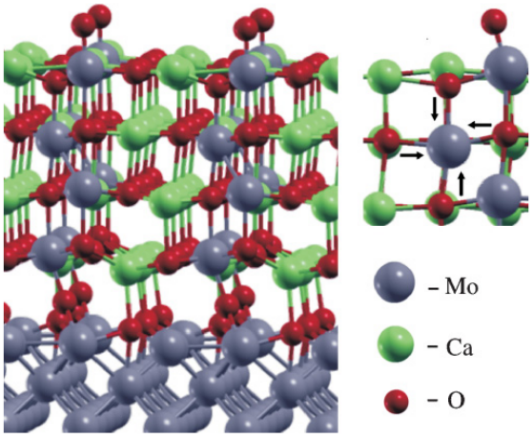

Figure 4.3: Structure model of a Mo=O terminated Ca_3MoO_4 mixed film with an oxidized Mo plane at the interface to the Mo(001) support [O/Ca_3MoO_4(4L)/O/Mo phase]. The right panel displays the inward relaxation of O ions next to a Mo impurity (side view), as marked by small arrows.

We therefore favor another model that assumes intermixing of Mo into the CaO rocksalt structure, as already suggested by the Auger results. In the model, 25% of the Ca ions are replaced by Mo, resulting in a Ca_3MoO_4 stoichiometry (Fig. 4.3). Adjacent MoO_6 octahedrons share hereby not more than two oxygen ligands, a constraint that leads to the formation of a (2x2) unit cell. In order to determine the stability of this mixed oxide with respect to a phase-separated CaO/Mo reference system, we have calculated the Gibbs free energy $\Delta\gamma$ per surface area S as a function of the oxygen chemical potential μ_0 according to $\Delta\gamma(T,p) = [G_{mix} - G_{sep} - n_O\Delta\mu_O(T,p)]/S$. Here, G_{mix} and G_{sep} are the free energies of the mixed and the phase-separated system, respectively, being approximated from the total DFT energy at zero K, and n_O is the number of additional oxygen atoms with respect to the reference system. The change in the O_2 chemical potential

$\Delta\mu_O(T,p) = \mu_O - \frac{1}{2}E(O_2)$, which we refer to half of the total energy of an oxygen molecule $E(O_2)$, can be related to temperature T and O_2 partial pressure p. [18] To mimic the experimental situation, the presence of chemisorbed oxygen at the interface and molybdyl (Mo=O) groups at the surface is considered as well. In all models, the total number of Ca and Mo atoms is kept constant and only their distribution in the different planes of the slab is altered.

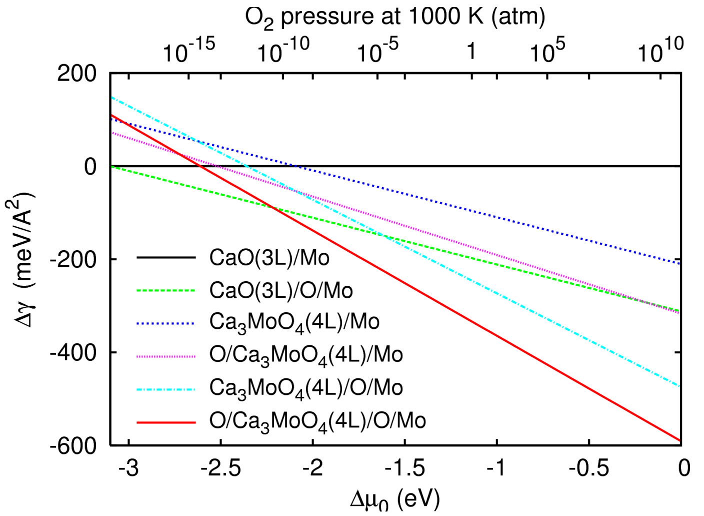

Figure 4.4: Gibbs-energy change per surface area for the different films considered in the text. The reference system is a three-layer CaO film grown on Mo(001). The oxygen chemical potential is converted into an oxygen partial pressure at T = 1000 K (upper scale).

The stability plots for different model structures are shown in Fig. 4.4. The phase-separated CaO (3L)/Mo phase is stable only at extremely oxygen-poor conditions ($\Delta\mu_O <$ -3.1 eV). In the range between -3.1 eV $< \Delta\mu_O <$ -2.2 eV, the most stable phase consists of a three-layer CaO film grown on an oxidized Mo layer [CaO(3L)/O/Mo], while a mixed Ca_3MoO_4(4L)/Mo phase is still higher in energy. The formation of surface Mo=O groups [O/Ca_3MoO_4(4L)/Mo] stabilizes the mixed phase and, at $\Delta\mu_O >$ -2.2 eV and in presence of chemisorbed oxygen at the interface, this phase becomes indeed the most stable one. We note that a simple square arrangement is assumed for the chemisorbed O ions at the interface, while the exploration of more sophisticated geometries is beyond the scope of this study. The stability regime of the O/Ca_3MoO_4(4L)/O/Mo matches the experimental preparation conditions, suggesting that interfacial mixing is indeed thermodynamically favorable. The anticipated formation of Mo=O groups that play a crucial role in stabilizing the mixed phase even explains the large corrugation revealed in atomically resolved STM images. While a corrugation of 0.8 Å seems incompatible with a flat (001) rocksalt plane, it perfectly fits into the picture of double-bonded oxygen ions attached to the surface Mo species (1.74 Å bond length). In fact, a similar surface corrugation has been observed for V_2O_3(0001) covered with V=O groups. [19]

One driving force for the formation of a mixed oxide is certainly the higher oxygen content of the new phase due to oxidation of Mo atoms from the substrate. [19, 20] However, Mo interdiffusion also presents an effective means to release the interfacial strain induced by the deviating Mo and CaO lattice parameters. Whereas a metal-oxygen bond length in CaO is of the order of 2.4 Å, it shortens to 1.9 Å in typical Mo-O compounds. A similar trend is revealed for the ionic radii that decrease from 115 pm for Ca^{2+} to 83 pm for Mo^{2+}. [21] Alternating Ca and Mo cations in a mixed oxide thus leads to a reduction of the lattice constant, a behavior that was verified with calculations performed on unsupported four-layer-thick slabs. While CaO has a (2×2) lattice parameter of 6.69 Å (bulk value 6.78 Å), this value reduces to 6.42 Å for the Ca_3MoO_4 film. As a result, the lattice mismatch with the Mo(001) surface decreases from 8% to 1.7%, enabling a pseudomorphic growth of the mixed oxide film. The interdiffusion of Mo into the CaO matrix can thus be considered as “chemical” means to compensate misfit strain in a metal-oxide system.

With the same arguments, the absence of intermixing at the MgO/Mo(001) interface can be rationalized. Also here, a mixed Mg_3MoO_4 film would be thermodynamically stable with respect to the phase-separated system due to oxidation of extra Mo atoms from the support. However, the stimulus related to misfit strain largely vanishes, as the lattice mismatch decreases only from 5.4% to 3.8% when replacing a quarter of the Mg ions with Mo. Furthermore, Mo diffusion inside a dense MgO lattice might be harder than in the more spacious CaO structure. We note, however, that substantial quantities of Mo have been detected with electron-paramagnetic resonance spectroscopy in Mo-supported MgO films treated at high temperature, suggesting that the formation of a mixed Mg-Mo oxide might be mainly kinetically hindered. [22]

For the same kinetic reasons, the formation of a mixed Ca-Mo oxide film is restricted to a region close to the metal-oxide interface. Results provided by the group of Prof. Freund also show that even for annealing temperatures as high as 1000 K, the Mo supply from the support stops at a critical film thickness due to the low diffusion rates. They indeed observe a self-terminating growth of the mixed oxide film. Beyond 4-5-ML nominal thickness, three-dimensional islands develop on top of the surface, which display the typical LEED and Auger signature of pristine rocksalt CaO (Figure 4.5). With the absence of Mo in the film, also the lattice mismatch with the substrate appears again, driving the system into a 3D Volmer-Weber mode.

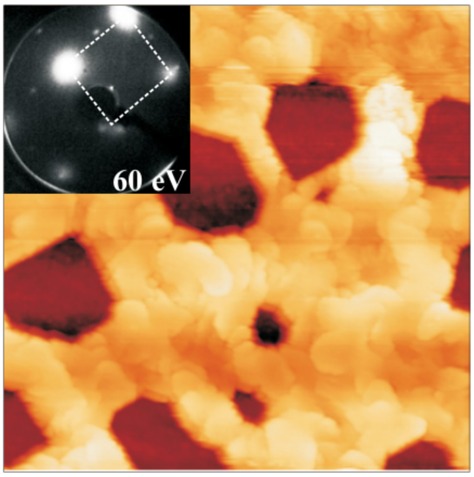

Figure 4.5: STM image of a 15-ML-thick CaO film deposited onto Mo(001) (U_s =3.6V, I_t =25 pA, 150x150nm^2). The Ca_3MoO_4 phase remains visible in the holes of the three-dimensional CaO patches. The inset shows the corresponding LEED pattern with a (1x1) unit cell.

4.4 Conclusions

In this chapter we have demonstrated that interdiffusion of substrate ions into a thin oxide film is an effective means to release the lattice strain imposed by the support. The mechanism becomes active in compressively strained oxides if the substrate ions occupy less space than the intrinsic cations of the film. This is the case for CaO deposited onto Mo(001), that gives rise to the formation of well-ordered, atomically flat Ca_3MoO_4 films at high temperature. A similar behavior might also be expected for films under tensile strain, when structural relaxation is realized by the interdiffusion of larger ions from the support. Intermixing is not observed for metal-oxide systems below a critical lattice mismatch, as demonstrated for MgO films on Mo(001) in this study. The strain-induced formation of mixed-oxide structures provides insights into the characteristics of oxide growth on metal surfaces and might explain several yet unsolved growth phenomena. Moreover, interfacial strain might be exploited to prepare mixed-oxide films with extremely high structural quality, in particular if a simple co-deposition of the constituents does not yield the desired structures.

Bibliography

[1] S. A. Chambers, *Surf. Sci. Rep.* **39**, 105 (2000); C. C. Chusuei, X. Lai, K. Luo, and D. W. Goodman, *Top. Catal.* **14**, 71 (2001).

[2] M. Bäumer and H.-J. Freund, *Prog. Surf. Sci.* **61**, 127 (1999).

[3] S. A. Chambers, T. T. Tran, T. A. Hileman, and T. A. Jurgens, *Surf. Sci.* **320**, L81 (1994).

[4] J. Goniakowski and C. Noguera, *Interface Sci.* **12**, 93 (2004).

[5] L. Giordano, F. Cinquini, and G. Pacchioni, *Phys. Rev. B* **73**, 045414 (2006).

[6] J. Wollschläger, D. Erdos, H. Goldbach, R. Hopken, and K. M. Schröder, *Thin Solid Films* **400**, 1 (2001); J. Schoiswohl, W. Zheng, S. Surnev, M. G. Ramsey, G. Granozzi, S. Agnoli, and F. P. Netzer, *Surf. Sci.* **600**, 1099 (2006).

[7] S. Benedetti, H. M. Benia, N. Nilius, S. Valeri, and H.-J. Freund, *Chem. Phys. Lett.* **430**, 330 (2006); S. Benedetti, P. Torelli, S. Valeri, H. M. Benia, N. Nilius, and G. Renaud, *Phys. Rev. B* **78**, 195411 (2008).

[8] S. Agnoli, M. Sambi, G. Granozzi, A. Atrei, M. Caffio, and G. Rovida, *Surf. Sci.* **576**, 1 (2005).

[9] G. Kresse,M. Schmid, E. Napetschnig, M. Shishkin, L. Kohler, and P. Varga, *Science* **308**, 1440 (2005).

[10] H. Gabasch, W. Unterberger, K. Hayek, B. Klotzer, G. Kresse, C. Klein, M. Schmid, and P. Varga, *Surf. Sci.* **600**, 205 (2006).

[11] Q. H. Wu, A. Fortunelli, and G. Granozzi, *Int. Rev. Phys. Chem.* **28**, 517 (2009).

[12] C. Tusche, H. L. Meyerheim, and J. Kirschner, *Phys. Rev. Lett.* **99**, 026102 (2007).

[13] H. M. Benia, P. Myrach, N. Nilius, and H.-J. Freund, *Surf. Sci.* **604**, 435 (2010).

[14] C. Noguera, J. Godet, and J. Goniakowski, *Phys. Rev. B* **81**, 155409 2010).

[15] J. P. Perdew, J. A. Chevary, S. H. Vosko, K. A. Jackson, M. R. Pederson, D. J. Singh, and C. Fiolhais, *Phys. Rev. B* **46**, 6671 (1992).

[16] O. Y. Gorbenko, S. V. Samoilenkov, I. E. Graboy, and A. R. Kaul, *Chem. Mater.* **14**, 4026 (2002).

[17] W. S. Cho, M. Yashima, M. Kakihana, A. Kudo, T. Sakata, and M. Yoshimura, J. Am. Ceram. Soc. 80, 765 (1997).

[18] K. Reuter and M. Scheffler, *Phys. Rev. B* **65**, 035406 (2001).

[19] S. Surnev, M. G. Ramsey, and F. P. Netzer, *Prog. Surf. Sci.* **73**, 117 (2003).

[20] C. Dri, C. Africh, F. Esch, G. Comelli, O. Dubay, L. Koehler, F. Mittendorfer, G. Kresse, P. Dudin, and M. Kiskinova, *J. Chem. Phys.* **125**, 094701 (2006).

[21] CRC Handbook of Chemistry and Physics, edited by D. R. Lide (CRC Press, Boca Raton, 2010).

[22] A. Gonchar, PhD Thesis, TU Berlin, Berlin, (2011).

Chapter 5

Tailoring the shape of Au ad-particles by doping CaO

In the introduction (see section 1.2) we pointed out that optimizing the structural and electronic properties of supported metal catalysts, to augment their activity and selectivity, is a goal of catalysis research. Various key parameters that govern the catalytic performance have been identified to date, for example, selecting proper material combinations and maximizing the dispersion of the active species. Special emphasis was placed on controlling the properties of the metal centers on the catalyst surface, that is, their size, shape, crystallinity, and charge state. In gold catalysis, for example, small raft-like deposits with amorphous structure and non-zero charge state were found to be more active than their bulk-like and neutral counterparts [1–4].

In section 1.2 we considered essentially two approaches to manipulate the properties of metal deposits. Whereas their size and density can be tuned by introducing anchoring sites into the oxide surface, for example, defects [4] or hydroxyl groups, [5] their charge state is controlled by adjusting the metal-support interactions [6], as, for example, oxygen vacancies or structural electron traps. The second approach discussed relies on the fact that on ultrathin oxide films, even spontaneous charging can take place as

---

The results of this chapter have been reported in the following publication: X. Shao, S. Prada, L. Giordano, G. Pacchioni, N. Nilius and H.-J. Freund, “Shape control of metal ad-particles via doping of the oxide support: An STM and DFT study”,*Angewandte Chemie Int. Ed.*, **50**, 11525 (2011).

electrons tunnel from the substrate into the metal deposits. [7, 8]

In this chapter, based on a collaboration with the group of Prof. Freund at the Fritz-Haber-Institut in Berlin, we focus on a third possibility based on doping, since oxide doping might open new and versatile routes to tune particle-support interactions [9–11]. Whereas “overvalent” dopants produce excess electrons in the host oxide that can be transferred into suitable adsorbates, “undervalent” impurities promote the formation of holes in the oxide electronic structure that might be filled with electrons from the metal deposits. Such a charge transfer has direct consequences on the equilibrium shape of the ad-particles, as it enhances the metal oxide adhesion as well as the Coulomb forces within the confined metallic systems. [8, 12, 13] The presence of dopants also alters the formation energy of oxide defects that may act as nucleation centers and hence stabilize the dispersion of the active species. [14] In this chapter we investigate the influence of Mo dopants on the growth of Au particles on CaO(001) films, by STM and DFT. We demonstrate how tiny amounts of Mo embedded in a CaO matrix change the growth behavior of gold. Whereas 3D deposits are formed on the pristine oxide surface, strictly 2D growth prevails on the doped material. All the experimental data reported in this chapter have been provided by the group of Prof. Freund.

5.1 Experimental evidences

5.1.1 Experimental details

CaO films of 60 ML thickness were prepared by Ca deposition onto a sputtered and annealed Mo(001) single crystal in 5×10^{-7} mbar of oxygen. After annealing to 1000 K, an atomically flat and well ordered oxide film is obtained, as deduced from a sharp (1×1) square pattern in LEED and STM images. The doping is realized by codepositing small Mo amounts (2%) from a second evaporator during oxide growth. The topmost layers are always prepared without dopants to suppress Mo segregation to the surface.

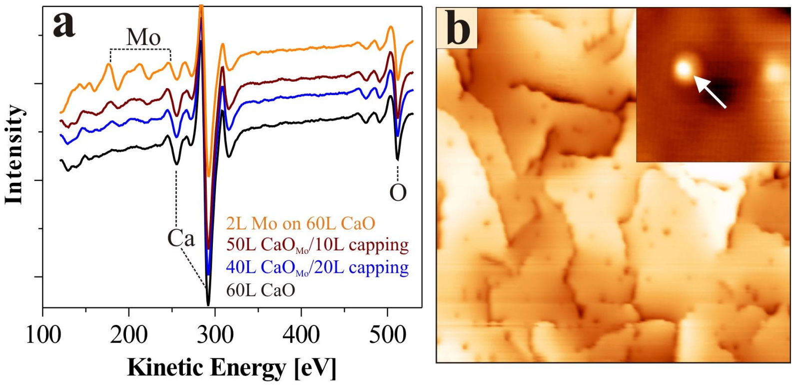

Figure 5.1: a) Auger spectra of pristine and Mo-doped CaO films covered with a thin Mo-free capping layer. The top curve has been taken after Mo deposition directly onto the surface. 1) 60 ML CaO + 2 ML Mo; 2) 50 ML CaOMo + 10 ML cap; 3) 40 ML CaOMo + 20 ML cap; 4) 60 ML CaO. b) STM image of a doped CaO film (100x100 nm^2). Inset: single Mo impurity, as observed in a film without capping layer (5×5 nm^2).

5.1.2 Results

The presence of Mo in the CaO matrix is confirmed with Auger spectroscopy (Figure 5.1a). Whereas only the Ca and O Auger transitions at 250, 290, and 512 eV are detected in the pristine oxide, Mo-specific peaks (around 200 eV) appear in doped films with a sufficiently thin capping layer. STM images of molybdenum-doped CaO films (Mo:CaO) display atomically flat and defect poor surfaces, covered with oxide terraces of 20 nm diameter, independent of the doping level (Figure 5.1b). The predominant defects are dislocation lines that originate from the coalescence of neighboring oxide islands and are involved in compensating the substrate-induced lattice strain. [15] For doped films with more than ten capping layers, no additional defects are revealed on the surface. Apparently, the caps are sufficiently thick to inhibit Mo segregation even during high-temperature treatments (up to 1000 K). When using thinner caps, atom-sized protrusions can be detected in the STM, which are assigned to individual Mo species (Figure 5.1b, inset).

Deposition of 0.7 ML Au at 300 K leads to the formation of metal par-

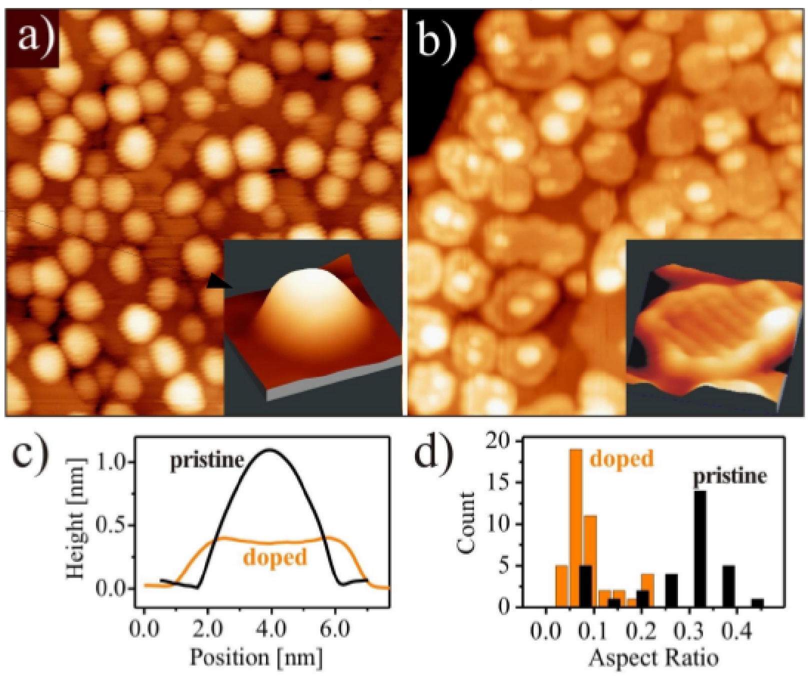

Figure 5.2: STM images of 0.7 ML Au on a) pristine and b) doped CaO films (50x50 nm^2). The insets display close-ups of two characteristic particles (10x10 nm^2) with the corresponding height profiles plotted in (c). d) Histogram of particle aspect ratios on doped and pristine films.

ticles. On pristine films, the deposits preferentially nucleate along the CaO dislocation lines and adopt pronounced 3D shapes (Figure 5.2a) with a height to diameter ratio of 0.30±0.10. The observed Volmer-Weber growth is characteristic for metals on wide-band-gap materials and reflects the small adhesion between ad-layer and inert oxide support. [16] In contrast, on the doped films, randomly distributed Au islands of monolayer height and aspect ratios of 0.07±0.02 develop (Figure 5.2b). These islands have hexagonal shapes, indicating growth along Au[111], and display a characteristic stripe pattern on their surface that is assigned to a Moiré structure formed between the square CaO and the hexagonal Au(111) lattice. The patterns occur with different orientations, indicating a rather loose Au-CaO interfacial registry. However, the mere appearance of monolayer islands suggests that the Mo impurities have a considerable impact on the Au-CaO adhesion.

5.2 Computational details

Spin-polarized DFT calculation has been performed with the VASP code (see 2.3). PBE and hybrid HSE functionals with 25% non-local exchange were used for calculating the total energies and the positions of Mo 4d levels inside the CaO band gap, respectively. Whereas bulk CaO was modeled with a (2 × 2 × 2) unit cell, a five-layer thick CaO(001) slab with a (3 × 3) surface cell and an Au atom adsorbed on one side was used for the adsorption studies; a dipole correction has been applied. The Brillouin zone was sampled with a (2 × 2 × 1) k-points mesh.

5.3 Results

To shed light on the role of the dopants, we have performed DFT calculations on a five-layer CaO(001) slab with one Mo ion substituting a Ca^{2+} species (2% Mo content). The calculations were carried out at the PBE level, but have been confirmed with test runs using hybrid HSE functionals. Without dopants, the Au adsorbs with 1.35 eV on top of a surface oxygen ion (Figure 5.3). The binding strength nearly triples in presence of a Mo species, even if the dopant is located well below the surface. Clearly, the Au-Mo interaction is preserved over large distances and independent of direct orbital overlap. Furthermore, the preference for binding to a surface oxygen atom is lost and cationic, anionic, and hollow sites become equally preferred sites for Au adsorption on the doped CaO films. For charge-neutrality reasons, in the undefective material, the substituting Mo should adopt the 2+ charge state of a rocksalt cation, which implies the Mo center must donate its 5s electrons to the neighboring ions, but retains the four electrons in the Mo 4d shell. This scenario is confirmed with HSE calculations for a single Mo in a bulk CaO environment, which find the low-spin $(t_{2g})^4(e_g)^0$ configuration as ground state and the high-spin $(t_{2g})^3(eg)^1$ state at 0.5 eV higher energy (the high-spin configuration becomes favorable for Mo ions in the CaO surface). Also with PBE, the $(t_{2g})^4(e_g)^0$ configuration remains energetically favorable. STM conductance spectra taken on 8 ML thick doped films confirm the existence of localized states in the gap region. Their assignment to

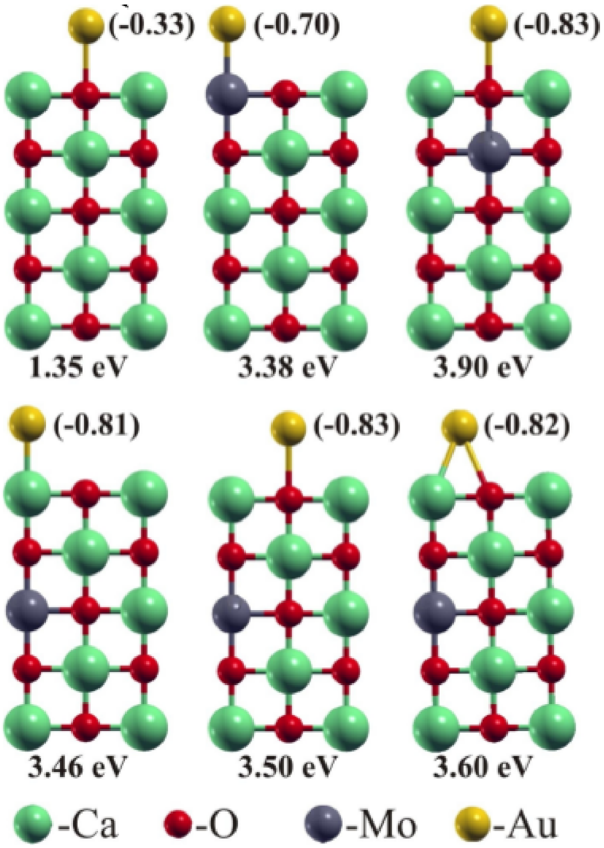

Figure 5.3: PBE binding energies and Bader charges (in parenthesis) for Au adsorbed on CaO(001) with a Mo impurity in various positions

specific Mo 4d-levels is hampered by the proximity of the metal substrate that is neglected in the calculations (Figure 5.4b). However, no conductance data could be acquired on thicker films because of the vanishing tunneling probability of electrons through the CaO gap region.

The PBE calculations suggest the Mo^{2+} charge state to be instable against electron transfer, either into CaO defect states, [17, 18] or into ad-species with acceptor character. Whereas electron trapping in the oxide film could not be confirmed, a charge transfer into the Au deposits is fully compatible with both the theoretical and experimental results. On pristine CaO, the Au atoms are neutral, as deduced from their half-filled 6*s* level,

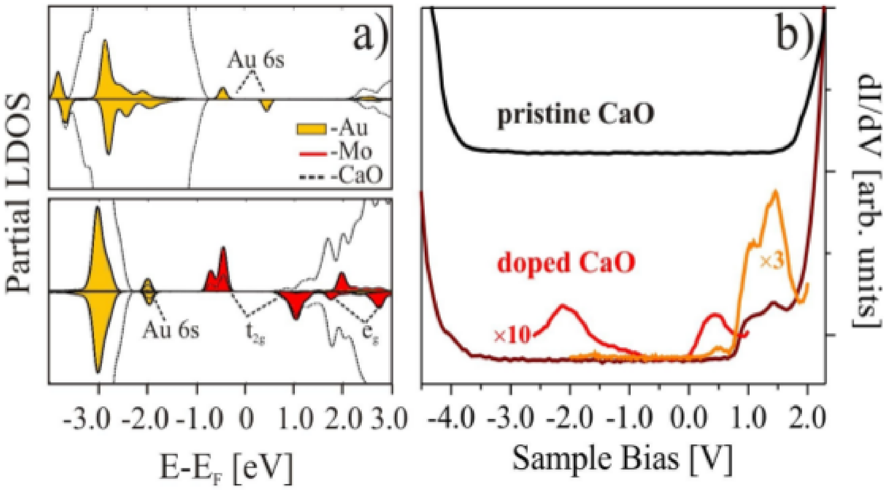

Figure 5.4: a) PBE projected density-of-states (DOS) calculated for nondoped (top) and doped (bottom) CaO films in presence of an Au adatom. b) STM conductance spectra taken on pristine and doped films of 8 ML thickness without gold. Several CaO gap states are discernable in the doped case.

and bind to the surface mainly through O2*p*-Au5*d* hybridization (Figure 5.4a). Upon doping, the Au 6*s* orbital shifts below the Fermi level and becomes doubly occupied, through a charge transfer from the Mo 4*d* state. This leads to an increased Bader charge and a vanishing magnetization of the bound gold atoms (Figures 5.3 and 5.4a). Concomitantly, the oxidation of the Mo dopant is detected, as the occupancy of the Mo 4*d* levels changes to $(t_{2g})^3(e_g)^0$ and the Mo charge state rises to 3+. The electron transfer enables strong electrostatic interactions between the Au^- and the CaO surface, boosted by a polaronic lattice distortion. [7,19] Thanks to this charge-mediated bond reinforcement triggered by the Mo, the gold tends to maximize its contact area with the CaO and forms 2D islands. A similar effect was earlier found for Au clusters on ultrathin oxide films, [12,13] (see 1.2) although the charging was initiated by electron tunneling from the metal substrate in that case. Also in the present example, the extra electrons most likely tunnel from the Mo dopants into the ad-metal, explaining why the 2D island shape prevails even in presence of a thin Mo-free capping layer.

5.4 Conclusions

In summary, the Mo-doping of CaO films changes the equilibrium shape of Au deposits from 3D to 2D. This crossover is initiated by a charge transfer from a high-lying Mo 4*d* level into the Au 6*s* affinity states, which makes the Au deposits negatively charged. The doping is highly efficient, as its signature remains detectable for Mo contents below 1%. We suspect that similar effects are present in many industrial catalysts that always contain finite concentrations of impurity ions. In fact, some of the raft-shaped metal particles that are suggested to be particularly active in catalysis might result from an unintentional doping during catalyst preparation. [3]

Bibliography

[1] a) M. Haruta, T. Kobayashi, H. Sano and N. Yamada, *Chem. Lett.* **16**, 405 (1987); b) M. Haruta, *CATTECH* **6**, 102 (2002).

[2] M. Valden, X. Lai, D. W. Goodman, *Science* **281**, 1647 (1998).

[3] a) A. S. K. Hashmi and G. J. Hutchings, *Angew. Chem.* **118**, 8064 (2006); *Angew. Chem. Int. Ed.* **45**, 7896 (2006); b) A. A. Herzing, C. J. Kiely,A. F. Albert, P. Landon and G. J. Hutchings, *Science 321*, 1331 (2008).

[4] T. Risse, S. Shaikhutdinov, N. Nilius, M. Sterrer and H.-J. Freund, *Acc. Chem. Res.* **41**, 949 (2008).

[5] M. A. Brown, Y. Fujimori, F. Ringleb, X. Shao, F. Stavale, N. Nilius, M. Sterrer and H.-J. Freund, *J. Am. Chem. Soc.* **133**, 10668 (2011).

[6] U. Landman, B. Yoon, C. Zhang, U. Heiz and M. Arenz, *Top. Catal.* **44**, 145 (2007).

[7] G. Pacchioni, L. Giordano and M. Baistrocchi, *Phys. Rev. Lett.* **94**, 226104 (2005).

[8] N. Nilius, M. V. Ganduglia-Pirovano, V. Brázdová, M. Kulawik, J. Sauer and H.-J. Freund, *Phys. Rev. Lett.* **100**, 096802 (2008).

[9] G. Pacchioni, *J. Chem. Phys.* **128**, 182505 (2008).

[10] V. Shapovalov and H. Metiu, *J. Catal.* **245**, 205 (2007).

[11] N. Mammen, S. Narasimhan, S. de Gironcoli, J. Am. Chem. Soc. 2011, 133, 2801.

[12] D. Ricci, A. Bongiorno, G. Pacchioni and U. Landman, *Phys. Rev. Lett.* **97**, 036106 (2006).

[13] M. Sterrer, T. Risse, M. Heyde, H.-P. Rust, H.-J. Freund, *Phys. Rev. Lett.* **98**, 206103 (2007).

[14] a) H. Y. Kim, H. M. Lee, R. Ganesh, S. Pala, V. Shapovalov and H. Metiu, *J. Phys. Chem. C* **112**, 12398 (2008); b) R. Ganesh, S. Pala and H. Metiu, *J. Phys. Chem. C* **111**, 12715 (2007).

[15] X. Shao, P. Myrach, N. Nilius and H. J. Freund, *J. Phys. Chem. C* **115**, 8784 (2011).

[16] a) M. Bäumer and H.-J. Freund, *Prog. Surf. Sci.* **61**, 127 (1999); b) X. Lai, T. P. St Clair, M. Valden and D.W. Goodman, *Prog. Surf. Sci.* **59**, 25 (1998).

[17] K. P. McKenna and A. L. Shluger, *Nat. Mater.* **7**, 859 (2008).

[18] H. M. Benia, P. Myrach, A. Gonchar, T. Risse, N. Nilius and H.-J. Freund, *Phys. Rev. B* **81**, 241415 (2010).

[19] U. Martinez, L. Giordano and G. Pacchioni, *ChemPhysChem* **11**, 412 (2010).

Chapter 6

Donor characteristics of Cr-doped MgO and Mo-doped CaO

In the previous chapter we have shown that doping is as a versatile means for tailoring the equilibrium shape and the thermodynamic stability of metal particles on oxide supports, which are also decisive parameters in heterogeneous catalysts. Because of its compelling simplicity, a basic charge-transfer picture is often evoked to describe the role of impurity ions in a host lattice, although it often fails to capture the complexity of the real system. Especially in oxide materials, dozens of mechanisms that suppress or modify the anticipated electron exchange are at work. For example, hole states generated by undervalent cationic impurities are often annihilated by an equal amount of charged O vacancies (e.g., F^+ color centers) [1] or by adsorbing donor molecules (e.g., hydrogen). [2] Conversely, the excess electrons released by overvalent dopants may be captured by structural inhomogeneities in the oxide lattice (e.g., by grain boundaries). [3] In addition, whether the desired charge transfer takes place depends on the energy position of the donor (acceptor) level with respect to the affinity state of the adsorbate. Reliable

---

The results of this chapter have been reported in the following publications: F. Stavale, X. Shao, N. Nilius, H.-J. Freund, S. Prada, L. Giordano, G. Pacchioni, “Donor Characteristics of Transition-Metal-Doped Oxides: Cr-Doped MgO versus Mo-Doped CaO” *J. Am. Chem. Soc.* **134**, 11380 (2012); S. Prada, L. Giordano, G. Pacchioni, “Charging of Gold Atoms on Doped MgO and CaO: Identifying the Key Parameters by DFT Calculations” *J. Phys. Chem. C* **117**, 9943 (2013).

prediction of the dopant's ability to act as an electron donor or acceptor in a given host oxide therefore requires a careful analysis of every single case. In this chapter, in a collaboration with the group of Prof. Freund at the Fritz-Haber-Institut in Berlin, we present two model systems for doped oxide materials that have isostructural and isoelectronic properties and still behave entirely differently with respect to gold particles adsorption. The two group 6 metals Cr and Mo were used as dopants, as they exhibit similar electronic structures [$ns^1(n - 1)d^5$] and ionization energies. They were inserted into the two rock salt oxides MgO and CaO, respectively, both of which are wide-gap insulators with band gaps of $>$7.0 eV. The experimental results reported in this chapter have been provided by the group of Prof. Freund.

6.1 Experimental evidences

6.1.1 Experimental details

The doped oxide systems were prepared as thin films via Mg (Ca) deposition onto sputtered and annealed Mo(001) single crystals in oxygen at a pressure of 5×10^{-7} mbar. [4, 5] The dopants were introduced by adding 1 atom % Cr (Mo) to the gas vapor used for the oxide growth. The film thickness was adjusted to 20 (60) monolayers (ML) for Cr:MgO (Mo:CaO) to suppress interface effects induced by the Mo(001) support. These values correspond to the maximum thicknesses that can still be probed with scanning tunneling microscopy (STM), a technique that relies on a finite conductivity of the oxide films. Surface segregation of the dopants was suppressed by growing five pristine oxide layers on top of the doped films. After annealing to 1000 K, a sharp (1 × 1) square pattern corresponding to a rock salt (001) surface was observed by low-energy electron diffraction (LEED), while STM images of the films revealed large, atomically flat terraces separated by mainly [100]-oriented dislocation lines (Figure 6.1). Although no dopant signature was detected by STM and LEED, their presence could be verified by means of Auger spectroscopy and, for Cr:MgO, cathodoluminescence spectroscopy. [6]

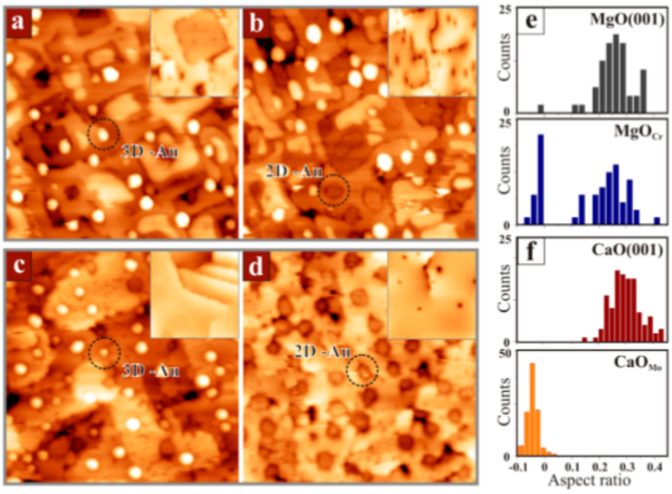

Figure 6.1: (a, b) STM topographic images of (a) bare and (b) Cr-doped MgO(001) films with a thickness of 20 ML after dosing of 0.5 ML Au (60 nm x 50 nm, 5.5 V). The insets display the respective surfaces before Au deposition (20 nm x 20 nm). (c, d) Similar measurements on (c) bare and (d) Mo-doped CaO(001) with a thickness of 60 ML (60 nm x 60 nm, 6.0 V). The 2D Au islands appear as faint depressions on both surfaces, because electron transport from the STM tip into the surface is inhibited by upshifted field-emission resonances above the Au islands. (e, f) Histograms of the particle aspect ratios (height/diameter) measured on the pristine and doped oxide films. The negative apparent height of the 2D gold in the images gives rise to negative aspect ratios in the histogram.

6.1.2 Results

Charge transfer processes involving the TM dopants were identified by depositing 0.5 ML Au on top of the Mo:CaO and Cr:MgO films at room temperature. The equilibrium geometry of Au particles is known to be sensitive to their charge state. Whereas neutral particles adopt compact three-dimensional (3D) shapes because of the small energy gain from interfacial interactions with the oxide support, two-dimensional (2D) islands form in the presence of excess electrons in the gold. This crossover in particle geometry is driven by effective electrostatic and polaronic interactions between Au^- and the oxide lattice and results in a spreading of the metal on the oxide support (see 1.2). Indeed, the equilibrium shape of the Au deposits was found to change upon doping of the MgO and CaO films (Figure 6.1). While Au grew into 3D deposits on the pristine oxides, monolayer islands developed on Mo:CaO films. Surprisingly, no geometry crossover was observed for Cr:MgO, where the vast majority of particles retained a 3D configuration and only few aggregates adopted a 2D shape. The difference became evident in shape histograms obtained by plotting the aspect ratios (height/diameter) of ∼500 Au particles observed on the different substrates (Figure 6.1e,f). The dimensionality change affected 100% of the Au particles on Mo:CaO but was limited to a small number of deposits on Cr:MgO. Apparently, only Mo dopants are able to donate electrons into the admetal, while Cr is electrically inactive. In view of the similar electronic properties of the two TM ions, the question arises why Mo is a better dopant than Cr. To elucidate the difference between the two doped oxides, in the next section we systematically analyze their electronic structures and the binding properties of gold.

6.2 Computational details

Periodic DFT calculations were performed with a plane wave basis set (400 eV energy cutoff) and the projector-augmented wave (PAW) method, as implemented in the VASP code. (see section 2.3) The stability of bulk impurities in different oxidation states was investigated with a (3 × 3 × 3) bulk supercell and (2 × 2 × 2) Monkhorst-Pack k-points mesh. For the description of the electronic properties of isolated substitutional TM a (2 × 2 × 2) supercell was used, and the Brillouin zone was sampled with a (3 × 3 × 3) Monkhorst-Pack mesh. For Au adsorption, a (3 × 3) surface supercell of a five-layer thick oxide slab was employed, where one impurity atom replaced one oxide cation. Au was adsorbed on one side of the slab. A dipole correction was included in order to eliminate the interaction among repeated slabs, separated by more than 10 Å. All atomic positions were optimized until atomic forces were less than 0.01 eV/Å. In the case of slab calculations, the atoms of the oxide bottom layer were kept fixed. Magnetic moments of impurities have been evaluated from the projection of the spin density into atomic spheres, while atomic charges have been estimated using the Bader decomposition scheme. [8]

Impurities with formal oxidation state larger than +2 (e.g., Cr^{3+} or

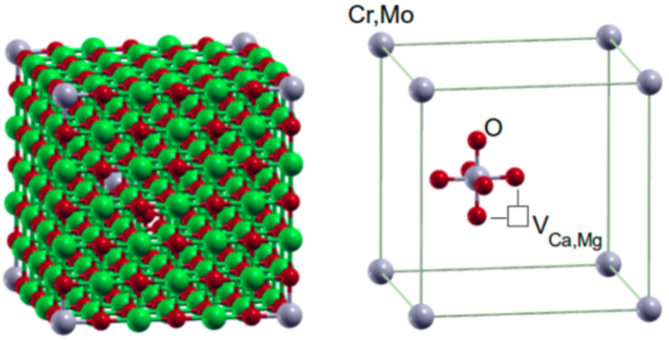

Figure 6.2: Position of the impurity atoms (Cr, Mo) and cationic vacancy for the MgO or CaO supercell used in the calculations in ball and stick representation (left) and schematic view (right). Red, O; green, Mg or Ca; gray, Cr or Mo.

Mo^{3+}) replacing the Mg^{2+} or Ca^{2+} lattice ions introduce a charge imbalance. This has been treated in two ways. In the first approach, the TM^{n+} charge is balanced by introducing compensating defects, such as cationic vacancies or substitutional low valence cations (e.g., Li), so that the entire system is charge neutral. This approach has been employed for bulk calculations. In particular, in order to evaluate the thermodynamic stability of impurity ions in different charge states, we used cationic vacancies as compensating species, while Li impurities have been introduced when analyzing the electronic properties of Cr^{3+} and Mo^{3+}. In a second approach, we considered the isolated impurity, and we used a uniform background of charge to compensate for the higher oxidation state of the TM ion. [9] This latter approach has been used in the study of Au adsorption. The results show that the conclusions are not dependent on the approach followed.

For the treatment of the exchange-correlation functional, we used different methods. The thermodynamic stability of TM impurities in various charge states as a function of the preparation conditions has been studied with the pure DFT PBE functional, also used in chapter 5. The electronic structure, and in particular, the density of states (DOS), Kohn-Sham energy gaps, and defect levels, have been obtained also using self-interaction corrected functionals. One specific example, that of Cr^{3+}:MgO, has been discussed using two different hybrid functionals, PBE0 and HSE06 (see 2.4.3). Furthermore, for this system, the DFT+U approach (see 2.4.2) has been also considered (in the Dudarev's formulation [10]), where the Hubbard term is added on the localized Cr 3d states, and the results have been analyzed as a function of the U parameter. The study of Au adsorption on Cr:MgO and Mo:CaO have been done at both the PBE and PBE0 levels of theory. The optimized lattice constant of pure bulk oxide at the different level of theory was used in the calculations (for MgO, 4.26 and 4.21 Å; for CaO, 4.83 and 4.81 Å at PBE and with hybrid functionals, respectively).

6.3 Results

6.3.1 Characterization of TM-doped MgO and CaO

We start the discussion by considering Cr impurities in MgO (Cr:MgO) and Mo impurities in CaO (Mo:CaO). In section 6.3.3, we will also consider the effect of the matrix by exchanging the impurities and the host materials (Cr:CaO and Mo:MgO). When a transition metal atom of the sixth group enters in a nondefective alkaline-earth oxide as a substitutional impurity it assumes a formal +2 oxidation state, resulting in a d^4 electronic configuration. In an octahedral environment, this can result in high spin (HS) $t_{2g}^3 e_g^1$ or low spin (LS) $t_{2g}^4 e_g^0$ configurations. In the bulk of Cr-doped MgO, Cr^{2+} assumes a HS $t_{2g}^3 e_g^1$ configuration, which is 0.63 eV (PBE) or 0.75 eV (PBE0) more stable than the LS configuration. The lattice relaxation induced by the impurity is small and mainly restricted to the nearest neighbour oxygen atoms: the average Cr-O distance is 2.17 Å, to be compared to d(Mg-O) = 2.13 Å. This is because the dopant ionic radius, $r(Cr^{2+}) = 0.73$ Å, is very similar to that of Mg^{2+}, $r(Mg^{2+}) = 0.72$ Å. [11]

We turn now to the description of Mo-doped CaO. The heavier Mo^{2+} cation assumes in the bulk oxide a LS $t_{2g}^4 e_g^0$ electronic configuration, preferred by 0.80 eV (PBE) or 0.53 eV (PBE0) over the HS $t_{2g}^3 e_g^1$ state. In this case, the impurity produces a small contraction of the metal-oxygen distance, d(Mo-O) = 2.31 Å, 4% shorter than the Ca-O distance in pure CaO (2.40 Å).

These results refer to an ideal, undefective crystal. In the real systems, one has to take into account that TM ions can easily change oxidation state and that +2 is not the most common oxidation state of Cr and Mo. Clearly, if an impurity in a host oxide crystal assumes a different charge state, defect centers must appear in the material to maintain electroneutrality. For instance, if a Zr^{4+} ion in ZrO_2 is replaced by a Ca^{2+} cation, an oxygen vacancy must form to keep the charge balance. In the case of Cr:MgO and Mo:CaO, the tendency of both Cr and Mo is to assume higher oxidation states. This can be compensated by the formation of cation vacancies.

Experimentally, it has been reported that Cr enters MgO as Cr^{3+}, the extra positive charge being compensated by the formation of Mg vacancies, V_{Mg}. [12, 13] This has been supported, for instance, by optical and EPR spectroscopies, which also indicate that the Cr^{3+} and the V_{Mg} centers are adjacent. [14, 15] A Mg vacancy in pure MgO results in the removal of two electrons from the O 2p valence band. The two holes tend to localize near the vacancy, with formation of two O^- species (the two unpaired electrons give rise to a triplet ground state). [16, 17] In the presence of Cr dopants, the hole centers associated to a V_{Mg} defect are quenched due to an electron transfer from the Cr 3d states. In particular, one V_{Mg} center compensates the formation of two Cr^{3+} ions in the lattice.

A similar mechanism is expected also for Mo:CaO, although direct experimental evidence is lacking. This opens a general question about the relative stability of the possible combinations of V_M centers and TM^{n+} cations, with M = Mg, Ca, TM = Cr, Mo, and n = 2-5. To answer this question, we compared the stability of two impurity atoms in the bulk (3 x 3 x 3) supercell, by varying the number of cation vacancies. In this way, the system without vacancies corresponds to the TM^{2+} oxidation state, while the system with n_V cation vacancies creates two TM^{n+} ions with $n = 2 + n_V$. We have verified, by analyzing the PDOS on the TM ions (not shown), that the holes generated by the cation vacancies are really transferred to the TM impurity for all considered oxidation states (+3 and +4 for Cr and +3 to +5 for Mo). The two impurity atoms are located as far as possible in the supercell, while the vacancies are adjacent to the impurity ions in the case of TM^{3+} and TM^{4+}, Figure 6.2. In the case of Mo^{5+}, the third vacancy is placed far from the two Mo atoms. In any case, we have verified that the position of the vacancies does not alter the stability diagram described below.

We first computed the cation vacancy formation energies, $E_{form}(V_M)$, for pure and doped oxides. In the case of MgO, the removal of a Mg atom has an energy cost of 8.07 eV (computed with respect to bulk Mg). This cost drops to 0.97 eV in the presence of two Cr atoms, thanks to the electron transfer from the impurities to the defect. In the case of CaO, forming a

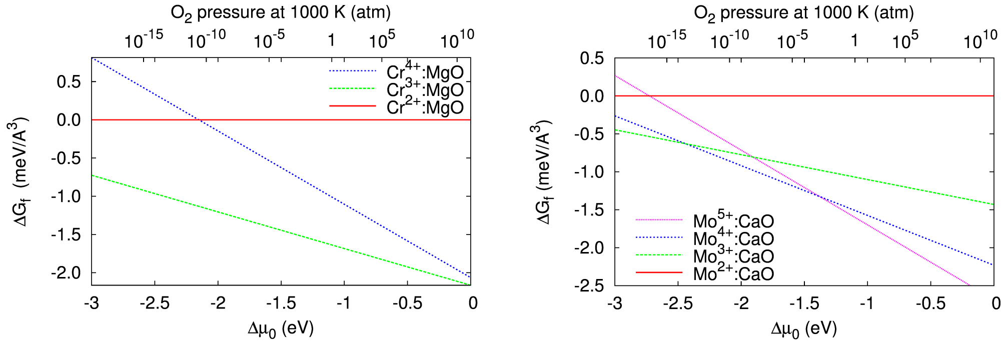

Figure 6.3: Change in Gibbs formation energy for the different TM^{n+} ions (with n = 2 + n$_V$, where n$_V$ is the number of cationic vacancies) structures as a function of the oxygen chemical potential: Cr:MgO (left) and Mo:CaO (right). The dependence on the oxygen partial pressure is also reported at T = 1000 K.

calcium vacancy costs 8.01 eV, but the value drops to 1.68 eV when two Mo substitutional ions are included in the supercell. The reason for the large change in formation energy is that one electron is transferred from the d states of each Cr or Mo ion to the low lying states of O$^-$ ions around V$_M$, with change of TM oxidation state from +2 to +3.

In order to determine the relative stability of the different defective structures, where the introduction of an increasing number of cation vacancies corresponds to an increase of the TM oxidation state, we have computed their Gibbs formation energy per unit of volume at pressure p and temperature T: [18]

$$G_f(T,p) = [G(T,p,\{n_x\}) - \sum_x n_x \mu_x(T,p)]/V \qquad (6.1)$$

where G is the Gibbs free energy of the solid with volume V; n_x, μ_x, and p_x are the number of particles in the solid, the chemical potential, and the partial pressure in the gas phase of the species x, respectively. We have assumed the following approximations: (1) metal vacancies are the only defects in the bulk structure that influence the oxidation state of the dopant, as described above; (2) all the entropic and vibrational contributions are neglected for the solid phase, and the Gibbs free energy is approximated with the total DFT energy (E); (3) during growth, metal (M), oxygen, and

MO oxide are at the thermodynamic equilibrium:

$$\mu_M + \mu_O = E_{MO} \tag{6.2}$$

Using the condition of equilibrium, we can calculate the Gibbs formation energy change with respect to the doped undefective oxide, ΔG_f, as the function of the oxygen chemical potential:

$$\Delta G_f = [G_{def} - G_{st} + n_V E_{MO} - n_V \Delta\mu_O(p,T)]/V \tag{6.3}$$

where G_{def} and G_{st} are the Gibbs free energies of the defective and stoichiometric systems, respectively, and n_V is the number of metal vacancies. The change in the O_2 chemical potential $\Delta\mu_O(p,T) = \mu_O - 1/2E(O_2)$ is referred to half of the total energy of an oxygen molecule and can be related to temperature T and oxygen partial pressure p.

The upper value for the oxygen chemical potential is determined by the condition in which oxygen molecules start to condensate $\Delta\mu_O = 0$; the lower limit is set where metal particles start to crystallize, $\mu_M = E_M$. Using the condition of equilibrium $E_{MO} - E_M < \Delta\mu_O$, we obtain the following ranges of validity: $-5.48 < \Delta\mu_0 < 0$ for MgO and $-6.10 < \Delta\mu_O < 0$ for CaO. The relative stability, computed at the PBE level, of the variously doped Cr:MgO and Mo:CaO oxides is reported in Figure 6.3. The results clearly indicate that in the entire range of oxygen chemical potential the preferential oxidation state of Cr in MgO is Cr^{3+}. This is also what is known experimentally. In the case of Mo:CaO, the Mo^{3+} state is favored in oxygen-poor conditions, while Mo^{4+} is preferred at intermediate values, and Mo^{5+} is stable in oxygen-rich conditions. In the experiments, the Mo:CaO films are prepared by reactive deposition and then annealed at T = 1000 K in an oxygen partial pressure of 5×10^{-7} mbar. Under these conditions, following our calculations, Mo^{3+} or Mo^{4+} ions are stable, suggesting that Mo in CaO can exist in higher oxidation states compared to Cr in MgO. We will see below that this a key aspect resulting in a different chemical reactivity of the two systems when Au atoms (and Au particles) are deposited on the surface of the two oxides.

From a structural point of view, the reduction of the TM size causes a progressive contraction of the TM-O distances with the increasing of the cation charge. In the case of Cr:MgO, this contraction ranges from 4% for Cr^{3+} to 7% for Cr^{4+} (the average d(Cr-O) being 2.05 and 1.99 Å). For

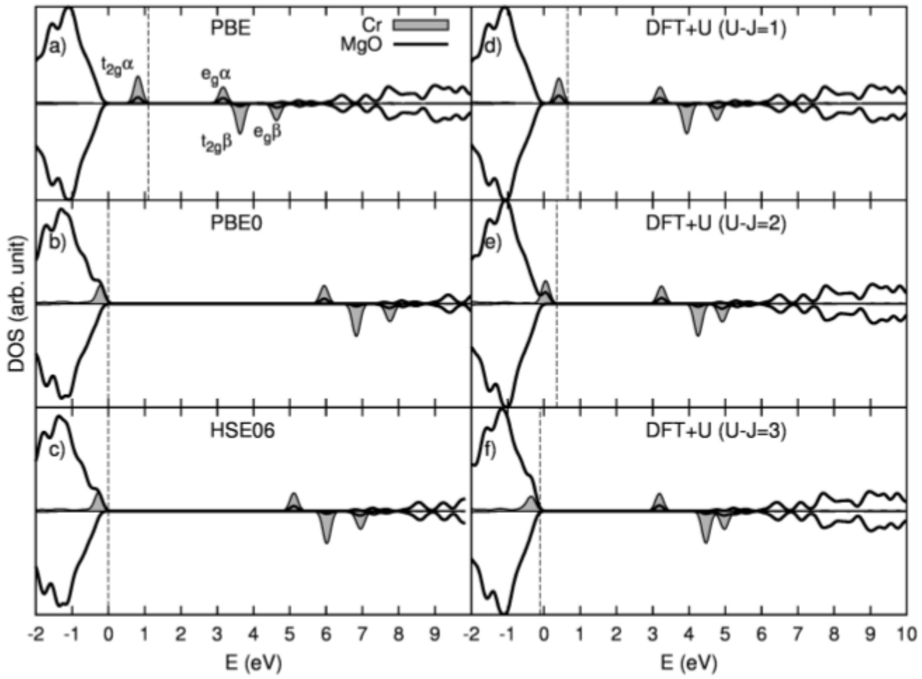

Figure 6.4: PDOS of a Cr^{3+} ion in substitutional position in bulk MgO as obtained with various methods. (a) PBE; (b) PBE0; (c) HSE06; (d) DFT +U, U - J = 1; (e) DFT+U, U - J = 2; (e) DFT+U, U - J = 3. The oxide valence band top edge is considered as zero energy reference; the vertical line indicates the highest occupied state.

Mo:CaO, the effect is more pronounced; Mo^{3+} induces a 7% contraction, which becomes 11% for Mo^{4+} and even 15% for Mo^{5+} (d(Mo-O) = 2.23, 2.14, and 2.05 Å, respectively).

6.3.2 Electronic structure of Cr^{3+}:MgO: methodological aspects

Having established the mechanisms of stabilization of TM impurities in various oxidation states and their relative stability, we consider now the electronic structure of the dopants. Of particular interest is the position of the t_{2g} and e_g states in the band gap of MgO and CaO as this is a key aspect in determining the tendency of the TM ions to act as electron donors with respect to adsorbed species. The discussion of the electronic structure of a TM ion embedded in an ionic crystal must take into account the well-known deficiency of standard DFT in predicting band gaps. [7] For this reason, we first considered a single example, Cr^{3+} in bulk MgO, using three conceptually different approaches: a standard GGA functional (PBE), two hybrid functionals (PBE0 and HSE06), and the DFT+U method where various U values have been compared. The +3 oxidation state has been obtained by substituting Mg^{2+} with a Li^{+} ion in the supercell, which remains neutral. In the absence of the TM impurity, Li creates a hole in the O $2p$ band, which is filled by an electron of the TM ion in the doped oxide. The PDOS curves for Cr^{3+}:MgO obtained with the various approaches are reported in Figure 6.4. We discuss the position of the Cr $3d$ states with respect to the top of the valence band (VB) and the bottom of the conduction band (CB) as provided by the Kohn-Sham energy levels. It should be mentioned that these values are not directly comparable to observable quantities like optical, photoemission, or scanning tunneling spectra due to many-body effects not included in the Kohn-Sham energy levels. Still, the results provide an indication of the different description of the TM ions as a function of the inclusion of self-interaction correction.

We start from the PBE results. With this approach, the MgO band gap, 4.5 eV, is severely underestimated with respect to the experiment (7.8 eV). [19] The t_{2g}^3 states are found at about 1 eV above the top of the VB, while the empty components of the t_{2g} and the e_g states are close to the CB, Figure 6.4a. Thus, the Cr occupied $3d$ states are inside the band gap of the insulating oxide. At the PBE0 level, the picture changes. The MgO gap increases to 7.2 eV, only slightly smaller than the experimental one. The inclusion of a portion of exact exchange splits the filled and empty components of the $3d$ levels so that the t_{2g}^3 states are now at the top of the VB and not above it, Figure 6.4b,c. The shift of the empty $3d$ levels toward higher energies is of a similar amount of the shift of the CB minimum, so that their relative position changes slightly. A virtually identical picture is obtained at the PBE0 and HSE06 level, Figure 6.4b,c. Clearly, introducing the self-interaction correction stabilizes the occupied d states and destabilizes the unoccupied ones as a result of the stronger spin localization. This effect has been verified using the DFT+U approach in connection with the PBE functional, Figure 6.4d-f. The effective U value has been varied in order to increase the level of electron localization. The effect is very clear. For U - J = 1, the picture is close to that obtained at the PBE level: the t_{2g}^3 states are at about 0.5 eV above the top of the VB, while the empty $3d$ states are close to the bottom of the CB. With U - J = 2, the t_{2g}^3 states are just above the O $2p$ valence band but still in the gap. For U - J = 3, the t_{2g}^3 are at the top of the VB, and the picture resembles that obtained with hybrid functionals. In all cases, the empty t_{2g} components and the e_g states are close to or in the CB. Notice that the band gap of MgO at the DFT+U level is not modified as the U term is added only to the localized Cr $3d$ orbitals. However, the $t_{2g} - e_g$ splitting is not as pronounced as with hybrid functionals, and the position of the empty Cr $3d$ states is not very different from that of the other calculations.

This discussion shows that, not surprisingly, the position of the MgO band gap edges and the Cr $3d$ levels depends on the level of treatment. How this will impact the discussion on the charge transfer from doping species to adsorbed species will be discussed in the next sections. Here, we limit ourselves to the observation that the position of the $3d$ Kohn-Sham energy levels with respect to the MgO gap changes, in particular for the occupied states. A detailed analysis of the implications of these differences on observable quantities, like $d-d$ transitions to simulate optical spectra or ionization energies to be compared with photoemission experiments, is required in order to assess which method better describes this system and goes beyond the scope of this work. Many-body theories or time-dependent DFT calculations would be necessary in order to elucidate this point. These approaches give access to excited states and to spectral signatures, such as $d-d$ transitions, which cannot be extracted from the d-d orbital separations obtained with the one-electron approaches used in this work. In the following, we discuss the electronic structure of Cr and Mo dopants in MgO and CaO using the PBE0 hybrid functional and its effect on the redox properties of the system.

6.3.3 Electronic structure of TM-doped MgO and CaO and matrix effects

The PDOS curves of Cr and Mo impurities in +2 and +3 oxidation states obtained at the PBE0 level are reported in Figure 6.5. Also in this case, the +3 oxidation state has been obtained by substituting Mg^{2+} or Ca^{2+} with a Li^+ ion in the supercell. The effect of the different oxide matrix has been

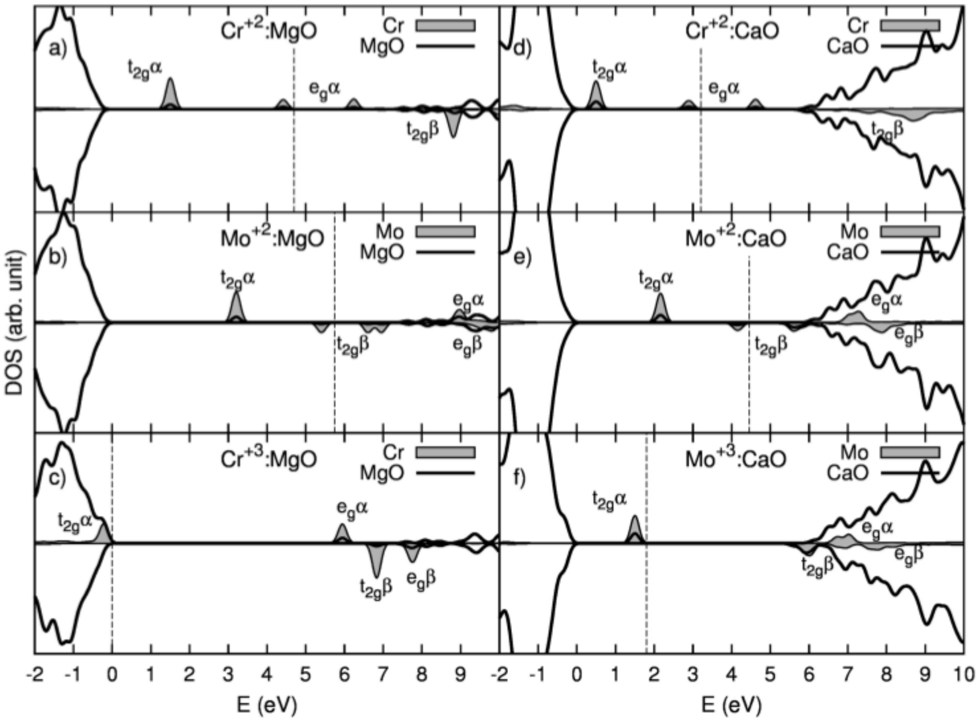

Figure 6.5: Projected density of states (PDOS) for Cr and Mo in MgO (left) and CaO (right), in different oxidation states, obtained at PBE0 level. (a) Cr^{2+}:MgO; (b) Mo^{2+}:MgO; (c) Cr^{3+}:MgO; (d) Cr^{2+}:CaO; (e) Mo^{2+}:CaO; (f) Mo^{3+}:CaO. The oxide valence band top edge is considered as zero energy reference; the vertical line indicates the highest occupied state.

analyzed by comparing Cr^{3+} and Mo^{3+} impurities in MgO and CaO.

The Cr-projected DOS of Cr^{2+}:MgO, Figure 6.5a, shows a small degree of hybridization between the dopant orbitals and the oxide valence band, in the energy region between -8 and -6 eV. The Cr 3d electrons remain localized on the impurity and create new states in the oxide band gap (see above). The system undergoes a small Jahn-Teller distortion, which removes the degeneracy of the O_h space group, but for the sake of simplicity, we continue to use the $t_{2g} - e_g$ notation. The t_{2g} levels, occupied by three electrons, are located about 2 eV above the top of the VB, while the singly occupied e_g level is nearly 3 eV higher in energy.

Next we consider a Mo^{2+} ion in the MgO matrix, Figure 6.5b. The Mo $4d$ levels are higher in the band gap compared to Cr (in particular, the filled t_{2g} levels are nearly 1 eV higher in energy). We note that, for both dopants, the highest empty d levels fall at the bottom of the CB and are partly hybridized with it, an effect more pronounced at the PBE level (not shown). The case of Cr^{3+}:MgO, Figure 6.5c, has already been discussed in the previous section. We want to notice here that, compared to the Cr^{2+}:MgO case, the higher positive charge on the dopant strongly stabilizes the filled t_{2g} level, resulting in a $t_{2g} - e_g$ splitting of 6.1 eV (it is about 2.9 eV in Cr^{2+}:MgO).

We turn now to the dopants in the CaO matrix. For both Cr^{2+}:CaO and Mo^{2+}:CaO, Figure 6.5d,e, we can see that the relative position of TM d levels is almost the same as in MgO. However, the filled d states are closer to the VB edge, as the gap is smaller in CaO. In particular, the filled t_{2g} and e_g levels are about 0.5 and 2 eV, respectively, above the CaO valence band. At higher energies, the lower CB edge in CaO causes a larger mixing between the dopants and the oxide states, as the empty d states fall in the conduction band.

Finally, we discuss the electronic structure of Mo^{3+}:CaO, Figure 6.5f. In this case, the stabilization of the filled t_{2g} level is much less pronounced than that in Cr^{3+}:MgO, and these states are stabilized by 0.8 eV only. The different position of the Cr^{3+} and Mo^{3+} d states is at the origin of their different donor ability, as shown in the next section. The t_{2g} minority spin component is found just below the CB edge, while the e_g states fall in the conduction band.

Before considering the adsorption properties, we analyze how the properties of TM-impurities located in the surface and subsurface regions change compared to bulk impurities. The impurity has thus been placed in different positions in a five layer thick slab. In Cr^{2+}:MgO and Cr^{3+}:MgO the properties are marginally affected by the presence of the surface. In particular, in Cr^{2+}:MgO, the high spin configuration, with four unpaired electrons, remains always preferred. Conversely, in Mo^{2+}:CaO, when Mo is in the surface layer the HS $e^2 b_2^1 a_1^1 b_1^0$ configuration becomes stable due to the symmetry breaking induced by the surface (the symmetry changes from O_h (bulk) to C_{4v} when the impurity is in the surface layer). When Mo is in a subsurface layer (second or third layer from the surface) due to the reduction of the CaO band gap at the oxide surface, the Mo highest occupied d state becomes partly delocalized over the CaO surface (see chapter 7). This effect

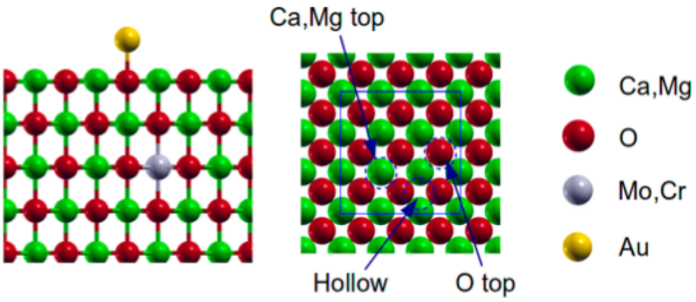

Figure 6.6: Schematic representation of a Au adatom adsorbed on the oxide surface in the presence of an impurity atom in the third oxide layer from the surface. Left, side view; right, top view.

is independent of the functional used since at PBE0 level the Mo $d-d$ separation and the CaO band gap are both increased more or less by the same amount, compared to PBE results.

6.3.4 Au adsorption on TM-doped MgO and CaO surfaces

The influence of doping on the adsorption properties of the oxide has been addressed by considering gold adatoms as representative of electronegative adsorbates. The impurity TM atom has been placed in the third oxide layer, thus avoiding any direct dopant-adsorbate interaction, Figure 6.6. This choice is driven by the objective to mimic the experiments, where the direct bonding between adsorbed gold and TM dopants is hindered by the deposition of a thin capping layer of pure oxide on the doped material. In chapter 5, we have considered several positions for the Mo^{2+} impurity atom, and we found that the adsorption on-top of an oxygen ion with the Mo impurity just below it (subsurface impurity) is the most stable configuration. This is followed by a configuration with Mo^{2+} in the third layer, the case considered here, while direct bonding between Mo and Au was found to be less favorable. Here, we consider systematically gold adsorption in the doped oxide described in the previous sections, with both PBE and PBE0 functionals. Oxidation states of the TM dopant higher than +2 have been treated by using a uniform background of charge.

		$E_{ads}(Au), eV$		$q(Au), \|e\|$	
	adsorption site	PBE	PBE0	PBE	PBE0
MgO	O-top	1.03	0.63	-0.30	-0.22
CaO	O-top	1.35	1.14	-0.33	-0.32
Cr^{2+}:MgO	hollow	2.97	2.36	-0.81	-0.83
Cr^{3+}:MgO	O-top	0.97	0.53	-0.25	-0.17
Mo^{2+}:CaO	hollow	3.60	3.04	-0.80	-0.84
Mo^{3+}:CaO	hollow	2.10	1.23	-0.79	-0.81
Mo^{4+}:CaO	hollow	1.72	-	-0.75	-
Mo^{3+}:MgO	hollow	1.20	-	-0.71	-
Cr^{3+}:CaO	O-top	1.47	-	-0.30	-

Table 6.1: Adsorption properties of Au adatoms adsorbed on pristine and doped MgO and CaO Surfaces: preferred adsorption site, adsorption energy with respect to gas phase Au (E_{ads}), Au Bader charge (q). The impurity atom (Cr or Mo) is placed in the third layer of the slab. The results are obtained with the PBE and PBE0 functionals.

The adsorption properties of Au adatoms on the pristine and doped oxides are reported in Table 6.1. By comparing Au adsorption on MgO and Cr^{2+}:MgO, one can observe profound differences. First of all, the preferred adsorption site changes from O-top to hollow. Moreover, on Cr:MgO the magnetic moment on Au is quenched, and the Bader charge indicates that Au has gained one extra-electron, becoming Au^-. This is clearly visible in the PDOS (PBE0), Figure 6.7a, showing that the Au 6s state is doubly occupied. As a result of the charge transfer, the Au gold states are pushed above the top of the MgO VB. The analysis of the Cr states reveals that the electron is transferred from the impurity, which assumes a $t_{2g}^3 e_g^0$ electronic configuration after the charge transfer (Cr^{3+}). The charge transfer strongly reinforces the bond of Au with the surface, and the resulting binding energy, 2.97 eV (PBE), is three times larger than on pure MgO, 1.03 eV (PBE). The effect is present also with the hybrid PBE0 functional, Figure 6.7a. The main difference is that the absolute value of the adsorption energy of Au on Cr^{2+}:MgO, 2.36 eV, is somewhat smaller than at the PBE level, but still much larger than on pure MgO, 0.63 eV, Table 6.1.

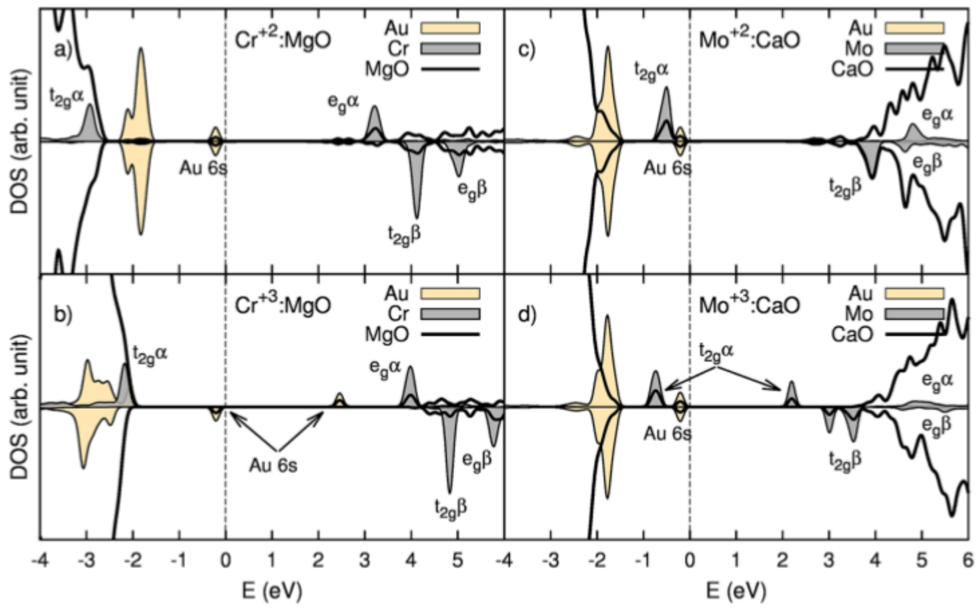

Figure 6.7: Projected density of states (PDOS) for Au adatoms on Cr:MgO (left) and Mo:CaO (right), obtained at the PBE0 level. Top, TM ion in +2 oxidation state; bottom, TM ion in +3 oxidation state. The vertical line indicates the highest occupied state. The results refer to the Au atom in the ground state geometry (Table 6.1).

Au adsorption on Mo^{2+}:CaO causes an analogous charge transfer from the impurity to the adsorbate, as indicated by the Au Bader charge (Table 6.1) and the Au $6s^2$ electronic configuration, see the PDOS in Figure 6.7b. The energy gain induced by the charge transfer is even more pronounced in this case (3.60 eV on doped CaO versus 1.35 eV on pure CaO at the PBE level), in agreement with the higher position of the Mo^{2+} states in the gap with respect to the Cr^{2+} ones. Also here, we found that the absolute Au binding energies are smaller at the PBE0 level, 3.04 eV for Mo^{2+}:CaO versus 1.14 eV for pure CaO, Table 6.1, but the trend is exactly the same.

In the previous section, we have shown that Cr^{2+} is not stable and that chromium enters in MgO as Cr^{3+}. The question becomes whether this species is also able to donate electrons to the electronegative gold adsorbate. The results, Table 6.1, indicate that the adsorption properties of Au adsorption on pristine MgO and Cr^{3+}:MgO are very similar: the O-top site is preferred, and gold is formally neutral and spin polarized ($6s^1$ atomic configuration), as clearly shown in the PDOS, Figure 6.7c. Also the Au adsorption energy is almost the same (PBE, MgO 1.03 eV, Cr^{3+}:MgO 0.97 eV; PBE0, MgO 0.63 eV, Cr^{3+}:MgO 0.53 eV). Thus, under usual experimental conditions no charge transfer to gold is expected for Cr:MgO. This is in agreement with the experimental findings, which showed a preferential three-dimensional growth of nanoparticles on this substrate, typical of neutral Au. This result is obtained at both PBE and PBE0 levels of theory.

Contrary to the Cr-doping case, Mo is able to donate charge to gold also when in an oxidation state larger than +2. In Figure 6.7d, the Au PDOS for adsorption on Mo^{3+}:CaO indicate that the Au $6s$ state is doubly occupied, while Mo oxidizes to Mo^{4+} and assumes a $t_{2g}^2 e_g^0$ electronic configuration. The energy gain related to the charge transfer is 2.10 (PBE) and 1.23 eV (PBE0) for Au on Mo^{3+}:CaO compared to 3.60 (PBE) and 3.04 eV (PBE0) for Au on Mo^{2+}:CaO, Table 6.1. This reflects the different position of the Mo $4d$ levels for the two oxidation states, Figure 6.5. Thus, also the different behavior of Cr^{3+} and Mo^{3+} impurities is confirmed at the PBE0 level, showing that while the absolute values of the interaction energies depend on the functional used, the general physical features are not. Charging of gold is also possible for Mo^{4+}:CaO, although in this case the charge transfer to Au is not complete and the energy gain is smaller (the Au adsorption energy is 1.72 eV (PBE), only slightly larger than neutral gold on pure CaO). We note that in the PDOS reported here, computed at the PBE0 level, the filled Mo t_{2g} states fall below the doubly occupied Au $6s$ state, whereas their positions are inverted at the PBE level (see chapter 5), due to the stabilization of the localized d states when including a fraction of Hartee-Fock exchange.

The electrostatic attraction between the charge species resulting from the charge transfer contributes to the increase in the Au adsorption energy. This follows the expected 1/r behavior (where r is the Au-TM distance). [20] A simple estimate for the geometrical configuration considered here, corresponding to r about 7 Å for MgO and 8 Å for CaO, indicates that the electrostatic attraction does not exceed 0.35 eV and thus is not the dominant contribution, as also pointed out in ref [20].

As a last point, in order to disentangle the role of the impurity from that of the oxide matrix on the donor ability of the system, we have considered Au adsorption on Mo^{3+}:MgO and Cr^{3+}:CaO. The PBE results, Table 6.1, indicate that even Cr^{3+}:CaO is unable to donate electrons to Au, despite the fact that the Cr t_{2g} levels are higher in energy due to the lower crystal field splitting induced by the CaO matrix (larger lattice parameter). This result confirms that the presence of the heavy Mo atom and its redox properties are crucial in determining the charge transfer. The tendency of Mo to act as electron donor when introduced in the lattice in oxidation state up to +4 can be ascribed to the ionization potentials (IP) of the Mo atom. This grows by increasing the cationic charge: IP(Mo^{2+}) = 27.1 eV, IP(Mo^{3+}) = 46.4 eV, and IP(Mo^{4+}) = 54.5 eV.31 However, for Cr the ionization of the more contracted 3d electron increases more rapidly, IP(Cr^{2+}) = 31.0 eV, IP(Cr^{3+}) = 49.2 eV, and IP(Cr^{4+}) = 69.5 eV. [11] The consequence is that the cost of oxidizing the TM ion is the key factor determining the donor ability of the doped oxide. [20] As a counter-proof, let us consider a Mo^{3+} ion in a MgO matrix with an adsorbed Au atom on the surface. The results, Table 6.1, indicate that the adsorption properties are similar to those of Mo^{3+}:CaO and that the charge transfer takes place. However, the shorter lattice parameter of the MgO matrix increases the crystal field splitting, lowering the t_{2g} 4 Mo levels and making the charge transfer less favorable. Indeed, the Au adsorption energy is 1.20 eV on Mo^{3+}:MgO with an energy gain of only 0.2 eV compared to pure MgO (PBE results). For comparison, the increase in adsorption energy going from CaO to Mo^{3+}:CaO is of 0.75 eV.

6.4 Conclusions

The effect of doping simple oxides with transition metal ions has been addressed for the case of Cr and Mo impurities in MgO and CaO, by combining STM analysis with pure DFT and hybrid functionals calculations. The introduction of the foreign species in the lattice changes the local structure and introduces states in the oxide band gap. As these states are relatively high in energy, there is the possibility of electron transfer from the impurity to low-lying defect states resulting in TM^{n+} ions, with $n > 2$. Cation vacancies are possible defects to accommodate the TM electrons.

The stability of Cr and Mo impurities in MgO and CaO in different oxidation states, combined with compensating cation vacancies, has been addressed as a function of the environmental conditions. Our analysis shows that Cr:MgO is stable in the +3 oxidation state, in agreement with previous literature. In the case of Mo:CaO, Mo^{3+} is stable in oxygen poor conditions, and even higher oxidation states are expected in oxygen-rich conditions. Although our analysis is based on thermodynamic stability and does not take into account entropic and kinetic effects that can influence the defect formation and the growth mode, it clearly indicates a tendency of the heavier Mo atoms to donate d electrons to acceptor states.

The presence of TM impurity in the oxide changes the surface reactivity, as electron exchange can occur between the TM and the adsorbate. In the case of electronegative species, electrons can be transferred to the adsorbate with consequent oxidation of the TM ions. Gold adatoms can become negatively charged via this redox mechanism in both matrixes considered when the TM dopant is in $+2$ oxidation state. However, if the TM ion is in TM^{n+} oxidation state with n $>$ 2, the charge transfer is system dependent. In the case of Cr^{3+} in both MgO and CaO, the t_{2g} Cr states are so low in energy that no charge transfer can occur to adsorbed gold. Conversely, Mo^{3+} and Mo^{4+} are still able do donate electrons to gold, as their d states are higher in energy. However, the energy gain associated with the charge transfer decreases by increasing the Mo oxidation state. The difference between the two TM species relies in the decrease of the ionization potential along the group, which make the heavier atoms more prone to donate charge. The difference between Cr and Mo is evident starting from the third ionization potential. A detailed comparison of the two TM ions in the two matrixes considered indicates that the use of the CaO matrix, with a larger lattice parameter, reduces the crystal field splitting and the Madelung potential. Compared to MgO, these two effects concur in destabilizing the t_{2g} TM levels, favoring the charge transfer to the adsorbate. Although the oxide band gap is better described with hybrid functionals, our results indicate that the donor properties of the TM impurity are independent of the functional used. In conclusion, we have shown that TM dopants may exhibit rather different abilities to transfer charges into adsorbates, even if they belong to the same group in the periodic table. We therefore propose that incorporating second- or third-series TM ions into spacious oxide lattices is a reliable route to produce systems with good donor characteristics.

Bibliography

[1] P. Myrach, N. Nilius, S. Levchenko, A. Gonchar, T. Risse, K.P. Dinse, L.A Boatner, W. Frandsen, R. Horn, H.-J. Freund, R. Schlögl and M. Scheffler, *ChemCatChem* **2**, 854 (2010).

[2] Z. Hu, B. Li, X.Y. Sun and H. Metiu, *J. Phys. Chem. C* **115**, 3065 (2011).

[3] K.P. McKenna and A.L. Shluger, *Nat. Mater.* **7**, 859 (2008).

[4] S. Benedetti, H.M. Benia, N. Nilius, S. Valeri and H.-J. Freund, *Chem. Phys. Lett.* **430**, 330 (2006).

[5] X. Shao, P. Myrach, N. Nilius and H.-J. Freund, *Phys. Chem. C* **115**, 8784 (2011).

[6] F. Stavale, N. Nilius and H.-J. Freund, *New J. Phys.* **14**, No. 033006 (2012).

[7] J. Muscat, A. Wander and N.M. Harrison, *Chem. Phys. Lett.* **342**, 397 (2001).

[8] R.F.W. Bader, *Chem. Rev.* **91**, 893 (1991).

[9] M. Leslie and M.J. Gillan, *J. Phys. C: Solid State Phys* **18**, 973 (1985).

[10] S.L. Dudarev and G.A. Botton, S.Y. Savrasov, C.J. Humphreys, A.P. Sutton, *Phys. Rev. B* **57**, 1505 (1998).

[11] D.R. Lide, Ed. CRC Handbook of Chemistry and Physics; CRC Press: Boca Raton, FL, 2010.

[12] A.L. Schawlow, *J. Appl. Phys.* **33**, 395 (1962).

[13] J.P Larkin, G.F. Inbush and F. Dravnieks, *Phys. Rev. B* **7**, 495 (1973).

[14] Q.E. Wertz and P. Auzins, *Phys. Rev.* **106**, 484 (1957).

[15] G.F. Imbush, A.L. Schawlow, A.D. May and S. Sugano, *Phys. Rev.* **140**, A 830 (1965).

[16] A.M. Ferrari and G. Pacchioni, *J. Phys. Chem.* **99**, 17010 (1995).

[17] P. Baranek, G. Pinarello, C. Pisani and R. Dovesi, *Phys. Chem. Chem. Phys.* **2**, 3893 (2000).

[18] K. Reuter and M. Scheffler, *Phys. Rev. B* **65**, 035406 (2001).

[19] D.M. Roessler and W.C. Walker, *Phys. Rev.* **159**, 733 (1967).

[20] J. Andersin, J. Nevaóaota, K. Honkala and H. Häkkinen, *Angew. Chem., Int. Ed.* **52**, 1424 (2013).

Chapter 7

Controlling the charge state of single Mo-dopants in a CaO Film

The concept of doping is less developed for oxides with respect to semiconductors (where doping levels down to 10^{15} cm^{-3} can be safely installed nowadays [1]) , as various peculiarities of these materials hamper the detailed insight into the nature of dopants. Oxides are subject to self-doping either with native defects or unknown impurities, the concentration of which is difficult to control experimentally [2]. Both, lattice defects and external impurities may adopt different charge states in the oxide lattice [3], a variability that leads to strong compensation effects and is less common in semiconductors. Moreover, dopants in wide-gap oxides are often electrically inactive, as thermal excitation is insufficient to lift the electrons from the defect states in the gap to the bulk bands. As a result, the excess charges remain bound to their host ions. This situation may change, however, when adsorbates with low-lying affinity levels bind to the surface and charge transfer between dopant and ad-species becomes possible. This is the case we have shown in chapter 5 and 6 for the gold adsorption on Mo doped CaO. These results underline the large demand for basic information on the role of dopants in oxide materials [4].

The properties of dopants have been comprehensively studied by theo-

---

The results of this chapter have been reported in the following publication: Y. Cui, N. Nilius, H.-J. Freund, S. Prada, L. Giordano and G. Pacchioni, “Controlling the Charge State of Single Mo-Dopants in a CaO Film”, *Phys. Rev. B* **88**, 205421 (2013).

retical means [3,5,6], while experimental verification of the derived concepts is still scarce [7,8]. As the nature of dopants sensitively depends on their local environment, i.e. the interplay with other impurities or the surface, spatially resolved experiments are required to obtain a mechanistic insight into their functionality. Local methods are also suited to probe the spatial distribution of dopants in a lattice and to determine the critical length, over which charge transfer with ad-species occurs. Answer to these questions is a key to understand the role of dopants in the surface chemistry of oxides.

In this chapter, in a collaboration with the group of Prof. Freund at the Fritz-Haber-Institut in Berlin, we combine scanning tunneling microscopy (STM) at 10 K and density functional theory to probe the spatial distribution and electronic properties of Mo donors in wide-gap CaO films. We show that near-surface dopants are electrically active and can be charged / discharged in the electric field of the STM tip. This flexibility results from the proximity of the highest occupied Mo-donor level (HOMO) to the onset of the oxide conduction band (CB). All the experimental data reported in this chapter have been provided by the group of Prof. Freund.

7.1 Computational and experimental details

Computational details

Spin-polarized DFT calculation has been performed with the VASP code (see 2.3). PBE0 functionals with 25% non-local exchange were used for calculating the positions of Mo $4d$ levels inside the CaO band gap. Bulk Mo ions are placed in a (2×2×2) CaO supercell, while near surface dopants are modeled with a (3×3) surface cell of a five layers slab. For reciprocal space sampling, a (3×3×3) and (3×3×1) Monkhorst-Pack meshes are used, respectively.

Experimental details

CaO films of ≈25 ML thickness were prepared by physical vapor deposition of Ca onto a sputtered and annealed Mo(001) surface in 5x10^{-7} mbar of oxygen. Crystallization of the films was achieved by vacuum annealing to 800-1100 K and resulted in a sharp (1x1) square pattern in LEED, being

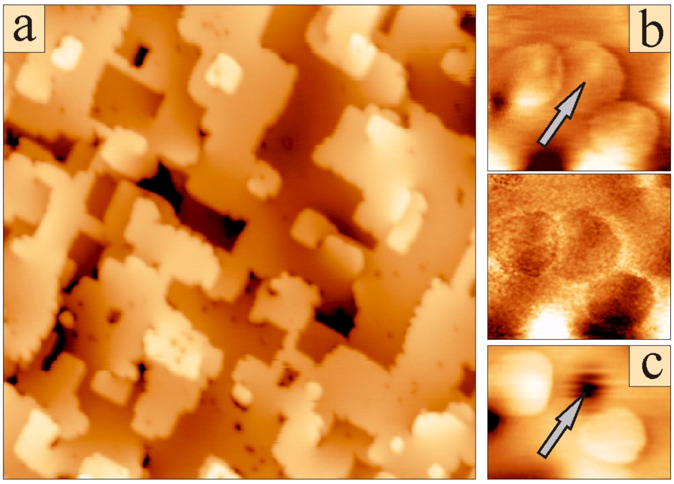

Figure 7.1: (a) Overview STM image of 25 ML CaO grown on Mo(001) (50x50 nm^2, 4.5 V). (b) Topographic and dI/dV image of charging rings related to three Mo donors in the surface region. (c) Adsorption of an O_2 molecule onto central feature leads to a suppression of the charging ring (11x8 nm^2, 2.5 V).

indicative for (001) terminated rocksalt CaO. Corresponding STM images displayed atomically-flat oxide terraces, separated by a network of step edges and dislocation lines that run along the non-polar CaO[100] direction (Fig. 7.1a). STM imaging was possible only for bias voltages above the CB-onset that was found to vary between 2.0-4.0 V depending on thickness and doping level of the film. Applying negative or low positive bias caused the tip to crash into the surface, suggesting that our films are too thick for electron transport via tunneling.

7.2 Results and discussion

In chapter 4 we have shown that the CaO films are self-doped due to spontaneous Mo diffusion out of the support at high temperature. Directly at the interface, the extra Mo occupies 25% of the cationic sites of the rocksalt lattice and arranges into a (2×2) superstructure. With increasing film thickness, the Mo concentration decreases due to a large activation energy for Mo diffusion, until hardly any dopants are detectable in the near-surface

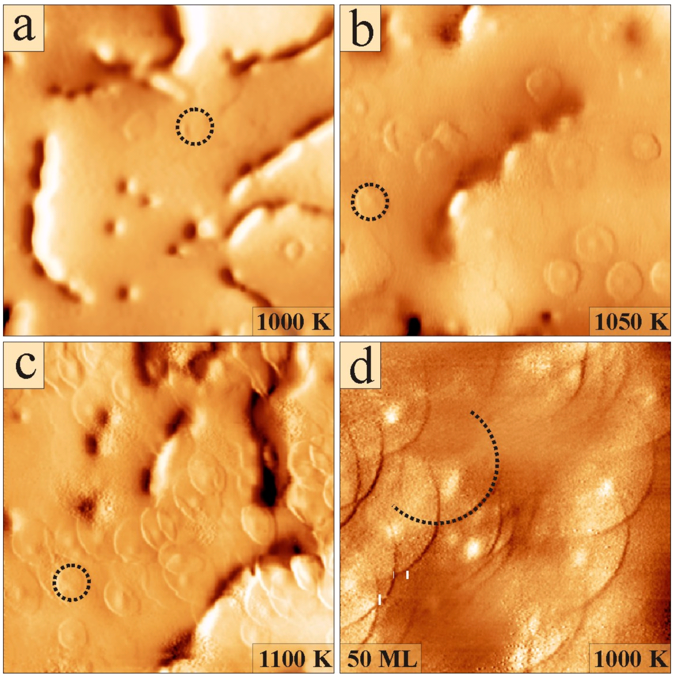

Figure 7.2: (a-c) STM images of 25 ML CaO annealed to the given temperatures (30x30 nm^2, 2.6 V). Note the increasing number of charging rings (see broken circle) upon annealing. (d) On 50 ML thick films, the diameter of charging rings is larger due to the inferior dielectric screening (30x30 nm^2, 4.4 V).

region of a 25 ML film. For even thicker films, Mo needs to be artificially introduced either via ion implantation or excessive heating of the sample to 1100 K. So far, the presence of Mo-ions was derived only indirectly from the modified adsorption behavior of the doped CaO (see chapter 5 and 6). With the new data, we are now able to determine position and charge state of the dopants in a direct experiment.

High-bias STM images of the film show a smooth morphology, only perturbed by a few point and line defects. With decreasing bias, characteristic rings appear on the CaO surface, the diameter of which varies with tunneling conditions (Fig. 7.1b). Whereas in topographic images the rings are discernible due to their enhanced height with respect to the surrounding, a bright circumference appears in differential conductance (dI/dV) maps taken with lock-in technique. In both cases, the surface plane itself is perfect and

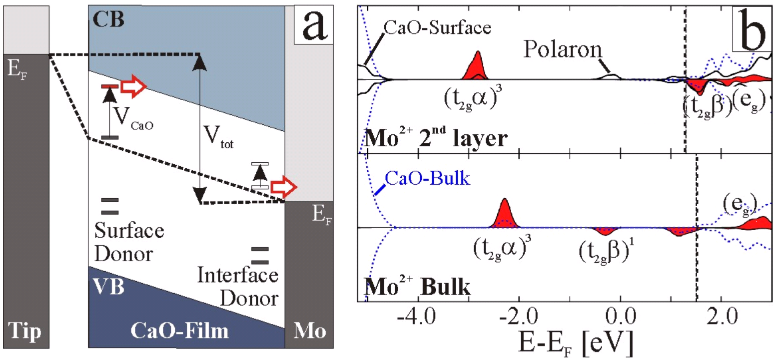

Figure 7.3: (a) Potential diagram of a STM junction containing a doped CaO film. The tip-electric field induces an upward bending of the oxide bands, which leads eventually to an electron transfer from the Mo^{2+} HOMO to the CB of the CaO. (b) PDOS of a Mo^{2+} donor in bulk CaO and the 2^{nd} (subsurface) plane. The dashed lines mark the CB-onset.

no atom-size defects are identified in the ring centers. To connect the ring features in STM with Mo dopants in the lattice, we have changed the Mo concentration by annealing the films to different temperatures, thus altering the thermodynamic stimulus for Mo diffusion (Fig. 7.2). Indeed, the density of ring structures was found to rise from $5x10^{11}$ to $5x10^{12}$ cm^{-2} when going from low- to high-temperature films. In the latter case, the rings overlapped without visible interference, suggesting that features indeed originate from isolated species in the oxide matrix.

The rings seen in STM can be explained with charging events of the Mo dopants in the tip electric field, a mechanism that has been identified for semiconducting [7,9] and organic layers [10] before. The Mo ions at Ca substitional sites introduce a number of defect levels with Mo 4*d* character inside the CaO band gap (see chapter 5 and 6). While their energy position is governed by the octahedral crystal field exerted by neighboring O^{2-} anions, their occupancy reflects the oxidation state of the dopants. Charging may now occur due to an upward bending of the CaO bands in presence of a positively biased tip, which temporary destabilizes the HOMO level of the dopant [11]. Two final states are conceivable for the electron after detachment from the Mo-HOMO (Fig. 7.3a). For dopants close to the interface, the HOMO may be pushed above the Fermi level of the system and

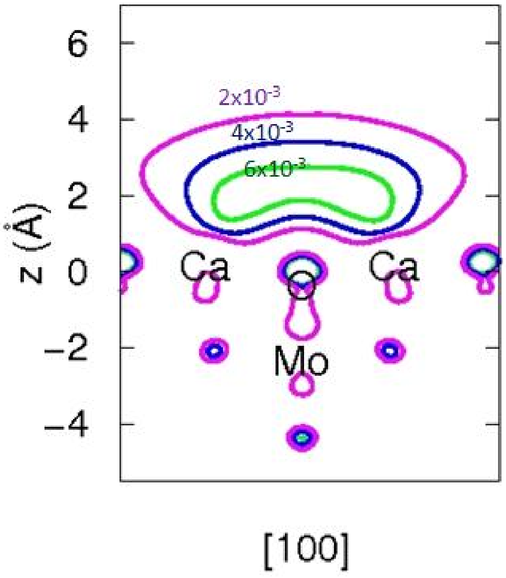

Figure 7.4: Projection of charge density isosurfaces (e/Å^3) of the polaronic state over a plane along the [100] direction for subsurface Mo. The origin of the z axis is located at the oxide surface.

discharges into the empty states of the metal substrate. In contrast, the HOMO electron of a near-surface dopant may tunnel into the CB of adjacent CaO patches that are less affected by the tip-induced band bending and therefore lower in energy. The amount of band bending in STM is given by the bias ratio between V_{CaO}, being the voltage drop due to insufficient dielectric screening inside the oxide film and the total sample bias V_{tot} [12]:

$$\frac{V_{tot}}{V_{CaO}} = \left(\frac{\epsilon_{CaO} d_{vac}}{\epsilon_{vac} d_{CaO}}\right). \tag{7.1}$$

Here, $\epsilon_{CaO} = 10$ is the oxide dielectric constant, while d_{vac} and d_{CaO} denote the mean widths of vacuum gap (≈0.5 nm) and oxide film (≈6 nm), respectively. For a bias range of 3-5 V, in which charging rings are observed in STM, the tip-induced band offsets amount to 1.6-2.8 V in near-surface CaO planes, but drop below 0.5 V in the interface region of the oxide film.

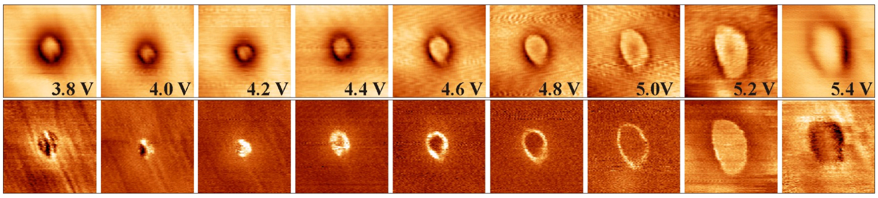

Figure 7.5: Topographic (top) and dI/dV maps (bottom) of a single Mo donor measured as function of bias voltages. The asymmetry of the ring reflects the deviation of the tip apex from a perfect sphere (5x5 nm^2).

Comparing these numbers to the position of Mo defect levels, as computed with a hybrid functional PBE0-DFT approach yields a first hint on which of the two proposed charging routes is more likely. In the ideal CaO bulk lattice with a computed band gap of 6.1 eV, a Mo^{2+} substitutional ion has the electron configuration $(t_{2g}\alpha)^3(t_{2g}\ \beta)^1(e_g)^0$ with the $(t_{2g}\beta)$-type HOMO being located at 1.8 eV below the CB-onset (Fig. 7.3b). Due to the gradual reduction in gap size, the Mo^{2+} HOMO shifts towards the band edge upon approaching the CaO surface, until it merges with the CB by forming a polaron with strong Ca 4*s* character. Formally, the Mo^{2+} loses one electron to the surface polaron, which is further stabilized by the attractive potential of the resulting Mo^{3+} ion. The polaronic state is spatially localized (small polaron, see Fig. 7.4), in agreement with its deep position with respect to the band edge (1.6 eV for Mo^{2+} in the 2nd sub-surface plane). In contrast, a Mo^{2+} directly in the surface retains all four 4d electrons and, due to the C_{4V} symmetry, assumes a high spin $(e)^2(b2)^1(a1)^1(b1)^0$ configuration with the HOMO being at 3.5 eV below the CB edge. Also in bulk CaO, Mo^{3+} ions may form due to spontaneous charge transfer to electron trapping defects, e.g. dislocation lines. However, these ions are stable against charging in the tip-electric field, as their $(t_{2g}\alpha)$-type HOMO lies almost 5 eV below the CB edge. The same is true for dopants in the interface region, which immediately loose an electron to the metal substrate by adopting a stable 3+ charge state. The residual $(t_{2g}\ \alpha)^3$ electrons of the ion can be removed neither, as their required energy to reach the metal Fermi level (1.5 eV) is not provided by the small band bending at the interface (Fig. 7.3a). Note that charging is generally excluded for Mo ions in higher oxidation states, i.e. +4, +5 or +6, as their electrons occupy low-lying states in the CaO

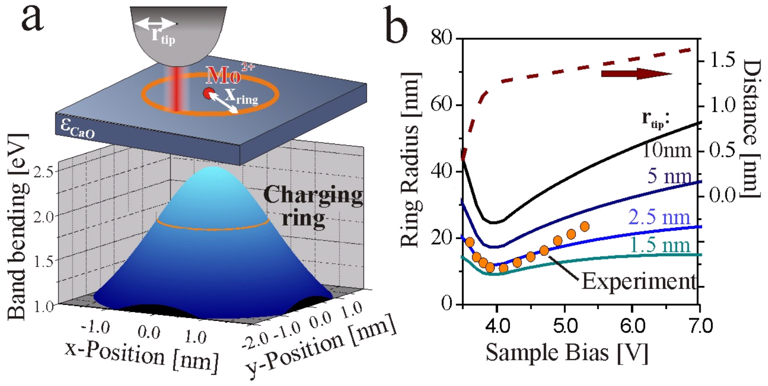

Figure 7.6: (a) Real-space model of a charging ring and shift of the Mo^{2+} HOMO calculated for 5.0 V sample bias and 2.5 nm tip radius. Electron transfer into the CB takes place when the level crosses the orange line ($\Delta E = 1.6$ eV). (b) Ring diameter shown as a function of tip radius and sample bias. The experimental tip-sample distance that enters the calculations is marked by the dashed line.

gap that cannot be destabilized by a tip-induced perturbation anymore. In conclusion, from all species considered here only the Mo^{2+} ions in vicinity to the surface are susceptible for a tip-induced charging. This result is corroborated by direct experimental evidence. After dosing oxygen, as an electron-accepting molecule, the ring structures disappear from the surface, because the low-lying oxygen $2\pi^*$ level takes the HOMO electron of a Mo^{2+} donor (Fig. 7.1b,c) [13]. At the premise of a limited transfer length of electrons in CaO, the participating Mo donor needs to be located in a near-surface region and interfacial species cannot be accounted for the rings seen in STM.

Further support comes from a careful analysis of the ring diameters and their dependence on the tunneling parameters (Fig. 7.5). The ring structures become visible due to the non-local character of band bending in the STM, which enables a charge transfer out of a Mo donor even at tip positions away from the dopant. [11] Mathematically, charging occurs when the tip-induced band offset at the dopant position $V_{Cao}(x)$ matches the binding energy of the Mo-HOMO with respect to the unperturbed CB edge (Fig. 7.6a). At this moment, the bound electron delocalizes over an extended CaO region and the positive charge directly at the donor site increases. The associated

Coulomb attraction partially compensates the tip-induced band shift, with the result that the tip electrons find more final states for tunneling and a circular region around the donor appears bright. Simultaneously, a sharp ring pops up in the conductance maps, reflecting the sudden rise in the accessible CaO state-density upon charging (Fig. 7.1b). The deviation of the perturbed region from an ideal circle hereby mirrors the asymmetry of the tip apex, giving rise to radial differences in the band bending. Assuming a spherical tip with radius r_{tip}, the size of the charging rings x_{ring} can be calculated from the bias division in the tunnel junction:

$$\frac{V_{tot}}{V_{CaO}} = \frac{\epsilon_{CaO}(d_{Vac} + r_{tip} - \sqrt{r_{tip}^2 - x_{ring}^2})}{\epsilon_{Vac} d_{CaO}} + 1. \tag{7.2}$$

In Fig. 7.6b, we have plotted the computed ring radii for different bias voltages and tip sizes, using the HOMO energy of a Mo^{2+} in the 2^{nd} subsurface plane (1.6 eV) as input parameter. The tip-sample distance d_{vac} was determined from experimental z-V curves by adding a distance offset of 0.5 nm to the measured curve. This model is able to reproduce the evolution of ring diameters observed in the experiment. Whereas the initial decrease in size is caused by a rapid retraction of the tip from the surface when the oxide CB becomes accessible for tunneling, the subsequent increase reflects the larger band bending at higher bias. Reasonable agreement between simulation and experiment is obtained for a tip radius of 2.5 nm, a value that is compatible with the spatial resolution in our images. Not surprisingly, thicker oxide films produce larger ring sizes due to a reduced screening of the tip electric field, an effect that becomes evident when comparing images taken on 25 and 50 ML thick films (Fig. 7.2c,d). We want to emphasize here that all charging rings in one image series have roughly the same diameter, indicating a similar position of the Mo donors with respect to the surface. In case of a homogeneous distribution of active dopants along the film normal, we would expect a much larger distribution of rings sizes than observed. Interestingly, we find no sign for a surface accumulation of Mo, although most of the active species seem to occupy positions in the topmost subsurface planes. The computed order of stability of the Mo position into the oxide film at the PBE0 level is: 2^{nd} layer $>$ 1^{st} layer $>$ 3^{rd} layer, but the differences are small, of the order of 0.2-0.3 eV.

7.3 Conclusions

In conclusion, ring structures observed in STM images of a CaO thin film have been connected to temporary charging events of Mo donors embedded in the oxide lattice. The rings develop as Mo^{2+} ions in a near surface region transfer their top-most electron to the CaO conduction band in response to the local electric field of the STM tip. This is a direct proof of the presence of Mo close to the oxide surface.

Bibliography

[1] B. I. Shklovskii and A.L. Efros, Electronic properties of doped semiconductors (Springer, Berlin, 1984).

[2] S. Wendt et al., *Science* **320**, 1755 (2008).

[3] H. Y. Kim, H. M. Lee, R. G. S. Pala, V. Shapovalov, and H. Metiu, *J. Phys. Chem. C* **112**, 12398 (2008).; V. Shapovalov and H. Metiu, *J. Catal.* **245**, 205 (2007).

[4] X. Sun, B. Li and H. Metiu, *J. Phys. Chem. C* **117**, 7114 (2013).

[5] M. Nolan and G. W. Watson, *Surf. Sci.* **586**, 25 (2005).

[6] G. Pacchioni et al., *J. Phys.: Condens. Matter* **16**, S2497 (2004).

[7] H. Zheng, J. Kröger and R. Berndt, *Phys. Rev. Lett.* **108**, 076801 (2012).

[8] X. Shao, N. Nilius and H.-J. Freund, *J. Am. Chem. Soc.* **134**, 2532 (2012).

[9] K. Teichmann et al., *Phys. Rev. Lett.* **101**, 076103 (2008).

[10] G. V. Nazin, X. H. Qiu and W. Ho, *Phys. Rev. Lett.* **95**, 166103 (2005).

[11] R. M. Feenstra, Y. Dong, M. P. Semtsiv and W. T. Masselink, *Nanotechnology* **18**, 044015 (2007).

[12] S. W. Wu, G. V. Nazin, X. Chen, X. H. Qiu and W. Ho, *Phys. Rev. Lett.* **93**, 236802 (2004).

[13] Y. Cui, N. Nilius, X. Shao, H. J. Freund, M. Baldowski and J. Sauer, *Angew. Chem. Int. Ed.* (submitted).

Chapter 8

Tuning work function change via doping thin film materials

In the introduction we pointed out the importance of doping oxide in tailoring "new" materials, because even simple binary metal oxides like MgO may radically change their properties when doped by other elements (see section 1.5). In the chapter 5 and 6 we showed the ability to engineer the properties of adsorbed metal particles by doping simple oxides with transition metals. Another possibility to tailor the properties of adsorbed metal catalysts is to use very thin oxide films supported by metals as a substrate. In fact very thin oxide films might be considered as the "electrically conductive" counterpart of their insulating bulk, since at the nanoscale charge transport through the film remains possible via electron tunneling. One important parameter which determines the occurrence and even the direction of the charge transfer is the work function of the metal/oxide system: a low work function may result in charge transfer from the metal/oxide interface to supported nanoparticles or molecular adsorbates; a high work function can induce charge transfer in the opposite direction, from the surface toward the metal support (see section 1.2). Tuning the work function of the system is thus essential in order to design oxide thin films with desired prop-

---

The results of this chapter have been reported in the following publication: S. Prada, L. Giordano, G. Pacchioni "Li, Al, and Ni Substitutional Doping in MgO Ultrathin Films on Metals: Work Function Tuning via Charge Compensation" *J. Phys. Chem. C* **116**, 5781 (2012).

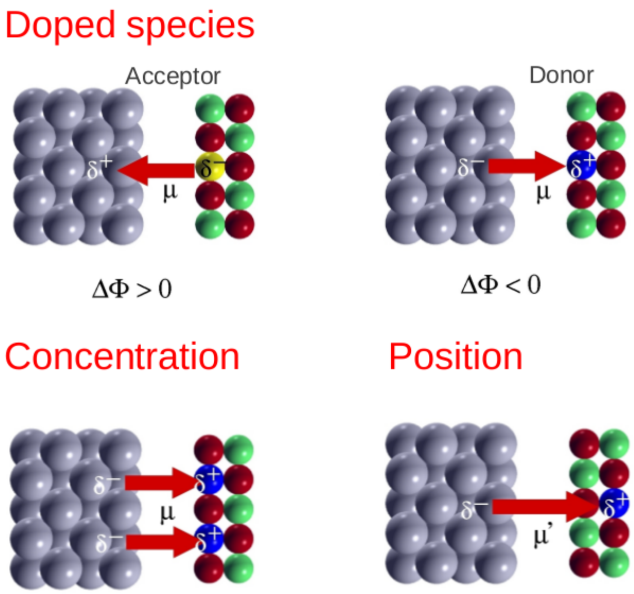

Figure 8.1: Important parameters of doped oxides that determine changes in the surface dipole μ and thus in the metal work function. Top panel) Donor-like or acceptor-like character of the doped species. Bottom panel) Dopant concentration and dopant position in the oxide film.

erties. In this chapter we account for the possibility to employ oxide doping to modulate this important parameter.

In the introduction we discussed the effect of thin films deposition on metals substrate in modifying the work function (see section 1.3 and Ref. [1,2]). In absence of a dipole moment in the oxide, this change is determined by two major contributions: a charge transfer between metal and adsorbates, where a different sign in the transfer increases or reduces the work function, and an electrostatic compressive effect that always reduces Φ. Depending on the nature of the oxide the combination of these two effects can generate an increase or a reduction of the substrate work function value. However, since this change only depends on the nature of the deposited oxide varying slightly with the film thickness, there is no way to control it finely. The idea of doping the adsorbed thin film is an attempt to tune finely the work function. By varying parameters like nature, position, and concentration of dopants within the film, it is possible in principle to tune the work function of the supported film in a desired way (Figure 8.1).

In the present chapter we analyze the structural and electronic properties of cationic-substituted MgO films grown on Mo(100), a substrate commonly used to grow MgO in the experiments. [3] We chose simple monovalent and three-valent elements, Li and Al, respectively, in order to investigate the nature of heterovalent impurities substituting the Mg^{2+} cation in MgO/Mo(100). The rationale is the following. Li, being monovalent, must induce the formation of an O^- ion in order to keep neutrality; the O^- ion can trap electrons from the metal support to form O^{2-} ions. On the other hand, Al doping will provide an extra electron which is either trapped at defects (vacancies, grain boundaries, etc.) or transferred to the metal support or at the metal/oxide interface. The charge transfer will result in a dipole change which increases or lowers Φ depending on the direction of the electron flow (Figure 8.1). We also studied Ni impurities in MgO films in order to gain insight into doping with transition metals, where different oxidation states are possible. The role of the substrate is highlighted by comparing the properties of doped MgO/Mo(100) and, in the case of Al doping, of MgO/Ag(100) films to the unsupported counterparts.

8.1 Computational details

Spin-polarized calculations have been performed in the framework of density functional theory (DFT), using a periodic approach and a plane-waves basis set, as implemented in the VASP code (see section 2.3) with a kinetic energy cutoff of 400 eV. The exchange-correlation potential is treated within the Perdew-Wang 91 (PW91) gradient-corrected approximation [4] and we employ the projector-augmented plane-wave (PAW) method.

The MgO film on Mo(100) surface is described by depositing three MgO layers on one side of a four-layer thick Mo slab at the optimized lattice parameter (3.15 Å). A similar setup is used for MgO/Ag (Ag optimized lattice parameter = 4.16 Å). For the MgO(100) surface, we use a three-layer slab at the optimized MgO lattice parameter (4.25 Å). The slabs are separated by at least 10 Å of vacuum, and the dipole correction is applied in order to eliminate the residual dipoles in the direction perpendicular to the surface. The two bottom layers of Mo or Ag (one layer in the case of MgO(100)) are fixed to the bulk position, while all the other coordinates are fully relaxed until atomic forces are lower than 0.01 eV/Å. For the description of the structural and electronic properties, a (3 × 3) supercell is used, with a (4 × 4 × 1) Monkhorst-Pack k-points mesh.

Trends in the dopants-induced work function change have been addressed by varying the concentrations of dopants making use of different in-plane supercells, with an equivalent k-point sampling. In the most diluted configuration, one impurity atom is placed in a (4 × 4) unit cell, corresponding to an in-plane coverage of 1/16 and a dopants concentration of $1/48 \approx 2\%$. The largest concentrations are described by considering a $(\sqrt{2} \times \sqrt{2})\mathrm{R}45^\circ$ supercell, corresponding to a doping of 16.6%, for Al and Ni, while for Li also a higher concentration of 33% has been considered ((1 × 1) unit cell). Notice that the different concentrations have been considered by doping one layer at a time so that the simultaneous doping of the different oxide layers is not included in our description.

Atomic charges are obtained within the scheme of charge density decomposition proposed by Bader, [5] while the magnetic moments of ions are estimated from electronic densities projected into atomic spheres. The work function Φ is estimated as the difference between the vacuum level and the Fermi energy.

8.2 Results and discussion

8.2.1 Li-doped MgO

When a lithium impurity substitutes Mg in bulk MgO or on the MgO(100) surface, it enters in the lattice as Li^+, as shown by the Bader charge of +0.88 and by the absence of spin density on Li. As a consequence, a hole is created in the oxide O 2p band, Figure 8.2a. In our calculations the hole is delocalized over the four O nearest neighbors of the Li atom, due to the shortcomings of pure DFT calculations in describing localized electronic states [6]. A more sophisticated approach (for instance, DFT with hybrid functionals) [7] would be required to correctly investigate the hole localization but is not essential for the problem described here.

When the MgO film is supported on Mo(100), the properties of Li-doped MgO are completely different. The Bader charge analysis shows that Li maintains the +1 oxidation state, Table 8.1, but a charge transfer occurs

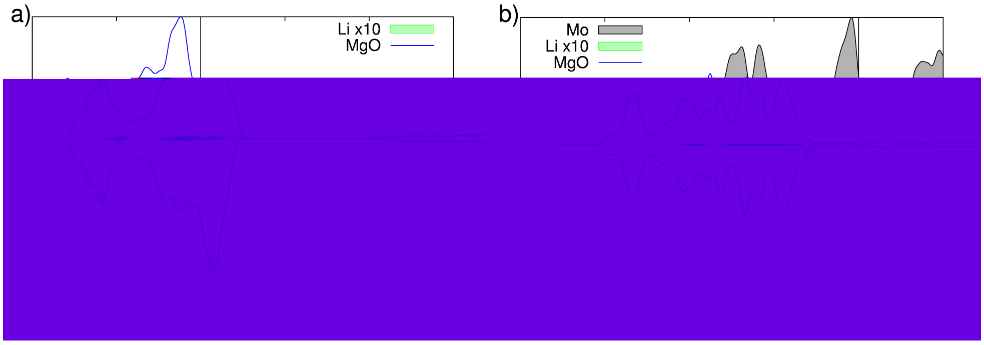

Figure 8.2: Projected density of states of (a) Li-doped MgO(100) and (b) Li-doped MgO(3 L)/Mo(100). The Li atom is in the surface layer (1/9 ML). The zero of energy is fixed at the Fermi energy, E_F. The Li-projected DOS have been multiplied by 10 in both panels.

from the Mo metal to fill the hole in the O 2p states. This is clearly shown by the projected density of states (DOS), Figure 8.2b, where the O 2p band is completely filled and well below the Fermi energy, E_F. This effect is independent of the position of the dopant in the film and represents a mechanism of valence compensation specific of metal-supported insulating films. A similar effect has been reported for defective [8] or for Al-doped silica films on Mo(112) [9].

The process of restoring the original valence of the O anions by charge transfer from the metal has important consequences on the properties of the system. Indeed, the dipole moment, generated by the electron transfer, increases the work function. The work function of the undoped MgO(3L)/Mo film, 2.17 eV, [1] is considerably smaller than for the Li-doped films, Table 8.1, no matter which is the dopants concentration. On the other hand, Φ may assume very different values depending on the Li concentration and position, Figure 8.3a. The work function increases linearly with the dopants concentration, indicating that also for the largest concentration considered (33%), corresponding to the substitution of all the Mg atoms of one layer with Li, all O ions are in the -2 charge state. For a given Li concentration, Φ depends on the position of the impurity in the film. When Li is in the interface layer, the dipole moment induced by the charge transfer is the smallest and, for the lowest concentration considered, the work function

	$d_{interface}$	ΔE eV	$q(M)$ $\|e\|$	$\mu(M)$ μ_B	Φ eV	$\Delta\Phi$ eV
			Li-Doped MgO/Mo			
interface	2.14	0.00	0.87	0.00	2.38	+0.21
center	2.15	0.25	0.88	0.00	2.89	+0.72
top	2.15	0.26	0.89	0.00	3.25	+1.08
			Al-Doped MgO/Mo			
interface	2.15	0.17	2.22	0.00	2.06	-0.11
center	2.15	0.00	2.44	0.00	2.14	-0.03
top	2.15	0.51	2.35	0.00	2.10	-0.07
			Ni-Doped MgO/Mo			
interface	2.09	0.00	-0.28	0.00	2.53	+0.36
center	2.15	2.03	0.96	1.64	2.47	+0.30
top	2.15	2.04	0.89	1.47	2.86	+0.69

Table 8.1: Structural and electronic properties of metal-doped MgO/Mo(100), computed with the (3 × 3) supercell. $d_{interface}$ is the average interface distance (the interface distance for the undoped MgO(3 L)/Mo(100) is 2.15 Å); ΔE is the energy difference with respect to the most stable situation taken as zero reference; $q(M)$ and $\mu(M)$ are the net Bader charge and the magnetic moment of the metal dopant, respectively; Φ is the work function and $\Delta\Phi$ the work function change with respect to the undoped film (Φ_{Mo} = 3.88 eV and $\Phi_{MgO/Mo}$ = 2.17 eV)

is basically the same as for the MgO(3L)/Mo(100) film, Figure 8.3a. This is consistent with the classical view that the surface dipole depends on the net charge transferred (q) and on the distance d between the charge in the insulator and the image charge formed in the metal. When the Li atom is at the interface, the distance d is short and the surface dipole is smaller. On the contrary, the dipole moment is largest when the impurity is in the surface layer; a Li concentration of about 10% can give a work function of more than 4 eV, Figure 8.3a.

From the energetic point of view, having the impurity Li atom at the interface is always preferred, while Li incorporation in the inner and surface layers has essentially the same stability, Table 8.1.

It should be noted that doping the MgO film with substitutional alkali atoms induces an increase in the work function while alkali atom adsorption on the surface of MgO(nL)/Ag(100) leads to an opposite effect. [10] This is because in the case of Li doping electrons flow from the metal toward the oxide to fill the holes in the O 2p states, while in the case of Li atom adsorption on the MgO surface this forms a Li^+ ion and the valence electron is transferred to the metal support via tunnelling through the film. The resulting surface dipole has thus an opposite sign, leading to opposite changes in work function.

8.2.2 Al-doped MgO

A substitutional Al impurity in MgO becomes Al^{3+}, since the +2 oxidation state of Al is unstable. Of the three valence electrons, two are transferred to the O 2p states and one to the oxide conduction band, as shown by the DOS in Figure 8.4a, and is then delocalized. It is worth noticing that this charge transfer can be a spurious effect of the underestimation of the oxide band gap employing pure DFT functionals. On the other hand, in real systems low energy states, localized in the band gap, can exist due to defects or grain boundaries, which can trap the extra electron. [11–13] Thus, the Al:MgO system should likely consist of Al^{3+} substitutional impurities and electrons trapped at localized defective sites.

When the oxide is supported on Mo, the Al impurity maintains the +3 oxidation state. This is confirmed by the Bader charges $>2|e|$, Table 8.1, which are of the same order as obtained on the unsupported MgO, and by the absence of spin density on Al. Contrary to unsupported MgO, the Al

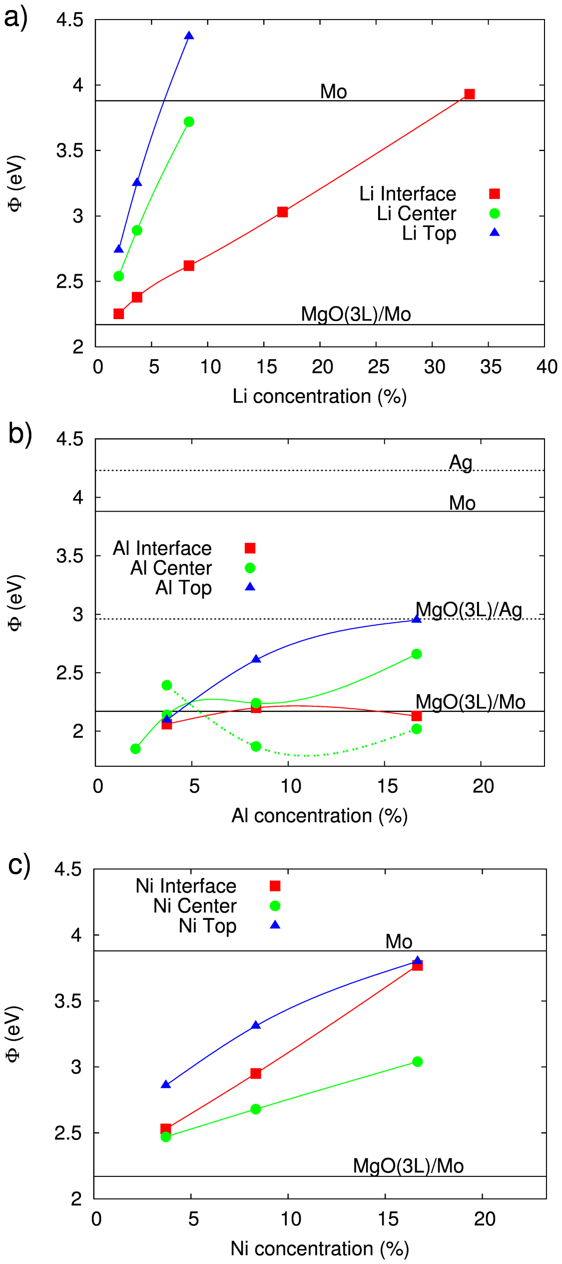

Figure 8.3: Work function of (a) Li-doped, (b) Al-doped, and (c) Ni-doped MgO(3 L)/Mo(100) films as a function of the dopant concentration. The impurity atoms are inserted in the interfacial, inner, or top layer. In (b) the work function of Al-doped MgO(3 L)/ Ag(100) with Al in the inner layer is also reported (dotted line).

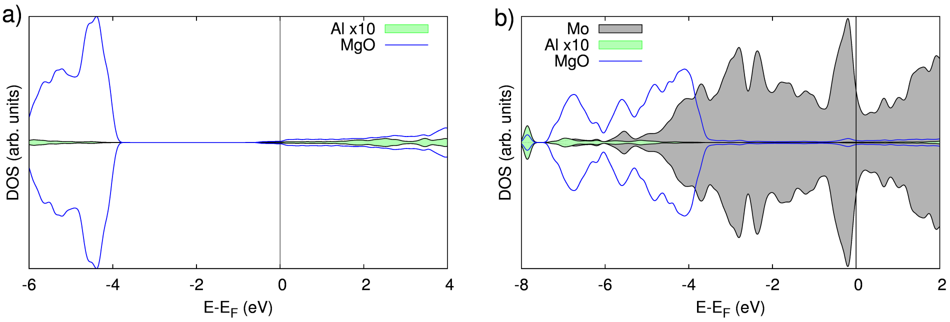

Figure 8.4: Projected density of states of (a) Al-doped MgO(100) and (b) Al-doped MgO(3 L)/Mo(100). The Al atom is in the surface layer (1/9 ML). The zero of energy is fixed at the Fermi energy, E_F. The Al-projected DOS have been multiplied by 10 in both panels.

excess electron can now be transferred to the metal substrate, although the conduction band edge is quite close to the Fermi level, indicating that in this case the transfer of the electron to the oxide conduction band could be competitive with the charge transfer to the metal support. However, the analysis of the Bader charges indicates that the excess electron is transferred to the Mo metal.

The charge transfer toward Mo is also proven by the decrease of work function obtained for low Al concentrations, Table 8.1 and Figure 8.3b. The work function change is much smaller than in the case of Li-doped MgO because the MgO/ Mo interface is already electron-rich, due to the compression of the metal electron density in the presence of MgO [1, 2] and can hardly accommodate extra electrons. Stated differently, the work function of the ideal MgO/Mo(100) interface is already very low, about 2 eV, and can be hardly reduced by oxide doping. It should be noted that the reported data are obtained for the favorable O-on-top configuration of the MgO/Mo film and refer then to the region of the islands with this interface register, which cannot be achieved on the entire film due to the lattice mismatch between MgO and Mo. [14] The difficulty of the interface to accept extra electrons is also reflected in the behavior as a function of the impurity concentration, Figure 8.3b. For a charge transfer of one electron per Al atom, independent of the in-plane concentration, one would expect a linear decreasing behavior.

Conversely, we observe that for the interface doping Φ is almost independent of the coverage, while for doping of the internal and surface layers the work function increases with concentration. These unexpected trends are the result of the combined effect of a smaller charge transfer (the aluminum Bader charge in the surface layer goes from 2.35 |e| in the (3 × 3) to 1.92 |e| in the $(\sqrt{2} \times \sqrt{2})$R45° unit cell), also due to some Al-Al interaction and, more important, to the occurrence of some oxide structural relaxation which counterbalances the electronic effects. The structural rearrangement induced by the introduction of the small Al^{3+} cation in the lattice is also the origin of the different trend in stability of the different configurations (the Al^{3+} ionic radius is 0.54 Å, to be compared to 0.72 Å of Mg^{2+} and 0.76 Å of Li^{+}), Table 8.1.

In order to verify that the small change of the work function is due to the initial low value of Φ for the undoped MgO/Mo(100) system, we have considered a MgO(3 L) film grown on Ag(100) where Φ for the undoped film is about 1 eV larger (2.96 eV). We restrict our analysis to the case of doping the central layer, since this is the most stable in the case of MgO/Mo, Table 8.1. For the lowest Al concentrations, Figure 8.3b, we observe indeed a sizeable decrease of the work function, which is of the order of 0.5 eV for an Al concentration of 3.7% and about 1 eV for a concentration of 8.3%. At higher dopant concentration the work function raises also for this system due to the combined effect of reduced charge transfer and structural distortion, as for the MgO/Mo case.

8.2.3 Ni-doped MgO

In bulk MgO Ni^{2+} substitutes the Mg^{2+} cation giving rise to MgO/NiO solid solutions. [15] The resulting electronic configuration of Ni^{2+} is $3d^8$ and is clearly visible in the Ni-projected DOS, Figure 8.5a, by the presence of two unpaired electrons on Ni (Bader charge of 1.19 |e|). For MgO/Mo(100) films, the nature of the Ni impurity critically depends on the position inside the film. When the Ni is in the central or surface layer the $3d(x^2 - y^2)$ state, which is empty in unsupported MgO, becomes filled, as shown by the PDOS in Figure 8.5b, and Ni assumes the formal +1 oxidation state (Ni^{+}, $3d^9$). However, the electron transfer is incomplete, as reflected by the Ni magnetization of 1.5 μ_B, and is slightly larger when Ni is in the surface layer. The charge transfer is induced by the relative position of empty Ni 3d

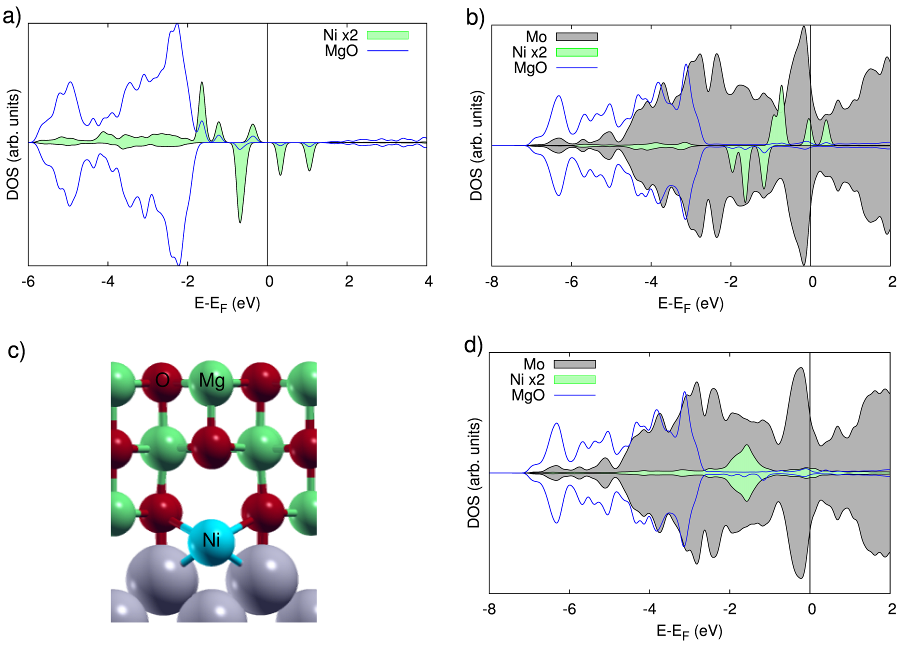

Figure 8.5: Projected density of states of (a) Ni-doped MgO(100) and (b) Ni-doped MgO(3 L)/Mo(100). The Ni atom is in the surface layer (1/9 ML). (c) Structure of substitutional Ni in the interface layer. (d) Projected DOS of Ni-doped MgO/Mo(100) with Ni in the interface layer (1/9 ML). The zero of energy is fixed at the Fermi energy, EF. The Ni-projected DOS have been multiplied by 2.

states with respect to the Fermi level of the oxide/metal system. Having the MgO/Mo interface a very low work function (high E_F), the Ni 3d(x^2 - y^2) state falls below E_F, and electrons are transferred into this state. On other substrates, like Ag, the work function of the combined oxide/metal system is higher (about 3 eV), so that the charge flow is not expected to occur and Ni should maintain the +2 oxidation state.

A completely different effect is found for the Ni atoms in the interface layer, as Ni undergoes a strong structural relaxation toward the metal substrate, Figure 8.5c. The small and negative net charge, Table 8.1, indicates that the impurity atom in contact with Mo has turned metallic, as confirmed by the PDOS in Figure 8.5d. Moreover, the absence of magnetic moment indicates that the Ni states strongly hybridize with the Mo states and lose the atomic character. The same magnetic quenching is observed by adsorbing a single Ni adatom on Mo(100). To summarize, no matter what the concentration of Ni impurities is, at the MgO/Mo interface we observe complete metallization of the Ni ions, while in the inner and surface layers Ni assumes an oxidation state intermediate between +2 (Ni^{2+}, $3d^8$) and +1 (Ni^+, $3d^9$).

The Ni metallization is accompanied by a large energy gain, Table 8.1. This indicates that the Ni doping of the MgO layers other than the interface, where the cation substitution is 2 eV less stable, can be obtained only out of thermodynamic equilibrium.

The trends of the work function as a function of the coverage reflect the Ni electronic configurations, Figure 8.3c. All cases show an almost linear increase of Φ with Ni concentration, indicating that the electron transfer from the substrate to the impurity stays constant in the range of concentrations considered. It is worth noticing that in our system we assume a ferromagnetic coupling of the Ni impurities. For the largest concentrations an antiferromagnetic coupling is in fact preferred, with implications on the electronic structure and the work function change. Interestingly, the slope of the work function change is the highest when Ni is in contact with Mo. This is because the Ni metallization requires the transfer of two electrons from Mo to Ni^{2+}. The resulting dipole moment is thus larger despite the smaller impurity/substrate distance. Furthermore, the linear behavior indicates that the Ni metallization does not depend on Ni coverage, as confirmed by the absence of magnetization on Ni and by the constant Bader charge, for all the configurations considered with Ni at the interface.

8.3 Conclusions

A possible way to modify the work function of an oxide ultrathin film is based on the selective doping with heteroatoms of the oxide phase. In this chapter we have considered three potential doping elements which replace a Mg^{2+} cation in a MgO thin film supported on Mo(100) or Ag(100). The first case considered is that of a Li impurity. In bulk MgO the presence of the monovalent cation results in the formation of holes in the O 2p valence band. On a supported MgO/ Mo(100) film, electrons flow from the

MgO/Mo interface to the O ions of the oxide to fill the holes and restore the formal -2 charge of the O anions. This results in a surface dipole whose direction is such to considerably increase the work function of the system. An opposite effect could take place if the Mg^{2+} cations are replaced by trivalent Al. Al in MgO enters as a Al^{3+} ion and thus donates an extra electron to the system. On bulk MgO this extra electron can be delocalized in the conduction band [17] or, more realistically, can be trapped at defect sites of the material. On MgO/Mo(100), the electron is transferred to the Mo metal, resulting in a charge transfer and a surface dipole that should decrease the work function. Actually, only for very low Al concentrations is this effect observed, and it is rather weak. The reason is that the work function of the perfect MgO/Mo(100) interface is already very low, about 2 eV, and cannot be further reduced. Other mechanisms enter in action (e.g., film relaxation) which counterbalance the effect of the charge transfer. In this respect a more interesting system is that of MgO films supported on Ag(100). Here in fact the initial work function, about 3 eV, is 1 eV larger than for MgO/Mo(100), and its reduction by selective doping is possible. Indeed, in this case a work function reduction can be obtained in a larger range of dopant concentrations.

The last case considered is that of a Ni ion replacing the Mg cation in MgO. Ni enters as Ni^{2+} ($3d^8$) in the host material, so that no charge unbalance is created. However, in the supported thin film the partly filled e_g states are in resonance with the Mo Fermi level so that a partial charge transfer is observed that turns the Ni ion in a charge state close to Ni^+ ($3d^9$) for Ni in the central and surface layers. Since the charge transfer is from the metal toward the oxide, the work function increases. On the other hand, the configuration with Ni at the interface is largely preferred as the direct interaction with the Mo surface causes a metallization of the impurity atoms. The metallization requires a charge transfer of two electrons from the Mo substrate, which increases the work function considerably.

In conclusion, we have shown that doping an oxide thin film can be a way to induce electron transfer from or toward the metal support and that this can be used to modify in a desired way the properties of the metal/oxide interface and in particular its work function.

Bibliography

[1] L. Giordano, F. Cinquini and G. Pacchioni, *Phys. Rev. B* **73**, 045414 (2006).

[2] S. Prada, U. Martinez and G. Pacchioni, *Phys. Rev. B* **78**, 235423 (2008).

[3] H.J. Freund and G. Pacchioni, *Chem. Soc. Rev.* **37**, 2224 (2008).

[4] J.P. Perdew, J.A. Chevary, S.H. Vosko, K.A. Jackson, M.R Pederson, D.J. Singh and C. Fiolhais, *Phys. Rev. B* **46**, 6671 (1992).

[5] R.F.W. Bader, *Chem. Rev.* **91**, 893 (1991).

[6] G. Pacchioni, F. Frigoli, D. Ricci and J.A. Weil, *Phys. Rev. B* **63**, 054102 (2000).

[7] C. Di Valentin, G. Pacchioni and A. Selloni, *Phys. Rev. Lett.* **97**, 166803 (2006).

[8] U. Martinez, L. Giordano and G. Pacchioni, *J. Phys. Chem. B* **110**, 17015 (2006).

[9] D. Stacchiola, S. Kaya, J. Weissenrieder, H. Kuhlenbeck, S. Shaikhutdinov, H.-J. Freund, M. Sierka, T.K. Todorova and J. Sauer, *Angew. Chem., Int. Ed.* **45**, 7636 (2006).

[10] L. Giordano and G. Pacchioni, *Phys. Chem. Chem. Phys.* **8**, 3335 (2006).

[11] M. Chiesa, M.C. Paganini, E. Giamello, D. Murphy, C. Di Valentin and G. Pacchioni, *Acc. Chem. Res.* **39**, 861 (2006).

[12] H.-M. Benia, P. Myrach, A. Gonchar, T. Risse, N. Nilius and H.-J. Freund, *Phys. Rev. B* **81**, 241415 (2010).

[13] K.P. McKenna, A.L. Shluger, *Nat. Mater.* **7**, 859 (2008).

[14] H.M. Benia, P. Myrach, N. Nilius and H.-J. Freund, *Surf. Sci.* **604**, 435 (2010).

[15] D. Scarano, G. Spoto, S. Bordiga, S. Cosuccia and A. Zecchina, *J. Chem. Soc., Faraday Trans.* **88**, 291 (1992).

[16] L. Giordano, G. Pacchioni, J. Goniakowski, N. Nilius, E.D.L. Rienks and H.-J. Freund, *Phys. Rev. Lett.* **101**, 026102 (2008).

[17] N. Mammen, S. Narasimhan and S. de Gironcoli, *J. Am. Chem. Soc.* **133**, 2801 (2011).

Chapter 9

Summary

Wide band-gap simple oxides are rather inert materials, which found applications in heterogeneous catalysis mainly as supports for active metal nanoparticles. This thesis investigates tailored modifications of the oxide characteristics aimed at making these substrates more reactive in catalytic processes. In particular we are interested in engineering the charge transfer with supported metal catalysts in order to enhance their activity and selectivity. By using first principles calculations in the framework of the density functional theory, we have explored two main routes in this field: 1) nanostructuring: oxide films of nanometric thickness deposited on metals differ completely from their bulk counterpart since electron transfer from and towards the metal substrate by tunneling is possible; 2) doping of oxides with substitutional metal ions: a versatile method that increases the opportunities to engineer new materials with enhanced performances.

The third chapter of this thesis is devoted to methodological aspects. Since standard DFT fails to correctly predict some properties of insulating materials, as, for example, the energy band gap, new methods and functionals were implemented to overcome the problem. We have used hybrid functionals and van der Waals corrections to investigate the properties of metal supported oxide films: MgO/Ag and FeO/Pt taken as case studies. We have shown that, while hybrid functionals provide a better description of oxide materials (band gap and structural properties), they sometimes fail in describing metals. The results obtained for the two metal-supported oxide films validate the use of standard DFT and DFT+U methods for the description of adsorption properties and charge transfer phenomena in these combined systems.

In the fourth chapter we have described a strain relaxation mechanism for CaO films deposited on the Mo(001) surface. We have demonstrated that interdiffusion of substrate ions into a thin oxide film is an effective means to release the lattice strain imposed by the support. The mechanism becomes active in compressively strained oxides if the substrate ions occupy less space than the intrinsic cations of the film. Mo ions diffusion into CaO at high temperature originates a mixed Ca_3O_4Mo phase that efficiently releases the strain. Intermixing is not observed, instead, for metal-oxide systems below a critical lattice mismatch, as demonstrated for MgO films on the same substrate.

In chapters 5 and 6 we have considered the role of oxide doping in optimizing the structural and electronic properties of supported metal catalysts. We have shown that doping CaO films with Mo-ions changes the equilibrium shape of Au deposits from 3D to 2D. This is due to a charge transfer that takes place from the *d*-states of Mo lying in the oxide band gap and the empty 6*s* state of gold. Although doping results to be an efficient way to tailor the properties of the adsorbate, the charge transfer turns out to be strongly dependent on the kind of dopant and nature of the oxide. We have demonstrated that over Cr-doped MgO (a system similar to Mo:CaO) Au clusters essentially retain their 3D shape and no charge transfer takes place. The fundamental reason for the different characteristics of the two systems lies in the nature of the dopant rather than in the oxide properties. In fact Cr^{3+}, the most stable state of Cr in the MgO matrix, is not able to transfer electrons to the adsorbed gold, while Mo is able to donate electrons up to the 5+ oxidation state. This is essentially due to the lower ionization potential of Mo with respect to Cr. We have then demonstrated that also the larger lattice parameter of CaO plays a role in favoring the charge transfer. A direct proof of the presence of Mo ions close to the oxide CaO surface is reported in the chapter 7, where we have elucidated the nature of ring structures observed in STM images of a CaO thin film that are connected to temporary charging events of Mo donors embedded in the oxide lattice. The experimental data reported in the chapters 4,5,6 and 7 have been provided by the group of professor H.-J. Freund at the Fritz-Haber Institut of Berlin.

Finally, in the last chapter, we have combined oxide doping and nanostructuring in modifying the work function of metal substrates. By varying parameters like nature, position, and concentration of dopants within the metal-supported oxide films, it is possible in principle to finely tune the work function of the metallic support in a desired way.

Appendix A

Au on Mo:CaO, additional experimental evidences

In chapters 6 and 7 we showed the ability to tune the charge properties of adsorbed gold particle by doping of oxides. In our model it was clear that the charge is transferred from the substitutional dopant, since not other reliable routes were taken into account. However, in the real system other mechanisms can be considered to explain the charge transfer such as, for example, electrons trapped in defects or tunneling from the metal substrate. The photoelectron spectra of the Mo:CaO system provided by the group of Prof. Freund at the Fritz-Haber-Institut of Berlin reported in the following show that Mo ions are oxidized after Au deposition, giving a confirmation of the results reported in this thesis.

X-ray photoelectron spectra of doped CaO films

The spectra were taken on 50 ML thick CaO films, using a laboratory X-ray source and a hemispherical electron analyzer (ESCA 2000). Both the Ca $2p$ and O $1s$ peaks experience a characteristic down-shift in energy by 0.3 eV upon depositing 0.5 ML Au (Fig. A.1). The effect is explained with an upward bending of the oxide bands, induced by an accumulation of extra electrons in the Au islands on the doped film. The nominally negative charge on the Au islands leads to a destabilization of the oxide electronic states at the surface and gives rise to an increase of their energy. No shift occurs for non-doped films, in agreement with the absence of any charge transfer in this case.

A quantitative evaluation of the Mo 3*d* spectra is more challenging, given the low signal-to-noise ratio due to the small dopant concentration (Fig. A.1). After subtracting a Shirley background, the experimental data could be fitted with two doublets according to two different Mo 3*d* peaks. The 3/2 contribution of the dominant doublet is centered at 230 eV and corresponds to Mo in a +2 or +3 charge state. The less intense doublet is up-shifted to 232 eV and can be assigned to Mo^{4+} or Mo^{5+}. To obtain the actual peak positions, the band bending effect has to be taken into account, i.e. 0.3 eV has to be added to the peak energies. Note for comparison that metallic Mo and Mo^{6+} give rise to Mo 3*d* positions at 228 and 236 eV, respectively. The group of Prof. Freund also observed a small but significant increase in the intensity of the high-energy doublet after Au deposition. The area ratio between low- and high-energy doublets was found to change from 3.0 to 3.6, indicating a larger number of highly oxidized Mo ions due to the charge transfer into the gold. The effect is not so pronounced, as a finite number of dopants are in a high oxidation state even before Au deposition, because they have lost electrons to the metal support below the film and to parasitic charge traps in the CaO, e.g. cationic vacancies and line defects.

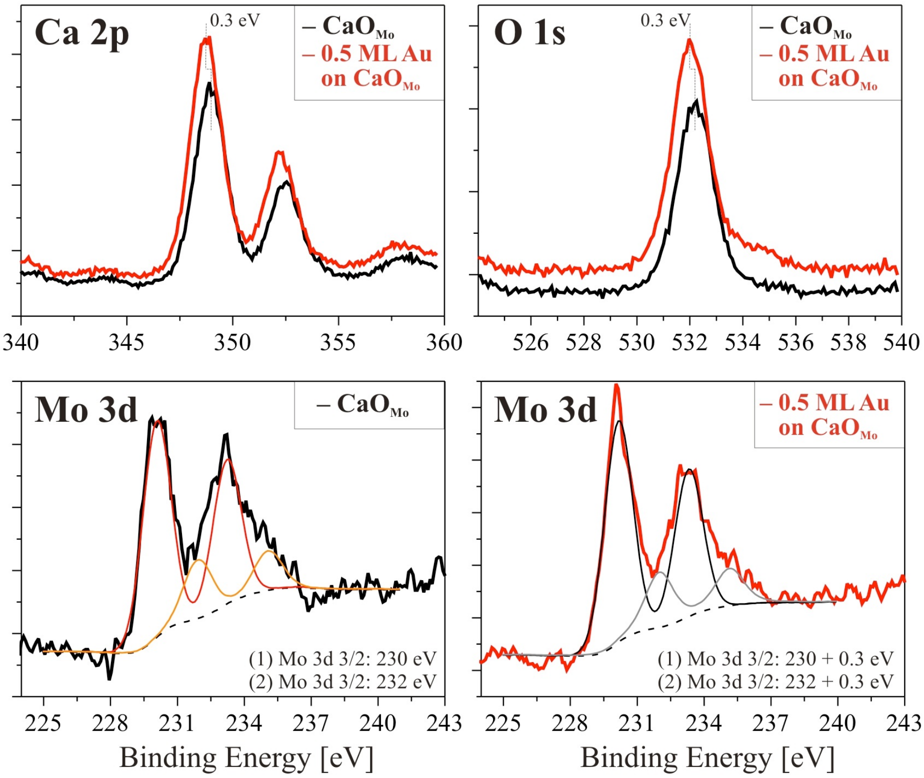

Figure A.1: XP spectra of Ca 2p, O 1s and Mo 3d peaks of the doped CaOMo films before and after Au deposition. Two trends become evident: (1) The oxide electronic states shift by 0.3 eV towards E_{Fermi} due to a band-bending effect induced by the negatively charged gold. (2) A similar trend is absent for the Mo 3d levels that shift to higher energy due to an increase of their oxidation state in presence of the gold.

Appendix B

Nb doped CaO

In chapter 6 we pointed out the parameters that affect the charge transfer mechanism from a dopants to an adsorbed metal catalyst. The most important one is the ionization potential of the dopant, lower is this value more easily an electron can be transferred to an acceptor species (in the considered cases Mo is a better donor than Cr). The second parameter, although less important than the first, is related to the oxide matrix: we showed that the use of the CaO matrix, with a larger lattice parameter, reduces the crystal field splitting and the Madelung potential with respect to the densest MgO matrix. These two effects concur in destabilizing the t_{2g} levels of a transition metal dopants, favouring the charge transfer to the adsorbate.

Starting from the above considerations we can extend the model in order to design new systems with enhanced performances. For example, from simple consideration on the ionization potential trend in the periodic table, we can predict that substituting Mo ions with Nb ions in the CaO matrix should results in a enhancement of the charge transfer properties.

To describe Nb doped CaO properties we used the same model as for the Mo:CaO case (see section 6.2). Standard GGA (PBE) calculations have been done to compute the gold adsorption energies, while PBE0 functional was used for the DOS plot; the choice is motivated by the fact that previous calculations with Mo:CaO have not shown significant differences between standard DFT and hybrid functionals in describing the charge transfer mechanism.

For the description of the proprieties of isolated substitutional Nb a (2×2×2) bulk cell is used and the Brillouin zone is sampled with a (3×3×3)

	adsorption site	E_{ads}(Au), eV	q(Au), e
CaO	O-top	1.35	-0.33
Nb^{2+}:CaO	hollow	3.23	-0.82
Nb^{3+}:CaO	hollow	3.06	-0.79
Nb^{4+}:CaO	hollow	2.60	-0.76
Mo^{2+}:CaO	hollow	3.60	-0.80
Mo^{3+}:CaO	hollow	2.10	-0.79
Mo^{4+}:CaO	hollow	1.72	-0.75

Table B.1: Adsorption properties of Au adatoms adsorbed on pristine and doped CaO surfaces: preferred adsorption site, adsorption energy with respect to gas phase Au (E_{ads}), Au Bader charge (q). Values relative to the Mo:CaO case are also reported for comparison.

Monkhorst-Pack mesh. Nb enters in the oxide as a +2 species substituting one Ca^{2+} ion. The configuration assumed by Nb is $(t_{2g}\alpha)^3$ $(\mathrm{t}_{2g}\beta)^0(e_g)^0$ with the three unpaired d-electrons lying in the oxide gap (Fig. B.1).

For Au adsorption, a (3×3) surface unit cell of a five-layer thick oxide slab is employed, where one impurity atom replaced one oxide cation in the third layer. Au is adsorbed on one side of the slab. The three different adsorption sites described in section 6.3.4 are tested. Impurities with formal oxidation state larger than +2 has been obtained removing one or two electron and adding a neutralizing background to compensate the extra charge. In Table B.1 results relative to the Au binding energy and its Bader charge, along with the preferred adsorption site are reported. It is evident that Nb is able to transfer one of its d-electrons to Au at every oxidation state. This is well visible from the Bader charges and the binding energies that are more than double with respect to pristine CaO surface. The results are confirmed by the DOS shown in Fig. B.1. The comparison with the data reported for Mo:CaO shows that, excluding the TM^{2+} case since the Mo $t_{2g}\beta$ electron lies very high in energy (see chapter 7), the adsorption energy of Au is 1eV higher for Nb with respect to Mo.

We conclude considering the stability of bulk impurities in different oxidation states as explained in section 6.3.1. The calculated Gibbs formation energy with respect to the oxygen partial pressure is shown in Figure B.2 for

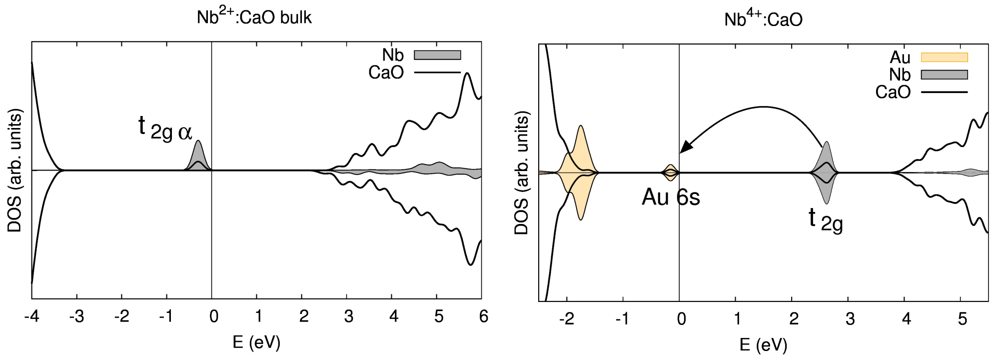

Figure B.1: DOS with PBEO functional, left) bulk Nb^{2+}:CaO, right) Au on Nb^{4+}CaO. The vertical line locates the highest occupied state.

T = 1000K. At the partial pressure of 10^{-10} atm , the most stable states are +3 and +4, states at which the dopant is still able to donate one electron to the adsorbed Au.

In conclusion we predict that Nb is a good charge donor, since it is able to donate all its d-electrons to an electronegative adsorbed species. In this respect it is even a better donor than Mo thanks to its lower ionization potential. The results are confirmed by Density of State calculations and consistent with the thermodynamic ion stability.

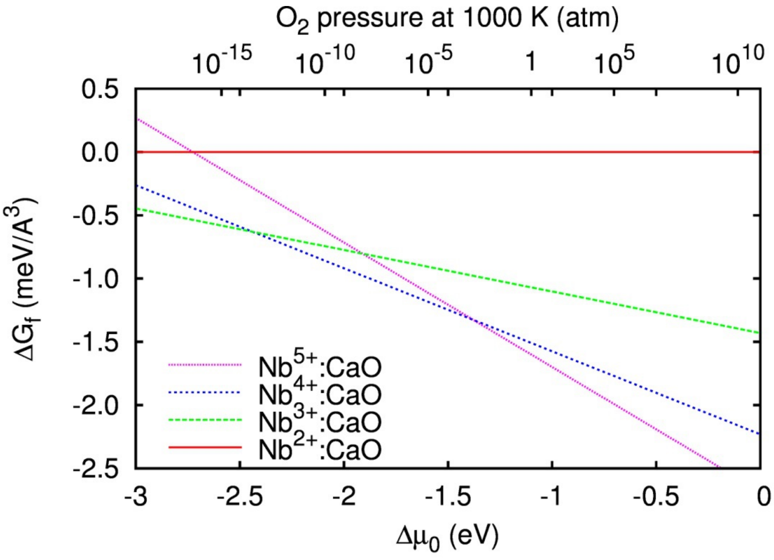

Figure B.2: Change in Gibbs formation energy for the different Nb^{n+} ions. The dependence on the oxygen partial pressure at T = 1000 K is also reported.

Publications

1. X. Shao , P. Myrach, N. Nilius, H.-J. Freund, U. Martinez, S. Prada, L. Giordano and G. Pacchioni., "Strain-induced formation of thin mixed-oxide films", *Phys. Rev. B* **83**, 245407 (2011).
2. X. Shao, S. Prada, L. Giordano, G. Pacchioni, N. Nilius, H.-J. Freund, "Shape control of metal adparticles via doping of the oxide support: An STM and DFT study", *Angewandte Chemie Int. Ed.* **50**, 11525 (2011).
3. S. Prada, L. Giordano and G. Pacchioni "Li, Al, and Ni Substitutional Doping in MgO Ultrathin Films on Metals: Work Function Tuning via Charge Compensation", *J. Phys. Chem. C* **116**, 5781 (2012).
4. F. Stavale, X. Shao, N. Nilius, H.-J. Freund, S. Prada, L. Giordano and G. Pacchioni, "Donor Characteristics of Transition-Metal-Doped Oxides: Cr-Doped MgO versus Mo-Doped CaO", *J. Am. Chem. Soc.* **134**, 11380 (2012).
5. S. Prada, L. Giordano, G. Pacchioni, "Charging of Gold Atoms on Doped MgO and CaO: Identifying the Key Parameters by DFT Calculations", *J. Phys. Chem. C* **117**, 9943 (2013).
6. Y. Cui, N. Nilius, H.-J. Freund, S. Prada, L. Giordano and G. Pacchioni, "Controlling the Charge State of Single Mo-Dopants in a CaO Film", *Phys. Rev. B* **88**, 205421 (2013).
7. S. Prada, L. Giordano, G. Pacchioni and J. Goniakowski, "Theoretical description of oxide metal interfaces: MgO ultra-thin films on Ag(100) as a case study beyond standard DFT", in preparation.

8. S. Prada, L. Giordano, G. Pacchioni and J. Goniakowski, “Properties of Pt-supported iron oxide ultra-thin films: effect of hybrid functionals”, in preparation

Acknowledgements

- My family
- My research group, in particular my supervisor Dr. Livia Giordano and Prof. Gianfranco Pacchioni
- The group “Oxides in Low Dimensions” at the INSP of Paris, in particular Dr. Jacek Goniakowski, for the collaborations and their kind hospitality
- Dr. Niklas Nilius and Prof. Hans-Joachim Freund at the Fritz Haber Institute of Berlin for the fruitful collaborations